A STUDY ON SURFACE ROUGHNESS OF LACTOSE CARRIER PARTICLES

TAN MEI JIN BERNICE

B. Sc. (Pharm.) 1st Class Hons.,

National University of Singapore

A THESIS SUBMITTED

FOR THE DEGREE OF DOCTOR OF PHILOSOPHY

DEPARTMENT OF PHARMACY

NATIONAL UNIVERSITY OF SINGAPORE

2016

DECLARATION

I hereby declare that the thesis is my original work and it has been written by me in its entirety. I have duly acknowledged all the sources of information which have been used in the thesis.

The thesis has also not been submitted for any degree in any university previously.

Tan Mei Jin Bernice

August 2016

ACKNOWLEDGEMENTS

I would like to express my heartfelt gratitude to my supervisors, Associate Professor Paul Heng Wan Sia and Associate Professor Chan Lai Wah, for their guidance, support and encouragement throughout the course of my research work. I am also thankful for the teachings and advice from Dr Celine Liew and Associate Professor TRR Kurup.

I would like to thank the Department of Pharmacy, Faculty of Science and the National University of Singapore for providing me with the research scholarship, research facilities and administrative support in these four years. My special appreciation goes to Ms. Teresa Ang and Ms. Wong Mei Yin for their technical assistance. I would also like to thank Ms. Gloria Tan for her valuable contribution to this work.

I would also like to acknowledge all from the big GEA-NUS family, whom I have had the pleasure of meeting or working alongside. Special mention goes to Dr Asim Kumar Samanta, Dr Loh Zhi Hui and Dr Wong Poh Mun, who guided me through the early stages of my research. To all the research staff, my fellow graduate students, final year project students and exchange students with whom I have worked, the friendships, fun and laughter you have brought to me will not be forgotten.

Finally, I wish to thank my family and friends for their constant support and encouragement throughout these years.

My PhD journey has been made so much more pleasant and enjoyable because of you!

With my sincere appreciation,

Bernice
2016

TABLE OF CONTENTS

SUMMARY

Carrier surface roughness is an important physical characteristic which critically influences the aerosolization of micronized drug particles in carrier-based dry powder inhaler (DPI) formulations. This research work attempted to address several important aspects in the development of improved DPI formulations by surface roughening of lactose carrier particles. In the first part of the work, reliable criteria for roughness measurement were defined, particularly the filtering wavelength in image processing, image size and sample size. Digital filtering of the raw surface profiles obtained by optical profilometry was found to be an important image processing step for obtaining comparative measures of surface roughness. In the second part of the work, roughened carrier particles were prepared using both fluid-bed coating and roller compaction. In fluid-bed coating, the attachment of micronized lactose particles to the surfaces of coarse lactose carriers resulted in changes to the micro-scale surface roughness. The surface roughening effect was investigated using feed powders of different starting particle size and surface area as well as carrier particles in different size fractions. In roller compaction, extensive fragmentation and bonding of particle fragments resulted in much rougher carrier particles of granular nature. The relationships of composition of the powder blend with variability of compaction parameters and carrier surface roughness were studied. The roughened carrier particles produced using both methods, when incorporated into DPI formulations containing a micronized drug, showed significant improvement in the fine particle fractions. Further studies using Raman spectral mapping showed that the surface distribution of drug particles and/or agglomerates was influenced by the degree of carrier surface roughness. Overall, the findings of this research work can aid formulation scientists in refining the selection criteria for carriers in DPI formulations, especially in terms of their surface characteristics.

Page intentionally left blank

LIST OF TABLES

LIST OF FIGURES

LIST OF SYMBOLS AND ABBREVIATIONS

$\sum A$	Total mass of drug deposited in mouthpiece adaptor, induction port, pre-separator and Stages 1 - 8 of the Next Generation Impactor
2D	Two dimensions
3D	Three dimensions
AFM	Atomic force microscope
ANOVA	Analysis of variance
ASME	American Society of Mechanical Engineers
BET	Brunauer–Emmett–Teller
BFE	Basic flowablity energy
DIN	German Institute of Standardization
DPI	Dry powder inhaler
D_s	Surface fractal dimension
d_x	Particle size corresponding to X^{th} volume percentile under the cumulative undersize distribution curve
FB	Fluid-bed coated carrier particles
ff_c	Flow function
F_p	Fraction of drug trapped in pre-separator
FPF	Fine particle fraction
GSD (or σ_g)	Geometric standard deviation
INH	Inhalation grade lactose (InhaLac® 230)
IPA	Isopropyl alcohol
ISO	International Organization for Standardization
$\lambda_{excitation\ source}$	Wavelength of excitation source in the Raman spectrophotometer
MDI	Metered-dose inhaler

M_f	Total mass of drug deposited in Stages 2 - 4 of the Next Generation Impactor
MMAD (or d)	Mass median aerodynamic diameter
MOC	Micro-orifice collector
M_p	Mass of drug deposited in the pre-separator
N	Sample size (for calculation of R_a and R_q)
NGI	Next Generation Impactor
p	Level of significance
$Peak_{1080/1604}$	Ratio of peak intensity at 1080 cm^{-1} to peak intensity at 1604 cm^{-1}
PSD	Power spectral density
R^2	Regression coefficient
R_a	Arithmetic mean roughness
RC	Roller compacted carrier particles
RH	Relative humidity
R_q	Root-mean-square roughness
RSD	Relative standard deviation
RSE	Relative standard error
SEM	Scanning electron microscope
σ_1	Major principal stress
σ_2	Unconfined yield strength
SS	Spectral score
USP	United States Pharmacopoeia
UV	Ultraviolet

Page intentionally left blank

CHAPTER 1

INTRODUCTION

1 INTRODUCTION

Pulmonary drug delivery systems are effective therapeutic options available in the clinical setting for delivering drugs for the treatment of lung diseases as well as for systemic applications. The pulmonary route is optimal for administering drugs to treat asthma and chronic obstructive pulmonary disease (1). The main physiological advantages of the lung as the site for drug delivery include a very large absorptive surface area and the relatively low enzymatic activity present. These physiological conditions in the lung allow substances, which cannot be delivered orally, to be absorbed rapidly into the bloodstream and to avoid first pass metabolism (2). Recent interest in the systemic delivery of medications by the pulmonary route has emerged after studies revealed that the lung epithelium is far more permeable to both small molecules and macromolecules compared to the gastrointestinal tract or skin (3). Coupled with the non-invasive nature of drug delivery, the pulmonary route has emerged as an especially attractive route for delivering therapeutic peptides and proteins and even as an effective alternative route for clinically-approved oral medications.

A pulmonary drug delivery system typically comprises an inhalation device which aids in the generation of an aerosol containing very fine droplets/particles of drug suspended in the gas phase. Inhalation devices may be classified into three types; (a) pressurized metered-dose inhaler (MDI), (b) dry powder inhaler (DPI) and (c) nebulizer. Pressurized MDIs and nebulizers contain drugs present in a liquid formulation while DPIs are formulated as dry powders. Compared to nebulizers, MDIs and DPIs are generally more compact, portable and convenient to use. They are therefore more commonly encountered in the outpatient setting, in particular the MDIs. Nebulizers, on the other hand, are usually reserved for patients unable to use the MDIs or DPIs effectively, such

as very young children or adults with severely compromised lung function (4). This is because nebulizers are generally bulkier due to the requirement of an additional source of compressed air to generate the aerosol in a confined breathing space and are more costly to operate. Regardless of the type of inhalation device, the efficacy of aerosol delivery to the lung is largely determined by four factors: the formulation, metering system, inhalation device design and inhalation technique of the patient (5).

The aerodynamic particle size distribution of the aerosol leaving the inhalation device is arguably the most important pharmaceutical characteristic of inhalers as it is directly related to the extent of drug delivery to the lung (6). Aerosolized drug particles that meet the critical size requirements for deposition at the therapeutically-relevant sites of the respiratory tract are known as respirable particles. An upper particle size limit of 4 – 6 μm is optimal for central airway deposition while that for peripheral airway deposition is 2 – 4 μm (7, 8). Particles below 0.5 μm can enter the deep alveolar lung regions but they may remain airborne and be exhaled with the expiratory airstream (9, 10). Particles larger than 10 μm are unlikely to be conveyed to the lower respiratory tract and are mainly deposited in the oral, pharyngeal and trachea-bronchial regions instead (10-12). The aerodynamic size distribution of aerosols can be assessed *in vitro* using cascade impactors, such as the Andersen cascade impactor and the Next Generation Impactor (NGI), or the multi-stage liquid impinger. An impactor or a liquid impinger is normally used to measure the performance of an inhalation product by means of its fine particle fraction (FPF). The FPF is defined as the mass fraction of respirable particles, which fall in the 1 – 5 μm size range, relative to the nominal dose contained in the device before aerosolization. In general, research efforts into the formulation and inhalation device design are aimed at improving the aerodynamic performance of the aerosol to ensure high FPF and reproducible drug deposition in the lung.

1.1 Dry powder inhalers

DPIs have been available since 1967 when the Spinhaler™, which was the first product for the delivery of sodium cromoglycate, was launched (13). Scientific and commercial interest in the development of DPIs were further stimulated after the implementation of the 1987 Montreal Protocol, which called for nations to phase out the manufacture and use of ozone-depleting chlorofluorocarbons (CFCs) (5). This posed major restrictions to the widespread use of the MDIs as CFCs were the main dispersive energy source of MDIs before alternative propellants were introduced in the later years. In comparison to other inhalation devices, DPIs have the capacity to deliver high doses of drug to the airways (14). The drug dose per actuation is in the order of tens or hundreds of micrograms (15). Stability of the drug substance in dry form and the reduced need for coordination of device actuation and inhalation are some other advantages of DPIs (5).

In order to overcome the natural barriers of the respiratory system to large foreign particles in the environment, drugs in a DPI have to be delivered as very fine particles (typically in micronized form) in the inhaled airstream. As a result of its small particle size and high surface energy, these fine drug particles tend to be highly agglomerative and poorly dispersible (16). Cohesion between fine particles is predominantly due to the van der Waals, capillary and electrostatic forces (17). These forces have to be overcome for the efficient dispersion of fine drug powders into discrete primary particles when inhaled. Researchers developing DPI formulations generally adopt a two-pronged approach to overcome the technical challenges associated with fine agglomerative particles. These two approaches are best examined by broadly dividing DPI formulations into two categories: (a) carrier-free formulations which usually, but not always, contain only drug particles of a suitable morphological form for effective lung delivery and (b)

carrier-based formulations which contain coarse carrier particles (typically lactose), in the size range of 40 – 200 μm, blended with the micronized drug.

1.1.1 Carrier-free formulations

Carrier-free formulations have been developed using a wide variety of sophisticated particle engineering techniques, which are aimed at reducing the intrinsic cohesion between very fine particles (18). There is no defined approach to the formulation of carrier-free particles because the methods adopted are highly dependent on the chemical and physical nature of the active ingredient. Hence, almost all successful commercial products utilizing these technologies generally fall under specific patent protection. An important distinction must be made between carrier-free formulations and excipient-free formulations. Conventionally, carriers in DPIs should fulfill two main criteria: (a) they are of a much larger physical size compared to the drug particles and (b) drug particles are distributed on the surfaces of carrier particles after blending. Therefore, the function of a carrier is dependent on its formation of an interactive mixture with the fine drug particles (Figure 1). Formulations may contain excipients which do not strictly fulfill the 'carrier' criteria but may occasionally be classified as carrier-free formulations in literature.

A number of carrier-free formulations have been produced by coating lipid materials (19), L-leucine (20, 21) and magnesium stearate (22) on drug particles to reduce their cohesiveness. Mannitol (23), trileucine (24) and other excipients (25) have also been used to reduce the cohesiveness of spray-dried particulates which contain drug. Some carrier-free formulations contain drug particles with large geometric mean diameters (5 – 20 μm) but low density (less than 0.4 g/cm^3) as a result of their porous structures (26). The aerodynamic performance of these large and porous particles has been shown to be

equivalent to that of smaller micronized particles but they exhibit improved flow and reduced bulk cohesiveness. Spray-dried drug particles in the 1 – 5 μm size range and with wrinkled surfaces or spherical shapes have also been successfully developed as inhalation products. They have been shown to exhibit lower dispersion energies during aerosolization (18). In order to complement the carrier-free formulations, inhaler devices may be specially designed to improve drug dispersion in these formulations. Some examples include the Intal Spincaps™ (27), Bricanyl® Turbohaler and Pulmicort® Turbohaler (28, 29), which create turbulent airflow for more efficient drug deaggregation.

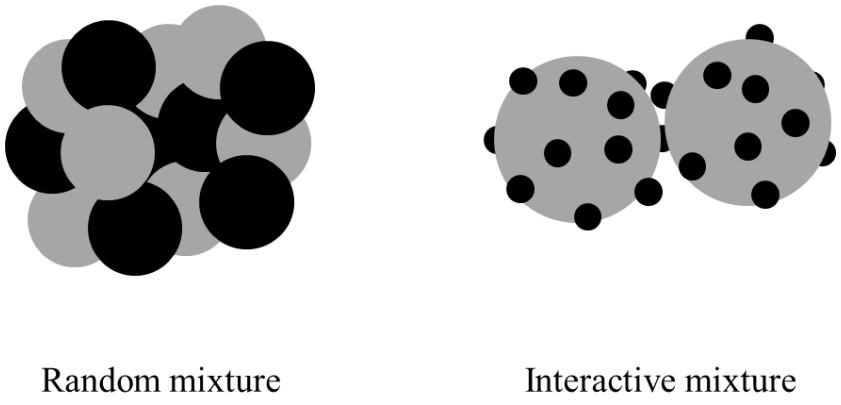

Figure 1. The differences in the orientation of particles, relative to each other, in random and interactive mixtures. The different-coloured spheres represent two different materials, or particles of the same material but with different sizes.

1.1.2 Carrier-based formulations

Carrier-based DPI formulations contain coarse carrier particles which are physically blended with micronized drug particles. Lactose monohydrate is the most commonly used carrier in commercially-available carrier-based DPIs and the typical carrier to drug mass ratio is 67.5:1 (10, 30-32). Alternative carrier materials that have been reported in

literature include mannitol, trehalose, erythritol and sorbitol (33, 34). In carrier-based formulations, drug particles adhere to the surfaces of carrier particles via different forms of particle interaction, resulting in a certain degree of ordered/interactive mixing (35, 36). This reduces the amount of free drug agglomerates, improves bulk flow and thereby enables more precise dose metering (37). The 'carrier' function of these excipients is best understood by examining the mechanisms of drug dispersion during inhalation. Compared to the agglomerates of fine drug particles, carrier particles are more susceptible to the aerodynamic forces in the turbulent airflow generated upon an inspiratory effort (38). After the carrier particles are entrained in the air, a combination of three groups of forces aid in the dislodgement of drug particles from the carrier surfaces. These forces may be broadly categorized as the (a) drag and lift, (b) shear and friction and (c) inertial forces, as shown in Figure 2. The detachment processes must occur within a relatively short time span, after the release of the powder from the inhaler into the oral cavity and the respiratory system. Due to their large particle size, carrier particles are mainly deposited in the oro-pharyngeal region where they are eventually swallowed. Hence, carrier particles do not increase the burden of lung clearance of foreign matter even though the percentages by mass of carriers are typically greater than 95 % of the DPI formulation.

Lactose monohydrate remains as the excipient of choice for carrier-based DPI formulations. There is an abundance of published literature about the preparation, characterization and performance of lactose carriers in DPIs. Several comprehensive review articles have been dedicated to the discussion of the physicochemical characteristics of lactose carriers, mechanistic aspects of drug dispersion in DPI formulations containing lactose and its interaction with inhaler design (5, 39-43). The size, size distribution, surface roughness, moisture content and crystal habit of lactose

carriers have been found to interact in complex relationships and influence one or more of the many performance attributes of DPIs (5). In addition to carrier properties, DPI performance may also be influenced by the type of drug, the physicochemical properties of the drug and the inhaler design.

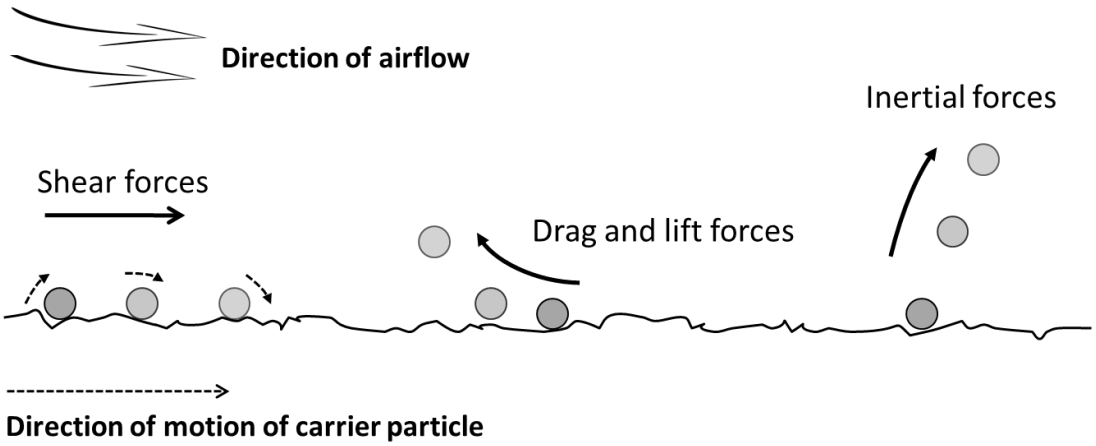

Figure 2. The mechanisms of drug detachment from the carrier surface.

Surface roughness (or rugosity) is an apparently simple inherent property of carrier particles. However, it is also a primary influence of the physical interactions between the drug and carrier in contact. Hence, it can affect the formulation and performance of a DPI in several ways. Surface roughness has an impact on mixing (44, 45) and the stability of interactive mixtures (46, 47). Interactive mixing of a DPI formulation is a two-step process involving the breaking up of drug particle agglomerates and dispersion of these fine particles on the surfaces of carrier particles. The surface asperities on rougher particles may restrict the opportunities for close contact between two approaching surfaces and hinder the adhesion of drug onto carrier surfaces during

blending. Drug agglomerates trapped in the recesses between the large asperities are also sheltered from the blending forces, which are essential for the continual breakage of drug agglomerates and the redistribution of drug particles to other carrier surfaces. This may adversely affect blend homogeneity during mixing. Rougher carrier surfaces, on the other hand, can promote blend stability by reducing the ease of removal of the drug particles by low shear abrasive forces. This decreases the likelihood of drug particles rolling off the surfaces during capsule or blister filling. However, the performance of DPI formulations containing rougher carrier particles was poorer as the drug particles were more firmly attached to the carrier surfaces and remained largely immobile (48-50). Surface roughness can dictate the adhesion potential of drug particles onto carriers, an attribute which also determines the ability of drug particles to detach from the carrier surfaces in the airstream when subjected to higher shear forces. A strong negative correlation between the carrier roughness and the FPF of a binary mixture composed of terbutaline and lactose has been observed (51). Lactose carriers that exhibit larger variability in adhesion force measurements also tended to result in greater standard deviations of FPF when *in vitro* studies were conducted (52). Hence, the reduction of carrier roughness can be a foremost strategy to reduce drug-carrier adhesion, although some researchers have suggested otherwise (41, 45, 53). It has been noted that an increase in carrier roughness does not necessarily affect the FPF adversely when the predominant mechanism for drug dispersion is by inertial impaction (45, 54). Despite considerable studies conducted in this area, it still remains a major challenge to relate the surface roughness to the functional characteristics of the carrier (55). This is partly due to the difficulties in developing methodologies with clearly defined parameters for surface characterization and in the definition of surface roughness. The following

sections in this chapter are dedicated to an in-depth review of surface roughness of particulate matter, with an emphasis on their impact on DPI performance.

1.2 Surface roughness of particulates

1.2.1 Fundamental concepts in surface roughness analysis

A surface can be visualised as a horizontal plane with surface irregularities (i.e., peaks and valleys) projecting from the plane. It can be represented in two dimensions (2D) by a cross-sectional line profile or in three dimensions (3D) by the surface topography. Depending on the scale of observation (or otherwise the degree of magnification at which a surface is viewed), the ‘smoothness’ or ‘roughness’ of the surface can vary significantly. A flat and shiny surface visually appears as smooth. However, as surface details are magnified under a microscope and observed over a shorter length scales, the surface may appear much rougher due to the presence of many surface irregularities. Hence, roughness is a scale-dependent property of a surface and any qualitative or quantitative measurement of roughness should be accompanied by the magnification and resolution of the surface profile.

As an alternative to the image magnification, the scale of observation of a surface can be more precisely defined by mathematical means. This involves an analysis of the spectrum of spatial frequency components present on the surface. In mathematics, a curve of any shape can be broken down (i.e., decomposed) into its constituent sine functions using Fourier analysis. Each sine function is defined by its amplitude and frequency of oscillation and the summation of all the sine functions results in the original curve. Fourier analysis can similarly be applied to surface profiles, regardless of whether they are in 2D or 3D. The term ‘spatial frequency’ is used to describe the number of times the surface features repeat per unit lateral distance while the amplitude refers to the

deviation of surface heights in the vertical direction. It is generally accepted that the low- and medium-frequency (i.e., widely-spaced) components constitute the shape and waviness of the surface, while high-frequency (i.e., closely-spaced) components constitute the surface roughness (Figure 3). A measured surface profile can be filtered into a series of sub-images, each containing only the surface features within well-defined spatial frequency (also known as cut-off frequency) ranges (56, 57). This facilitates the numerical characterization of the surface, based on their roughness attributes, waviness and shape profiles. A variety of filtering techniques for separating roughness from waviness and shape are proposed in the International Organization for Standardization (ISO), American Society of Mechanical Engineers (ASME) and German Institute of Standardization (DIN) standards (57). Selection of cut-off frequencies for the roughness profile is dependent on the lateral resolution of the stylus or optical instrument used in surface mapping. Hence, surface roughness measurements are only meaningful when accompanied by appropriate measurement and image processing criteria (58, 59).

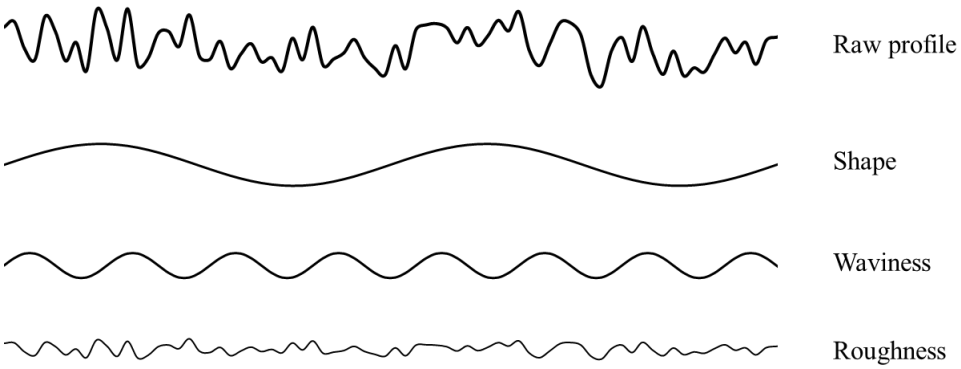

Figure 3. Surface information at different length scales can be extracted from the raw surface profile.

The study of surface metrology has historically been essential in many engineering disciplines especially where the surface finish of machine parts determines their performance. For such engineered surfaces, it has been widely accepted that surface features of different spatial frequencies affect their functions in different ways (57). For carrier particles in a DPI formulation, the spatial frequencies of surface features that most critically affect drug adhesion and detachment have not been clearly defined yet in literature. However, carrier surface models in pictorial form have been proposed to describe the roughness of carriers at the different length scales and its effect on drug dispersion, most often in relation to the particle size of the drug (9, 60, 61). Figure 4 illustrates how drug particles may interact with the carrier surface features presented at different length scales. Generally, crevices and protuberances on carrier surfaces that are wider than the diameters of the micronized drug particles and in which the particles can be entrapped within constitute the macro-roughness of the surface (62). It has been suggested in literature that the entrapment of drug particles usually adversely affects drug-carrier separation as a greater inspiratory effort would be required to dislodge the entrapped drug particles. On the other hand, nano-roughness refers to the nano-scale surface asperities which are much smaller in size than the drug particles. Nano-scale surface asperities establish a controlled number of contact points between adhering drug particles and carrier surfaces, and determine both the true area of contact and their distance of separation (63). The increase in nano-scale roughness is usually associated with a positive effect on drug dispersion.

Often, surface roughness is quantitatively represented by surface height parameters that are based only on the magnitude of asperity heights but provide no additional information on the length scale of the asperities. The roughness of particulate matter in different literature reports ranges from a few tens to hundreds or even a thousand nm.

The wide reported range could be attributed to the marked variability in length scale from which the surface information was obtained. Roughness values are almost always significantly smaller in magnitude than drug particles (1 – 5 μm). There is no consensus on the extent of roughening or smoothening of carrier particles required to result in significant changes to DPI performance. No optimal roughness value for carriers has been defined because the differences in other particle properties such as size, size distribution, shape, crystallinity, flow and packing properties may also alter carrier performance (9, 31, 48). Nevertheless, these surface models still provide useful modes for the classification of carrier surfaces to account for the differences in DPI performance with respect to carrier surface roughness.

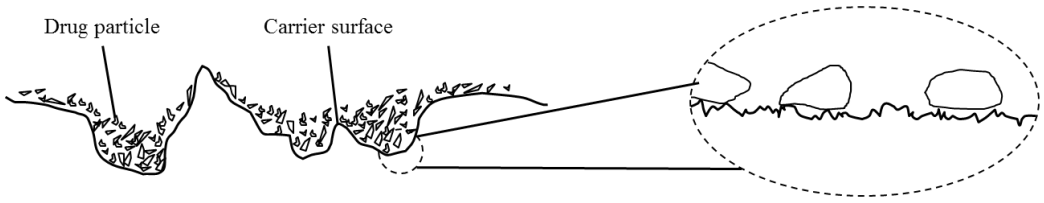

Macro-roughness
- Observed at longer length scales
- Lower spatial frequency

Nano-roughness
- Observed at shorter length scales
- Higher spatial frequency

Figure 4. The interaction of micronized drug particles with carrier surface features at different length scales.

1.2.2 Factors affecting the measurement of surface roughness

1.2.2.1 Particle size

A major challenge in determining the surface roughness of carrier particles is their relatively small particle sizes, which typically fall between 40 – 200 μm. Due to the random orientation of particles on the measurement stage and variability in their shapes, it is laborious to locate sufficiently large number of suitable planar surfaces for roughness measurements and to obtain statistically acceptable mean values. Tilted or curved surfaces that are very rough often contain surface features that exceed the range of vertical distance from the measurement stage (in the order of a few μm) which very precise stylus-based instruments can measure. The size of sampling areas is thus markedly limited and this hampers accurate quantification of surface heights at larger length scales. Conventionally, determination of the roughness of irregular particles smaller than 20 μm was considered neither useful nor reliable (64), as they existed largely as fragments with a large number of fracture planes and abrupt variations in particle shape. Another challenge encountered during surface profiling of small particles is the inadequate resolution of surface details. Hence, very few studies have investigated the surface roughness of micronized particles in DPI research, with the exception of two studies on spherical bovine serum albumin particles (54, 65). The use of precise instruments, such as the atomic force microscope (AFM) and the confocal laser scanning microscope, is necessary for resolving the nano-scale surface features on micronized particles (17, 54, 66). The geometry of the stylus tip, and any wear sustained during the measurement process, has a significant influence on the accuracy of the measured roughness value (67).

1.2.2.2 Measurement conditions

Three major considerations in image capture and analysis to validate roughness parameters are the scan area (68, 69), image processing technique (68) and probe tip geometry for stylus-based instruments (67, 70). As the tilt on a surface should not exceed 7° for high precision roughness measurements (53), scans are generally limited to very small areas. Thus, a very large number of images are required to accurately represent the surfaces of particles in a sample (71). In 2D line profiling, a characteristic length, given by the minimum length that allows for representative roughness measurements, exists for any given surface (68). A minimum sampling length should be at least four to five times the characteristic length for representative measurements to be obtained. As it increases further, confidence in a scale-independent roughness measurement also increases. For a given surface, the magnitude of roughness increases with the sampling length or area due to the inclusion of more prominent surface features (72). In one study, the mean root mean square roughness of a lactose tablet surface using 1 μm^2 scan areas was 7.7 nm compared to 53.7 nm when the scan area was 2500 μm^2 (69). In another study, smaller scan areas increased the standard deviation of the arithmetic mean roughness and root mean square roughness by almost 50 % of their respective mean values (53). Prior optimisation of the sampling length and measurement variables, such as the depth and rate of image scans, was shown to be important for accurate roughness measurement using the scanning probe microscope (60). For the highest resolution of surface details using stylus-based instruments, probe–surface interaction should take place when the surface is perpendicular to the axis of the probe tip (73). This condition is not always met when the geometry of the probe tip is not as sharp as the peaks and valleys on highly irregular surfaces (68). Any surface asperity that is sharper than the probe tip cannot be accurately reproduced on the surface topography and a mirrored shape of the tip is

produced instead (69). Lateral forces experienced by the probe tip contribute to the distortion of surface features (74). Issues of probe tip wear and tear or breakage are commonly encountered if the probe comes into contact with the surface during scanning (75). In order for accurate representation of the surface, the sample needs to be relatively smooth on a scale comparable to the radius of the curvature at the apex of the tip (67).

1.2.2.3 Image processing techniques

The application of algorithms to remove sample tilt and surface curvature is required for surface images since the particle surfaces are rarely perfectly flat planes. Subsequently, filtering of the surface profile is required before surface texture parameters can be derived (76). Filtering involves the suppression of surface components of selected spatial frequencies so that the surface profile at the desired length scale is obtained. The use of standard roughness parameters alone does not always allow meaningful comparison of data obtained from different measuring instruments unless surface profiles of identical spatial frequencies are extracted (57). Until a functional correlation between particular surface components and carrier performance can be established, neither the shape, waviness nor roughness of particles should be omitted when undertaking surface analysis (56). The lack of a proper definition of surface roughness of carrier particles may have contributed to the reported conflicting trends in surface roughness and DPI performance. While the standardisation of filtering techniques is necessary, there are also concerns that post-processed images may be a misrepresentation of the actual average surfaces (68). Hence, a variety of filtering techniques are still being developed for surfaces with different characteristics and for increasingly complex applications in surface roughness analysis (57).

1.2.2.4 Selection of roughness parameters

Surface topography contains a series of data points with each being defined by its x-, y- and z-coordinates relative to a mean surface. Line profiles are defined by points along the x- (or y-) and z-axis. Before the advent of 3D surface profiling instruments, such as white light interferometers, surface analysis was largely based on 2D line profilometry. Many repeatedly-spaced line scans were required to produce 3D surface topographies. Two-dimensional surface parameters are denoted by different prefixes that reflect the surface components described (76-80). For example, P_a, W_a and R_a represent the arithmetic mean surface height in the shape, waviness and roughness profiles, respectively. At present, it is recognised that the spatial distribution of surface features from 3D measurements may allow more comprehensive surface analysis. In addition to height parameters, many spatial and hybrid parameters relevant only to 3D surfaces have been derived (81). All 3D parameters start with the prefix S and are distinguished by the filtering process for the derivation of the parameter (78). However, due to their simple physical interpretation and long history of use, R_a and R_q remain as the most widely-used roughness parameters in pharmaceutical research (56, 80). Fractal descriptors, which are derived from 2D pixel measurements of particles in images from light microscopes, have also been used when surface profilometers are not available. However, they can be unreliable for accurate characterisation of surface roughness due to the insufficient image resolution (64). The use of single height parameters to represent surface roughness imparts simplicity for making statistical comparisons but they do not contain any actual spatial information about the surface (68, 82). The ratios of the distances between carrier surface features to drug particle size may account for the likelihood of drug entrapment (61). Without specifying the length scale of roughness, numerically large height parameters could be describing surfaces of vastly different qualities. For higher

roughness measurement values at the greater length scales, surfaces may contain wide and deep surface crevices. On the other hand, tall but closely-spaced asperities may also result in comparable roughness values. Hence, a combination of height and spatial parameters is usually necessary to provide reflective information about the specific qualities of a surface (53, 77).

1.2.3 Methods to measure surface roughness

1.2.3.1 Surface profiling by atomic force microscopy

The AFM is capable of recording the surface topography down to sub-nanometre resolution besides determining the adhesion force between the probe tip and the surface (58, 68, 83). This allows the direct estimation of the strength of drug particle adhesion to the shape of individual asperities (69). Surface roughness on length scales with many orders of magnitude can be measured by the AFM. A sharp probe mounted on a cantilever spring traverses the surface during a scan. The force required to lift the probe off the surface can also be measured (69, 83, 84). Deflection of the probe corresponding to the height of each scan point is monitored by a laser beam reflected onto a position-sensitive photodiode detector. The AFM is often used as a reference method for roughness measurement as it involves physical mapping by a probe of the surface and produces images with superior resolution (85). The ability of the AFM to resolve nano-scale surface features is achieved by positioning the probe tip at very close distances from the surface asperities while the scans are conducted over very small areas of the surface (85). The duration required to scan a $5 \times 5\ \mu m^2$ area of a surface was reported to be 15 min when using the AFM, but only 30 s for a $45 \times 59\ \mu m^2$ area using an optical method (86). The AFM also exhibits a limited vertical range of the probe deflection and tall asperities or deep crevices often cannot be measured at all (39, 51). In one study, the surface roughness of relatively smooth anhydrous lactose particles with R_q of 300 – 600

nm was successfully characterised using the AFM (87). In contrast, accurate measurements of similarly-sized fractions of rough, fluid-bed granulated lactose particles could not be obtained. In another study, the roughness of several inhalable grades of lactose particles also could not be accurately measured due to the restricted movement of the probe, particularly at very rough sections of the surfaces (88). Hence, the AFM appears to be ideal for smooth to moderately rough surfaces and is not suited for very rough surfaces especially when the scan area is large.

1.2.3.2 Non-contact surface profiling by optical methods

Optical profilers make use of white light interferometry to measure very rough surfaces (R_a in the order of μm), especially those which the AFM cannot measure due to the restricted probe vertical deflection range (88, 89). However, most optical profilers also exhibit a limited lateral resolution of about 0.5 μm (80) and are more effective at evaluating the macro-roughness of a surface. An interferometer is present together with the objective lens in the optical profiler (80). Light from an optical source is split into two coherent beams; the reference beam follows a fixed optical path in the interferometer, while the sample beam is directed to and reflected from the sample (89). When the objective lens is positioned at the plane of precise focus, maximal constructive interference, resulting from the combination of the two beams, is detected by the charge-coupled device camera. The plane of focus of every point on the surface is detected through vertical scanning of the objective lens. The suitability of using the optical profiler for determining the roughness of both micron-sized protein particles and coarse lactose carrier particles has been evaluated (86). Particles were imaged using three different instruments: scanning electron microscope (SEM), optical profiler and AFM. Visual observations of all surface profiles suggested that there was good agreement among the three methods. The root mean square roughness values determined by the

optical profiler were slightly higher but correlated well with measurements using the AFM. However, it has been reported elsewhere that the optical profiler is unable to image regions of spherical surfaces if the surface slope exceeds 30º (80). Sub-micron surface details are likely to be smoothened out due to the limited image resolution (85). Optical artefacts can also contribute to significant deviations in roughness values determined when surface features have extreme gradients. The extreme sensitivity of the optical profiler to vibration may also lead to high variability in roughness measurements (86). This, however, can be overcome by placing optical profilers on vibration-dampening tables.

Confocal laser scanning microscopy is another optical technique used to produce high resolution 3D images of surfaces (89). A spatial pinhole between the photo-detector and sample is employed to eliminate out-of-focus light, so that only light from the focal plane forms the image. Images are constructed from point-to-point scans across the surface. This technique was used to quantify the surface roughness of spherical spray-dried mannitol particles with mean particle size of 13 – 14 μm (66). The lateral resolution was reported to be 120 nm with a minimum detectable roughness of 10 nm. Fourier transformation of the data was required to differentiate the small-scale from the large-scale roughness, which also included a component of particle shape. As the roughness values obtained corresponded well to visual observations of the particles under the SEM, this method was proposed as a simple quantitative technique for roughness measurement of spherical particles.

Light scattering techniques have been used to obtain the surface fractal dimension of particles as a parameter of surface roughness (65). Particles in suspension are subject to an incident light beam that is scattered in various reflected angles due to the presence of surface irregularities. The intensity of scattered light and scatter angles are measured by

detectors positioned at various angles. The surface fractal dimension is obtained from the fractal region of the scattering curve where surface structures can be resolved. In one study, a Mastersizer S laser diffractometer (Malvern, Worcs, UK) was used to quantify the roughness of 2 μm spray-dried bovine serum albumin particles (65). Due to their small particle size, the roughness values obtained were not considered as physically correct but were more useful to rank order the samples. The roughness trend obtained was consistent with visual observations of the samples under the SEM.

1.2.3.3 Surface imaging by scanning electron microscopy

The SEM has been widely used for qualitative roughness analysis due to the possibility for high magnification and resolution (80). It is routinely used for investigating particle morphology, ordered structures in powder mixtures (89) and for obtaining fractal descriptors in quantitative roughness analysis (90). However, only roughness at the macro-scale can be reliably evaluated due to limitations in the image resolution in comparison with the AFM (90). In a study, lactose particle surfaces were visibly smooth in SEM images but were significantly rougher, with peaks and valleys varying over 0.5 μm, when measured using the AFM (88). Even though SEM images appear to have a 3D structure, the extraction of 3D information is of limited use for accurate roughness quantification due to the sophistication and errors in the mathematical methods employed (91). However, 3D reconstruction software has been used on one occasion to create surface line profiles of 80 μm mannitol particles from SEM images (61). The R_a values were obtained by averaging several R_a values from different line profiles over the analysed surfaces. Similar to the AFM, it is generally time-consuming to obtain a representative number of images for accurate roughness quantification (62). In addition to qualitative surface analysis, the SEM has been used to investigate agglomerate structure and the organisation of drug and carrier particles in DPI mixtures. In one study,

images of micronized budesonide powder showed that a high proportion of particles with optical diameters of 1 – 5 μm presented as agglomerates (92). Even after prolonged mixing with carrier lactose in a Turbula® mixer, drug agglomerates still remained but became more predominantly concentrated within the surface crevices of carrier particles. This suggests that rougher areas of the surfaces were strong binding sites for the drug particles and confirmed the highly cohesive nature of budesonide, which was in agreement with findings from the drug–carrier adhesion experiments (17).

1.2.3.4 Determination of specific surface area

The specific surface area of particles has been used as an indirect measure of surface roughness. The particle size, shape and porosity are additional factors which also influence the surface area (53). Several studies have reported positive correlations between the surface roughness and specific surface area of particles. Surface area can be measured using nitrogen adsorption with the single-point (87) or multiple-point Brunauer–Emmett–Teller (BET) methods (90) or by air permeametry (9). Nitrogen adsorption method is preferable to air permeametry as it is more accurate, especially when large particles are involved (90). Among the different nitrogen adsorption techniques, the static volumetric technique was found to be more sensitive to changes in carrier roughness and showed better correlation with SEM images and AFM measurements. The specific surface area of different commercial grades of recrystallised, fluid-bed granulated and spray-dried lactose particles was positively correlated with the emitted dose and the FPF in an *in vitro* study involving the drug, pranlukast hydrate (93). This was attributed to the greater drug-carrying capacity of rougher lactose particles. However, surface area measurements alone cannot distinguish between roughness at different length scales and surface imaging is still necessary for meaningful roughness characterisation.

1.2.4 Surface roughness modification

1.2.4.1 Spray drying

Spray drying has been most commonly investigated for the surface modification of fine drug particles since highly spherical particles with homogenous surfaces can be produced. Homogenous surfaces offer similar adhesion conditions to adhering particles, whereas milling causes particles to have variable surface affinities as mechanical damage creates sharp edges and amorphous regions on crystalline surfaces (89). Both smooth and corrugated bovine serum albumin particles with R_q of 15 and 67 nm, respectively, have been prepared by using different parameters in spray drying (54, 65). A lower feed concentration, air atomisation pressure, inlet and outlet temperatures resulted in rougher particles without significant changes to their median diameter. Rough surfaces were formed due to indentations on the surface when the external crust of protein collapsed into the protein-depleted interior as drying progressed. In another study, the roughness of spray-dried bovine serum albumin particles was quantified using the surface fractal dimension, D_s (65). A D_s value of 2 indicates a perfectly smooth surface while a value of 3 represents a very rough surface. It was found that a small increase in surface roughness, from 2.06 to 2.18, was sufficient to improve the FPF significantly when the formulation was tested in a Rotahaler®. It was thought that rougher particles adhered less to the walls of the inhaler and were easier to disperse. No improvement in FPF was observed when D_s was further increased from 2.18 to 2.41. The rougher surfaces could also have contributed to higher drag forces on the particles when they were airborne and this accounted for the constant FPF despite further increase in surface roughness. The influence of the outlet air temperature on surface roughness was found to vary according to the size of the spray dryer used. Mannitol carrier particles were prepared by spray drying 15 %, w/w aqueous mannitol solutions. The R_a of approximately 13 μm mannitol

particles was about 120 nm when the outlet air temperature was 60 ºC and 240 nm when the temperature was increased to 120 ºC in a laboratory-scale spray dryer (66). With a lower outlet air temperature, the slower rate of drying led to supersaturated layers of mannitol solution on the particle surfaces. Upon drying, tiny surface crystals were formed and this led to smoother surfaces. When a similar study was conducted using a pilot-scale spray dryer (diameter, 2.7 m; height, 3.7 m), which was significantly larger than the laboratory-scale spray dryer, the influence of the outlet air temperature on roughness was found to be reversed (61). Mannitol carrier particles with diameters of about 80 μm were prepared. Particles with the roughest surfaces (R_a = 140 nm) were produced with an outlet air temperature of 67 ºC and the rough surfaces were due to approximately 3 μm rod-shaped crystals lining the surface. When the temperature was increased to 84 ºC, smoother particles (R_a = 89 nm) were formed due to the presence of singular and smaller surface crystals. The exact reason for the differences in the two studies is unclear but it appeared to be related to the scale of the spray dryer and the post-spray particle residence time in flight. The highest FPF was obtained when rougher particles produced by the laboratory-scale spray dryer were used (66), while the lowest FPF was obtained when rougher particles produced by the pilot-scale spray dryer were used (61). The differing trends were attributed to the differences in the quality of surface roughness of the particles produced by the two spray dryers. The laboratory-scale model produced particles with long-wave roughness, which promoted the entrapment of drug particles and thus decreased the FPF. On the other hand, the pilot-scale model produced particles with short-wave roughness which increased the FPF (61).

The spray drying process has also been used for surface smoothening by polymer coating of lactose particles (94). Both ethylcellulose and polyvinylpyrrolidone were investigated as coating materials for lactose carriers in the size range of 63 – 90 μm. The feed for

spray drying consisted of coarse lactose carriers suspended in a saturated lactose-ethanol solution containing the dissolved polymer. Coated lactose appeared visibly smoother than the uncoated lactose under the SEM even though there were no significant differences in the roughness parameters determined by the AFM. The chemical nature of the coated particle surface resembled that of the polymer, indicating successful surface coverage. The FPF of DPI formulations containing polyvinylpyrrolidone-coated and ethylcellulose-coated lactose carriers were lower and higher than that of the uncoated lactose carrier, respectively. It was found that the increase in the drug-carrier adhesion was accompanied by a reduction in the FPF. However, the lactose particles were coated with polymers with different chemical nature and the differences in adhesion forces could no longer be solely ascribed to changes in the carrier surface roughness.

1.2.4.2 Solution phase processing

Solution phase processing describes techniques where carrier particles are exposed to a liquid medium to bring about partial surface dissolution of adhering fines and asperities without any marked change to the mean particle size and overall shape (95). Dry lactose carrier particles have been added to a saturated solution of lactose at 25 ºC for the initiation of temperature-controlled dissolution. By ramping up the temperature at a controlled rate of 0.5 ºC/min to the final set temperature ranging from 30 ºC to 50 ºC, particles with different surface roughness were produced. A higher dissolution temperature resulted in smoother particle surfaces with less adhering fines when visualised under the SEM (95). This method did not result in significant changes to the flowability, surface area and crystallinity of lactose. Surface smoothening appeared to reduce the number of active sites since the FPF was improved, especially for drug to carrier ratios of less than 1:100 (96). Decantation methods have also been explored for surface smoothening of carrier particles. In one study, lactose and mannitol particles

were repeatedly immersed in absolute ethanol and decanted (with fresh solvent replaced) to result in partial dissolution of the adhering fines and surface smoothening (62, 88). In another study, decantation was combined with wet sieving. The process was repeated a total of eight times to obtain homogenous smooth-surfaced crystalline lactose for roughness analysis (86). In all dissolution-related methods, surface smoothening is achieved by reducing both the surface fines and surface asperities. An increase in the drug adhesion forces occurs, accompanied by the reduction of FPF when smoothened particles of this type are used in comparison to the untreated particles (62, 97).

Surface smoothening of milled lactose particles by the adsorption of moisture and subsequent dissolution of adhering micron-sized fines has been validated by surface area measurement and SEM imaging (98). Changes to the lactose particle surfaces were controlled by three main variables: relative humidity during storage, concentration of adhering fines and duration of storage. When lactose was stored at room temperature and a low relative humidity of 32 % for 10 days, the specific surface area decreased by 40 % without any observable change in surface roughness. This phenomenon was attributed to the preferential dissolution of sub-micron surface features according to the Kelvin effect (98, 99). Micron-sized (or larger) features remained relatively unaffected by adsorbed moisture at low humidity levels. In contrast, smoother surfaces were clearly observable in SEM images when the relative humidity was increased to 75 %. In another study, the exposure of atomically smooth α-lactose monohydrate crystals (R_q = 0.250 nm) to either increasing relative humidity conditions (15 – 75 % RH) or 75 % RH for 12 h had no effect on either the appearance or the root mean square roughness of the crystalline particles (100). The attractive forces between two dry particles are mainly van der Waals and electrostatic forces. However, above a certain relative humidity, capillary forces due to adsorbed moisture on the carrier surface become the predominant attractive force (99).

The contribution of capillary adhesion to total adhesion force between α-lactose monohydrate and two drugs, salbutamol sulphate and budesonide, was investigated under increasing relative humidity conditions using the AFM (100). While the adhesion forces increased with each incremental rise in humidity for both drugs, the range of relative humidity values for which the adhesion forces increased most drastically was between 15 % and 60 % for the budesonide/lactose combination but above 60 % for the salbutamol/lactose combination. This suggests that the general opinion about the limiting role of capillary forces on particle adhesion below the relative humidity of 65 % was not always applicable (100). Moisture uptake by carrier particles is commonly responsible for particle agglomeration and surface changes but can be prevented by adding magnesium stearate (101). It has been shown that formulations containing magnesium stearate do not show a decrease in FPF with storage at 30 – 40 % RH for 90 days, whereas formulations without magnesium stearate exhibit an 8 % decrease in FPF.

A smoothening process involving the spraying of a 5:3 ethanol–water mixture onto lactose particles in a high shear mixer has been attempted (59). Each spray process was followed by vacuum drying and the cycle was repeated 10 times. The whole process was also carried out with magnesium stearate dispersed in the solvent mixture (59, 90). The shape and size of the particles were retained but the edges were rounded and the surfaces smoother. This was confirmed by the measurement of three roughness parameters: grey level variation in SEM images, R_a using the AFM and specific surface area. The R_a value was significantly reduced, from 110 nm for the untreated lactose to 25 nm for the smoothened lactose. The combined effect of the wetting of particle surfaces and the rolling motion of particles against each other and the mixer wall resulted in superficial dissolution of surface asperities and deposition of dissolved substances into surface fissures. Such particles exhibited improved flow and packing properties.

1.2.4.3 Crystallization

A temperature-controlled micro-crystallisation technique was adopted to modify the nano-scale roughness of α-lactose monohydrate particles (100). Seed crystals produced from a small volume of saturated lactose solution were immersed in a crystallisation vessel containing supersaturated lactose solution. Sub-nanometre scale surface roughness could be controlled by modifying the temperature and degree of supersaturation of the solution. Highly smoothened lactose crystals with R_q of 0.250 nm were produced and used as the substrate in the AFM measurement of the adhesion forces to drug probes under different relative humidity conditions. In another study, α-lactose monohydrate were crystallised from neutralised Carbopol® 934 gels and they exhibited smooth surfaces without detectable roughness under the optical microscope (102). When a sufficiently high concentration of Carbopol® was used, the growing crystals were held within the gel framework and their surface topography was independent of the temperature, duration and concentration of lactose in the gel. In addition to surface smoothness, the harvested crystallised lactose exhibited desirable attributes of DPI carriers such as a narrow size distribution, more uniform shape and better flowability (103). When the smoothened carriers were tested with salbutamol, the FPF increased from 14.7 % to 21.5 % compared to lactose carriers crystallised from aqueous lactose solutions. However, it may also be possible that residual Carbopol® on the surface of the carrier particles had affected drug adhesion properties and this factor cannot be completely ignored.

1.2.4.4 Sieving

Mechanical or air jet sieves are commonly used to produce narrow size fractions of carrier particles as well as to remove surface fines. As a result of the strong adhesion of

fines to coarse particles, both sieving methods caused some reduction in fines but not complete removal as required for effective surface smoothening (50, 95). As the actual amount of fines for surface layering is generally very low, particle size analysis using laser diffraction is not sufficiently sensitive to assess the level of fines remaining. With air-jet sieving, the energy input from the airstream could not efficiently remove surface fines smaller than 4.8 μm, while the concentration of fine lactose (smaller than 20 μm) could be reduced to constant level after a certain duration of air-jet sieving (104). The efficiency of lactose fines removal was shown to be dependent on both the crystal form and the initial amount of fines (31). Anhydrous α-lactose crystals are weaker than α-lactose monohydrate crystals and have a higher tendency to fragment (105).

1.2.4.5 Fluid-bed coating

A reduction in carrier surface roughness was achieved when lactose particles were sprayed with an aqueous solution of lactose and hydroxypropyl methylcellulose in a Wurster coater (50). The surface roughness of lactose was decreased with the increase in surface coating time. The highest *in vitro* FPF of 34.9 % was achieved using particles with the optimal R_a of 610 nm, while particles with R_a above or below 610 nm exhibited lower FPF. It was thought that surface smoothening had not only reduced drug entrapment and adhesion but also decreased the drug-carrying capacity and emitted dose. Hence, the FPF decreased further from 34.9 % to 31.7 % when particles with R_a of 480 nm were tested. However, the presence of hydroxypropyl methylcellulose layer on the surfaces of coated lactose particles could have completely altered the drug-carrier adhesion properties. These findings may not be directly related to the changes in the surface roughness of the lactose particles, which had occurred during the surface coating process. In another study, a precision coater that utilised a swirling air flow pattern in the coating zone was used for surface roughening of lactose particles (48). Coarse lactose

particles were sprayed, with suspensions containing micronized lactose in different isopropyl alcohol/water mixtures. The use of 75 %, w/w of isopropyl alcohol resulted in lactose particles with the highest R_a value of 216 nm, compared to the R_a value of 159 nm for the untreated lactose. In contrast to other studies, the FPF increased linearly with carrier roughness but the emitted dose was relatively unchanged.

1.2.4.6 Dry powder coating

Fine powders can be used to coat coarse particles with the aim of modifying the surface properties of the coarser particles. This can be carried out through either a vigorous mixing process or mechanofusion (22). Fine lactose and magnesium stearate have been the most commonly used coating excipients, with the latter being most notable for its anti-adherent and anti-friction properties. Magnesium stearate has also been reported to reduce both the electrostatic charges (46) and capillary forces (59) between lactose particles so as to promote greater interaction between the fines and coarse lactose carriers (101). Other sugars, such as glucose, mannitol, sorbitol, maltitol, xylitol and trehalose, have also been investigated as powder coating excipients (34, 106-108). Fine excipients have been produced by micronization using various mills, such as ultracentrifuge (106), jet (104, 108, 109) and ball (104) mills. In powder coating by physical mixing, sufficient shear forces are required to break down the cohesive agglomerates and fill the fine particles into surface depressions of the coarse carriers for surface smoothening (49). Various mixing equipment, such as vortex mixers (9, 48, 50, 106), Turbula® mixers (51, 108, 110), shaker mixers (106) and high shear mixers (111), have been used. The identity of the finely-divided excipients (lactose, mannitol or sorbitol) had no impact on the FPF when the concentration of fines was greater than 4.4 %, w/w (108). In one study, the FPF of formoterol fumarate increased linearly with the concentration of lactose fines for up to about 5 %, w/w and decreased thereafter

(101). The increase of FPF was attributed to the reduction in drug entrapment, as well as the formation of mixed agglomerates. In another study, lactose carriers, which were mixed with 10 %, w/w of sucrose tristearate in a high-speed elliptical-rotor type mixer, produced an increase in FPF of salbutamol sulphate from 17.4 % to 46.8 %. In addition to the identity and concentration of fine excipient, mixing process variables, such as the type of mixing equipment, mixing speed (44), order (109) and duration (109, 110, 112, 113), were all found to independently affect the FPF. These variables influenced the magnitude of shear forces during mixing and affected the extent of surface layering, the drug–carrier adhesion, the agglomerate structures and the final organisation of the blend (114).

Both the coarse and fine particles are subjected to intense shear and compression forces in a mechanofusion system (115, 116), where the particles are repeatedly forced through small clearances between the vessel wall and an inner rotating element (117). The high-energy input creates conditions for mechanical fusion of surfaces by solid sintering. The effects of mechanofusion on the surface energy of carrier particles depend on their particle size and the identity of the fine excipient added (118). Magnesium stearate and sucrose stearate had less effect on both the surface properties and inhalation performance of a grade of fine lactose (SorboLac® 400, d_{50} = 10 μm) compared to a coarser lactose grade (Pharmatose® 325M, d_{50} = 60 μm). Coarse lactose carriers that were either mechanofused with magnesium stearate or sucrose stearate resulted in higher dispersibility of drugs in several DPI formulations. It was postulated that mechanofusion had reduced the macro-roughness of the surface, increased the number of microscopic asperities (118) but did not affect the particle size (16). Mechanofusion of micronized drug with fine excipient particles has also been investigated. The process was postulated to (a) overcome strong inter-particulate cohesive forces and reduce the degree of drug

agglomeration, (b) increase the speed of powder fluidisation in the airstream and (c) increase the extent of drug de-agglomeration during aerosolisation (22, 115). Limited size reduction of drug is expected to occur and the most probable physical change is some plastic deformation to produce rounder drug particles (117). The deformation, smearing and fusion of fine excipient on drug particle surfaces may occur. Mechanofusion of 5 %, w/w magnesium stearate with micronized salbutamol sulphate, salmeterol xinafoate, triamcinolone acetonide and budesonide particles have been carried out separately (22, 115). In all instances, the modified drug particles exhibited higher FPF in *in vitro* studies. When observed under the SEM, unmodified particles appeared mainly as agglomerates larger than 10 μm while modified particles formed visibly smaller agglomerates. Significant reduction in powder cohesiveness was further confirmed using flow measurements in a shear cell apparatus. A high degree of drug particle surface modification at the nano-scale was hypothesised to cause the reduction in particle cohesion but this could not be confirmed due to the limited resolution using the SEM.

1.3 Research gaps

Carrier surface roughness has been widely presumed to exert an influence on the fine particle fraction in carrier-based DPI formulations. Fundamentally, the study of surface roughness is a necessary prerequisite for a better understanding of the physical interactions between any two surfaces (drug and carrier) in contact. There have been considerable but varied literature reports on the effect of carrier roughness on DPI performance. These research efforts have largely been disproportionate to the outcomes gained from application of knowledge about carrier surface roughness to the formulation of DPI products. The majority of literature findings are in agreement with the general principles proposed in various carrier surface models (9, 60, 61). These principles are

logically based on the size of drug particles relative to the surface crevices as well as the contact area and adhesion strength between the drug and carrier. While they serve as useful models to rationalize the experimental observations of the *in vitro* performance of DPI formulations, the measurement and interpretation of carrier particle surface roughness itself remains largely as an empirical field of study.

A comprehensive investigation of carrier surface roughness in DPI usually involves three major directions: (a) development of a reliable measurement protocol for particle surface roughness, (b) investigation of the processes by which carrier surfaces can be modified reliably in predictable ways and (c) assessment and rationalization of the *in vitro* performance of inhaled formulations containing carriers with different degrees of surface roughness. The work performed in this thesis will attempt to address the research gaps identified in each of these areas.

1.3.1 Roughness measurement of particulate matter

Surface roughness can be measured either by contact or non-contact profilometry. As discussed in Section 1.2.3, the choice of the measuring equipment will determine the length scale of surface information. Where surface profiling is used for roughness measurement, the AFM has traditionally been preferred due to its high resolution and precision for evaluating nano-scale particle surface features. For carrier particles with very rough surfaces, such as those which are granular in nature, the AFM cannot provide reliable measures of roughness due to limitations in the vertical range of probe deflection. Hence, the AFM might not be a sufficiently versatile tool for the evaluation of a range of carrier particles with widely varying roughness (from atomically smooth to granular rough). One other important consequence of the widespread use of the AFM for roughness evaluation is that most published findings relate more to the nano-roughness

of carriers, rather than their macro-roughness. The relationship between nano-scale surface roughness of carrier and adhesion strength of drug to the carrier is well-established. Relatively less research has been conducted on very rough carriers of granular nature, partly due to the limitations in the methods for roughness measurement. The restricted vertical scanning range may be overcome by the use of non-contact profilometers. The rate of data capture is also much higher when non-contact profilometers are used, compared to the AFM, but the spatial resolution of scans is compromised. Therefore, an in-depth study of carrier macro-roughness may be performed by the selection of an appropriate measurement tool.

There is much subjectivity in the definitions and measurement parameters of particle surface roughness. Due to the scale-dependency of roughness, the measured values seldom contain direct meaningful information unless they are accompanied by the scale of measurement. A review of the literature has shown that DPI carriers normally exist within a narrow size range but roughness values in different reports can span several orders of magnitude. One common observation in this field of roughness measurement research is that roughness values are usually valid only for comparative use when measurements are carried out within the same laboratory and using similar measurement protocols. Unlike the well-established measures of particle size or surface area, these roughness values are often not directly comparable as long as the equipment, measurement and data processing conditions differ. Hence, roughness at different length scales is most commonly described in a qualitative manner, either as macro-, micro- or nano-roughness, rather than in quantitative terms. At the same time, visual information from SEM images are often more informative than the actual roughness values presented. There is a general lack of awareness that the efforts to standardize roughness measurements and calculations are required to confer physical meaning to the values.

Therefore, it is important to investigate the measurement and data processing conditions for the calculation of roughness parameters.

Surface roughness is known to be an intrinsically highly variable characteristic of particles in a population. However, surface roughness, like surface area, is often viewed as a bulk characteristic of the carrier. Each individual carrier particle interacts with many other drug particles and their collective behavior eventually determines the DPI performance. This concept may be better understood by drawing a parallel to the importance of the size distribution, and not only the median size, of particles in determining their bulk properties. Hence, a deeper understanding of surface roughness may be gained by examining the distribution of roughness values in the population of carrier particles.

1.3.2 Creation of rough carrier particles

In order to study the effect of surface roughness on carrier function, different processing methods which give rise to surface modification at different length scales should be available. This would allow the preparation of carrier particles which exhibit a wide span of roughness values, ranging from atomically smooth particles to very rough and irregular particles. Good control of carrier roughness can be achieved using each surface modification process only if the effects of the process parameters on carrier roughness are known. The particle surface modification methods widely reported in literature are predominantly used to induce surface smoothening on carrier particles. The typical crystalline α-lactose monohydrate particles suitable for DPI possess a characteristic tomahawk shape associated with monoclinic crystals. These crystals are regularly-shaped and are generally flat with relatively smooth surfaces. The commonly reported surface smoothening methods involve either the manipulation of the crystallization

conditions of lactose or the controlled dissolution of surface asperities. The methods for surface roughening, on the other hand, have been limited to spray drying to produce spherical particles with wrinkled/dimpled surfaces. There are evidences to suggest that carrier particles with roughened surfaces at a macro-scale result in higher FPF (52, 87) due to a reduction in the drug adhesion to the carrier particles (52). One possible method to induce surface roughening is by the physical aggregation of primary lactose particles to form larger, surface-roughened carrier particles. With careful selection of lactose particle size and processing techniques, it may be possible to design the surface characteristics of carrier particles for use in DPI products.

1.3.3 Relationship between the surface properties and functional characteristics of a carrier

Rougher carrier surfaces are generally considered to possess counteractive effects on drug detachment in a DPI formulation. The concept of cohesive-adhesive force balance has been extensively applied to studies in blend uniformity and drug detachment from the carrier. Researchers have shown that the adhesion strength of drug particles to rougher surfaces was reduced due to reduced contact area. Others have found that rougher carriers increased the emitted dose of drug from the inhaler. Despite these potential positive contributions to the FPF, researchers have also reported that the FPF was decreased when rougher carriers were used. These findings have led some researchers to the compelling argument that a greater degree of drug entrapment in the carrier surface crevices can negate the positive effects of roughened carrier surfaces to reduce drug adhesion. However, this remains inconclusive as there is a lack of clear physical evidence to show that more drug particles are truly entrapped on roughened surfaces. A logical outcome of this argument is that there exists an optimal carrier surface roughness that balances the reduction of adhesion force and the degree of drug

entrapment. In order to establish the optimal surface roughness, investigations of the *in vitro* performance of DPI formulations containing very rough carriers will also be necessary. Finally, the surface distribution of drug particles on carriers with varying surface roughness may be investigated using both visual and chemical imaging methods. These imaging tools may be used to ascertain whether the distribution of drug particles on carriers is altered by the carrier surface roughness.

CHAPTER 2

HYPOTHESES AND OBJECTIVES

2 HYPOTHESES AND OBJECTIVES

The research work carried out in this thesis was aimed at developing strategies to quantify and to modify surface roughness of lactose carrier particles for use in DPI formulations. Lactose monohydrate was selected as the carrier material for study primarily due to its widespread regulatory acceptance as well as the limited choice of carrier excipients as suitable alternatives. Much contradicting evidence still exist regarding the extent of carrier surface 'smoothness' or 'roughness' that is most ideal for maximizing the FPF. It is not uncommon for commercial lactose carrier-based DPI products to exhibit FPF of less than 50 %, with many in the 10 – 20 % range. Surface modification of lactose carriers was an attempt to address the pressing concerns of the low FPF of commercial lactose carrier-based DPI products. Therefore, the main hypothesis of this work is that lactose carrier particles, when roughened using suitable processing methods, can improve the release characteristics of micronized drug during aerosolization from an inhaler device.

Studies with the following objectives were conducted to test the research hypothesis:

A. To investigate the reliable image processing techniques for particle surface roughness using optical profilometry
B. To investigate the feasibility of preparing roughened carrier particles by surface coating and by compaction
C. To evaluate the *in vitro* dry powder inhaler performance of carriers with different degrees of surface roughness
D. To investigate the surface distribution of micronized drug particles in carriers of different surface roughness using Raman spectroscopy

The studies were organized into three parts:

Part 1. Investigation of the measurement criteria and image processing techniques for reliable attributes to quantify surface roughness of particulates by optical profilometry

Part 2. Investigation of two methods to prepare roughened lactose carrier particles

A. Fluid-bed coating

B. Dry granulation by roller compaction

Part 3. Investigation of the use of roughened lactose carriers in dry powder inhaler formulations:

A. Evaluation of the *in vitro* fine particle fraction and aerodynamic particle size distribution in interactive mixtures containing roughened lactose carriers

B. Investigation of the surface distribution of micronized drug particles on roughened lactose carriers using Raman spectroscopy

CHAPTER 3

EXPERIMENTAL

3 EXPERIMENTAL

3.1 Part 1: Investigation of the measurement criteria and image processing techniques for reliable attributes to quantify surface roughness of particulates by optical profilometry

3.1.1 Rationale of study

The literature review suggests that roughness measurements are closely related to: (a) the length scale at which measurements were made and (b) the image processing techniques performed on the raw surface profiles before determination of roughness parameters. A surface can be composed of features at different length scales, ranging from the visible surface textures down to the atomic level structures (119). Unless these measurement conditions are properly defined, measurements of roughness values and trends observed may not be reproducible and the reported measurement values hold little significance to other researchers. Two batches of carrier particles (roughened and smoothened) were produced by fluid-bed coating and the influences of the following conditions on roughness values were examined: filter wavelengths, surface tilt, image size and sample size.

3.1.2 Surface modification of lactose particles by fluid-bed coating

Surface modification was conducted using a fluid-bed coater, comprising the Flexstream™ module, mounted on an air handling system (MP-1, GEA Aeromatic Fielder, UK). The photograph of the fluid-bed coater is shown in Figure 5A. The two-fluid spray nozzle for delivery of the coating liquid is located at the side of the product chamber. A non-sifting gill plate (Figure 5B) distributes air from the bottom of the chamber in a swirling flow pattern, which contributes to directional mass flow and improves the drying efficiency during coating.

(A)

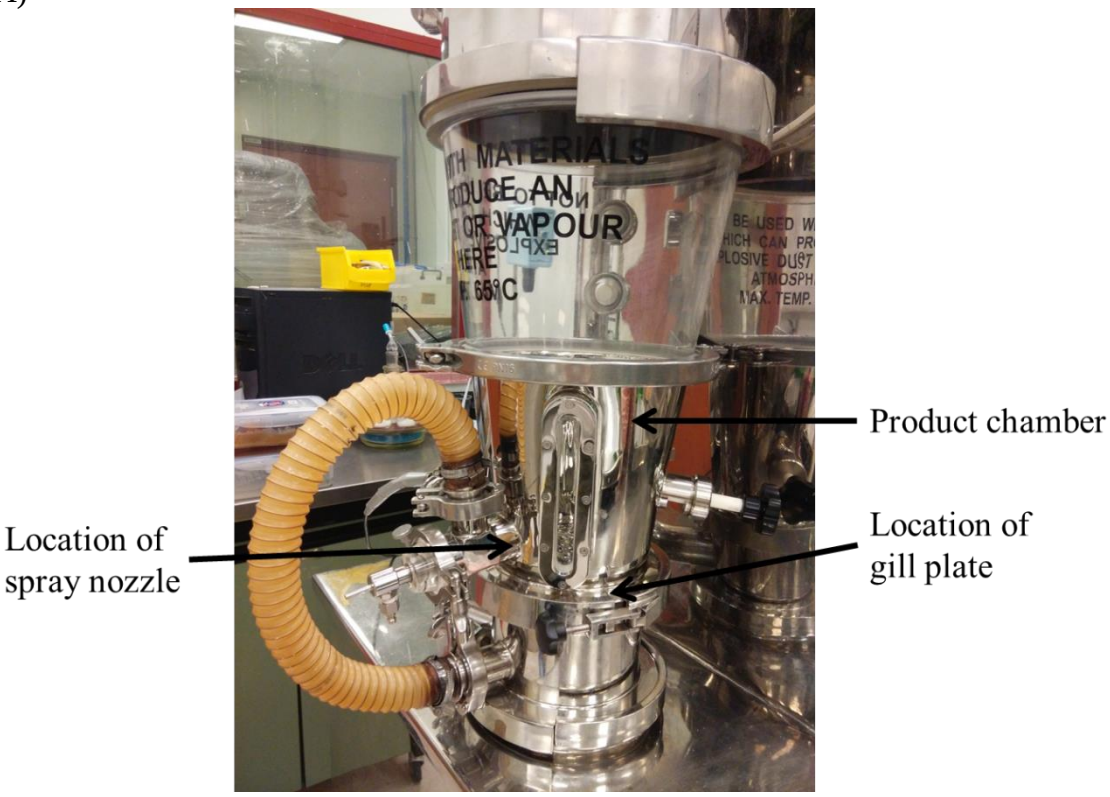

(B)

Figure 5. Photographs showing (A) the fluid-bed coater with the Flexstream™ module and the location of the spray nozzle relative to the fluidizing bed, and (B) the non-sifting gill plate that distributes air in a swirling flow pattern in the product chamber.

The powder feed for fluid-bed coating consisted of 2 kg of lactose powder (d_{50} = 154 µm; lactose 100M; SpheroLac® 100, Meggle, Germany). Micronized lactose was produced by jet milling (100 AFG, Hosokawa Micron, Germany) lactose 100M at a grinding air pressure of 4 bars and classifying wheel speed set at 15000 rpm. The jet mill consisted of a milling chamber, also called the grinding zone, integrated with a powder classifying system. During jet milling, milled lactose particles from the milling chamber were continuously conveyed by air to the vicinity of the classifying wheel rotating at 15000 rpm. Milled particles smaller than a certain cut-off diameter were removed by the classifying wheel with the exiting air flow and conveyed into the product-collecting bin. The rotation speed of the classifying wheel determined the cut-off diameter of the milled particles collected. The higher the classifying wheel speed, the smaller the cut-off diameter and the particle size of the milled lactose collected. Prior milling trials were conducted in order to optimize the grinding air pressure and classifying wheel speed so that micronized lactose with d_{50} of 2 µm were obtained for use in fluid-bed coating.

Liquid suspensions of micronized lactose were prepared immediately before use and sprayed onto the powder feed in the fluid-bed chamber. The spray liquids were prepared by dispersing 15 %, w/w micronized lactose in the suspension liquid. The suspension liquid consisted of a combination of isopropyl alcohol (IPA; Aik Moh Paints and Chemicals, Singapore) and water in a 3:2 (v/v) ratio, which was previously saturated with lactose. This IPA/water ratio was selected as it has been shown in previous work to result in the greatest increase in surface roughness compared other volume ratios (48). The saturated solution was first prepared by adding excess fine lactose (lactose 400M; Sorbolac® 400, Meggle, Germany) into the IPA/water combination, stirring the mixture for at least 24 hours and filtering through a 0.45 µm membrane filter. A 600 g spray liquid was prepared and used to spray on the powder feed to produce roughened lactose

particles. Smoothened lactose particles were also prepared in the same manner, except that the spray liquid used was a saturated lactose solution, without any dispersed micronized lactose added.

During fluid-bed coating, the inlet airflow rate was maintained between 70 – 100 m^3/h, just sufficient to ensure the complete fluidization of the powders in the fluid-bed chamber. The inlet air temperature was maintained at 60 °C throughout fluid-bed coating. The spray liquid was delivered using a two-fluid spray nozzle with 0.5 mm diameter at an atomizing pressure of 2.5 bars. The spray rate was kept between 10 - 15 g/min to achieve the steady state product temperature of about 30 °C throughout the process. After all the spray liquid was delivered, the product was further fluidized until the product temperature reached 45 ºC. All the powders in the fluid-bed chamber was collected and passed through a powder classifying system (50 ATP, Hosokawa Micron Ltd, Germany) with the classifying wheel speed set at 7500 rpm. The purpose of this step was to rapidly remove the micronized lactose which did not successfully adhere onto the feed particles. The rotation speed of the twin screw feeder of the classifying system was set at 3 rpm, which corresponded to the material feed rate of approximately 26 g/min. Similar to the jet milling process, lactose fines were removed by the classifying wheel with the exiting air flow. The remaining particles, with the fines removed, were conveyed by gravity into a product-collecting bin.

3.1.3 Air-jet sieving

The lactose particles produced in Section 3.1.2 were further fractionated using the air-jet sieve (Hosokawa Micron, USA). A 30 g powder sample was placed on a 180 µm aperture size sieve and the sieving process carried out for 15 min. The powder which passed through the sieve apertures was transferred to a 125 µm aperture size sieve and

sieving was carried out for another 15 min. The coarse carrier particles retained on the 125 µm aperture size sieve, which fell within the size range of 125 – 180 µm, were collected for further analysis.

3.1.4 Scanning electron microscopy

The lactose particles were sprinkled on carbon tape and their surface morphologies were examined under the SEM (JSM-6010LV, JEOL, Japan) using an accelerating voltage of 1.2 kV.

3.1.5 Surface profiling of coarse lactose carrier particles

3.1.5.1 Acquisition of surface images

Particle surfaces were profiled using an optical profiler (Wyko® NT1100 Optical Profiling System, Veeco, USA) using the white light vertical scanning interferometry mode (Figure 6). An interferometer was present together with the magnification objective for the mapping of 3D surface profiles of the particulates. The optical profiler was placed on an air table maintained with 3 bars of air pressure to isolate the instrument from vibrations arising from the surroundings. Surface images of 109 µm x 144 µm were captured using a 2.0x field-of-view lens and 20x objective lens. Each raw surface profile was captured and displayed on the Wyko® Vision® 3.0 software without any prior processing of the image. All further image processing operations, including the roughness calculations, were conducted using the same software and are described in detail in the subsequent sections.

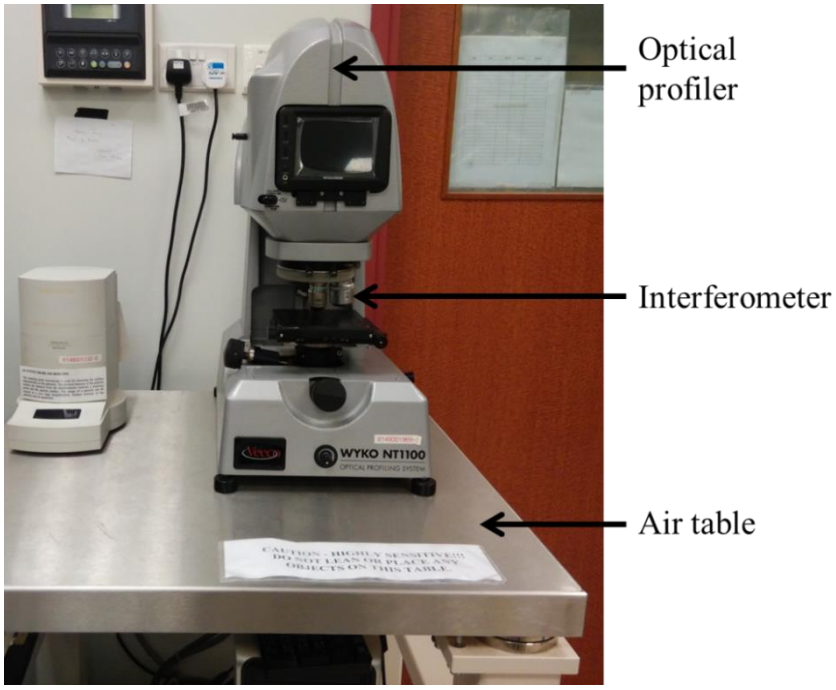

Figure 6. The optical profiler, which was placed on an air table, was used for surface roughness measurements in this study.

3.1.5.2 Assessment of surface features using power spectral density plots

The total surface information, including the shape, waviness and roughness, of the roughened and smoothened coarse lactose carrier particles were first examined using the power spectral density (PSD) plots. A total of five randomly selected particle surface images from each batch of carrier particles was analysed. One PSD plot was obtained for each surface image by Fourier decomposition of the measured surface profile into several sine waves with different spatial frequencies (120). Each sine wave has its corresponding amplitude, phase and frequency. The PSD is therefore a plot of the power of the signal, which is a square function of the surface heights, per unit spatial frequency against the spatial frequency (1/μm). The units of PSD can be simplified from $nm^2 \cdot \mu m$ into nm^3 but it is not related to actual physical volumes. These plots describe the variation of the surface heights with increasing spatial frequency. Surface features of

lower spatial frequencies are more widely-spaced while those of higher frequencies are more closely-spaced. The PSD plots were used in the data pre-processing stage for visually examining the variation of surface heights at different length scales on the surface. The lower limit of the spatial frequency that could be analysed was limited by the largest size of the image (approximately 100 μm x 100 μm) while the upper limit was determined by the lateral resolution of the optical profiler. The lateral optical resolution was 0.75 μm when the 20x objective, with a numerical aperture of 0.4, was used for surface profiling. By obtaining the reciprocals of these upper and lower limits, the useful range of values on the x-axis on the PSD plots for meaningful analysis was about 0.01 – 1.5 (1/μm).

3.1.5.3 Application of digital filters on surface images

A total of 50 sub-regions of the surface images of various sizes (10 x 10 μm^2, 20 x 20 μm^2 and 30 x 30 μm^2) were randomly selected from the two carrier batches. Digital filtering was applied on all sub-regions before the surface parameters were derived. In the digital filtering process, three different types of filters could be used: the high-pass, band-pass and low-pass filter. The purpose of applying these filters was to separate the surface features of different length scales, which collectively made up the raw surface profile. The transmission characteristics of the three different filters are shown in Figure 7. After the application of a low-pass filter, only the surface features of longer wavelengths were retained in (or transmitted to) the filtered profile, indicating the overall shape of the surface. Conversely, only the surface features of shorter wavelengths were retained in the filtered profile when the high-pass filter was used. The band-pass filter was used to suppress the surface features of both longer and shorter wavelengths, so that the features that were of intermediate wavelengths were retained. The three different filters were defined by the value(s) of the cut-off spatial frequencies being set and were

applied individually, where appropriate. The cut-off frequency is the frequency at which 50 % of the amplitude of the surface height is being transmitted. The cut-off frequency was set at below 0.1 μm^{-1} for the low-pass filter, 0.1 – 1.5 μm^{-1} for the band-pass filter and greater than 1.5 μm^{-1} for the high-pass filter. The Gaussian filtering window was selected for this study and the standard deviation of the filters was set at 2 x 10^{-4} μm^{-1}. Hence, for the band-pass filter, the width of the filter was much smaller than the bandwidth of the filtered profile. In terms of physical length scales, the filters were used to extract surface features that were of length scales of either smaller than 0.66 μm, 0.66 – 10 μm or greater than 10 μm along the horizontal plane on the surfaces. These cut-off filter values were selected on the basis of the typical size of the micronized drug particles in DPI formulations. It was felt that surface features which were most important in drug-carrier interactions were of a similar length scale corresponding to the size range of the drug particles.

Histogram plots were also constructed to aid in the visualization of changes in the surface height distributions after the application of digital filters with different cut-off frequencies. Each surface image is a digital image and each pixel on the image has a corresponding surface height value assigned to it. The distribution of surface heights in each image was presented in the histogram plots. The changes in the distribution of the surface heights were analysed after different filters were applied on the raw surface profiles. In addition to digital filtering, the effect of the removal of tilt on surface topology was also studied. Where the tilt removal function in the software was used, linear tilt from the surface image was removed using a least-squares fitting technique. This involved the fitting of a plane to the data points on the original surface image and the subtraction of the fitted plane from this image, so that the tilt can be removed in the processed image.

(A)

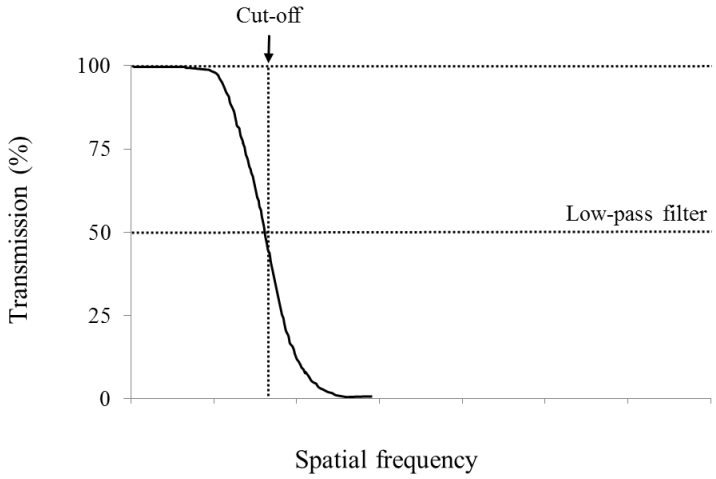

(B)

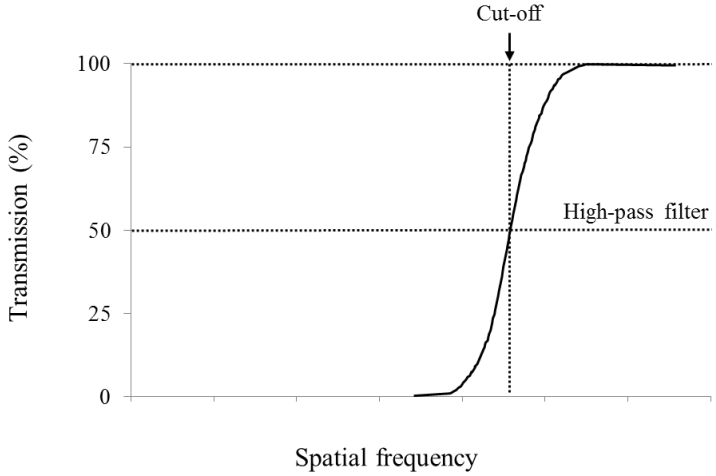

(C)

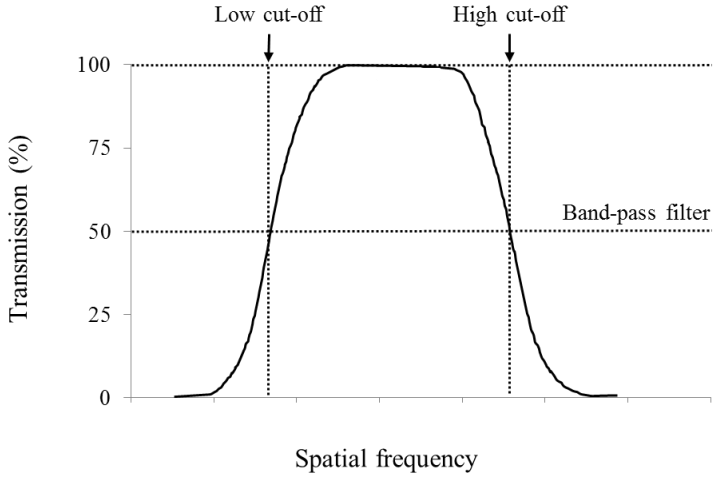

Figure 7. Graphs showing the transmission characteristics for the (A) low-pass, (B) high-pass and (C) band-pass filters.

3.1.5.4 Calculation of surface roughness parameters

Particle surface roughness was characterized using two roughness parameters. The arithmetic mean roughness, R_a, represents the average height deviation of the surface profile from the mean surface. The root-mean-square roughness, R_q, represents the standard deviation of the surface heights with reference to the mean surface. The mean surface refers to the horizontal plane that divides the surface profile equally above and below the plane. Since 3D surface images were obtained using optical interferometry, 3D roughness parameters were digitally approximated using 2D assessments and they were calculated by the following equations:

$$R_a = \frac{1}{m \cdot n} \cdot \sum_{i=1}^{m} \sum_{j=1}^{n} \left| Z_{ij} \right| \quad (1)$$

$$R_q = \sqrt{\frac{1}{m \cdot n} \cdot \sum_{i=1}^{m} \sum_{i=1}^{n} Z^2(x_i, y_j)} \quad (2)$$

where m and n are the number of pixels in the image array in the x and y directions, respectively. Z is the local value of the surface height, relative to the mean surface, at each grid point.

3.1.5.5 Determination of the sample size for roughness measurements

A total of 400 surface images of area 20 x 20 μm^2 was obtained using the smoothened particles. During the surface profiling, the stage was moved in a systematic pattern to ensure that no overlapping surface images were collected. The R_a and R_q values were then calculated for each surface image, after the application of the band-pass filter as described in Section 3.1.5.3. In order to determine a suitable sample size (N) for the calculation of roughness parameters, moving averages of R_a and R_q were calculated using different values of N. Using N = 20 as an example, the 1st element of the moving

average is the average of the first 20 values, while the 2^{nd} element is the average of the 2^{nd} – 21^{st} value in the series. The process was repeated for the entire series of 400 R_a and R_q values. The 400 values were used in the same order that they were collected and the series was assumed to be in randomized order since the carrier particles were randomly orientated on the measurement stage. The N values investigated were 20, 60, 80, 120, 150, 200 and 250.

3.2 Part 2: Investigation of two methods to prepare roughened lactose carrier particles

3.2.1 Part 2A: Fluid-bed coating

3.2.1.1 Rationale of study

The research work conducted in Part 1 of this study has shown that lactose particles were successfully roughened after fluid-bed coating. As the carrier particles in a DPI formulation have commonly been reported to exist in a wide size range of 40 – 200 μm, it was of interest to investigate whether the fluid-bed coater was capable of roughening lactose particles in this wide size range. Surface roughening of lactose particles by the fluid-bed is a coating process and its efficiency depends on sufficient separation of individual particles during fluidization and good powder movement around the spray zone. This in turn is largely dependent on the cohesiveness of powder particles, a property closely linked to the particle size and size distribution of the powder to be coated.

In order to produce roughened particles in different size ranges, the following approaches were considered. The first approach was to coat coarse lactose particles of various narrow size ranges with micronized lactose. The second approach was to coat coarse lactose particles of a wider size range with micronized lactose, followed by fractionation of the coated particles into carriers of different size ranges. Based on literature reports, potential segregation of particles based on their size in the fluidization chamber can possibly lead to the non-uniform surface roughening effect of different-sized particles, depending on the location of the spray nozzle relative to the fluidizing bed. This is especially true when coating is carried out in the top-spray and bottom-spray Wurster fluid-bed coaters. Therefore, this study aimed to investigate whether (a) there were differences in the surface roughening effect when feed particles of different sizes

were used during fluid-bed coating in the Flexstream™ module, with a size-spray nozzle, and (b) the surfaces of particles of different sizes, but within the same processed batch, were roughened to different extents.

3.2.1.2 Preparation of lactose feed particles

Lactose 100M was used as received (denoted as feed P1) while lactose 140M (GranuLac® 140, Meggle Pharma, Germany) was fractionated by classification before use in the coating process. Lactose 140M was passed through the classifying system using the classifying wheel speed of 7500 rpm and the material feed rate of 26 g/min. The coarser particles, with fines removed, in the product-collecting bin were collected and denoted as feed P2. The classifying wheel speed of 7500 rpm was determined from preliminary studies to remove fines below 5 µm from the classified powder (i.e., d_3 = 5 µm). A portion of feed P2 was further fractionated by passing through the classifying system using a classifying wheel speed of 2000 rpm. The classifying wheel speed of 2000 rpm was determined from preliminary studies to result in the removal of particles smaller than 100 µm. The coarser fraction was discarded while the smaller-sized fraction (i.e., d_{97} = 100 µm) was collected and denoted as feed P3. The particle sizes and size distributions of the three feed powders are shown in Table 1. All particle size measurements were conducted as described in Section 3.2.1.5.1. Micronized lactose with d_{50} of 2 µm was also prepared as described in Section 3.1.2.

3.2.1.3 Surface modification of lactose particles by fluid-bed coating

The surface modification process was conducted as described in Section 3.1.2 and the powders for coating and spray liquids used are shown in Table 2. Roughened particles were produced by delivering the spray liquids containing 15 %, w/w of micronized lactose while smoothened particles were produced by delivering only saturated lactose

solutions, without any dispersed micronized lactose. For feed P1, a spray liquid with 5 %, w/w micronized lactose was also used to produce particles of intermediate roughness. As the specific surface areas of feed P2 and P3 were approximately twice (pre-determined, Section 3.2.1.5.3) that of feed P1, the masses of spray liquids used had to be doubled to 1200 g. After fluid-bed coating, the collected powders were passed through the powder classifying system with the classifying wheel speed of 7500 rpm and the material feed rate of 26 g/min, to remove loose fines.

3.2.1.4 Air-jet sieving

The carrier particles produced in Section 3.2.1.3 were fractionated by air-jet sieving as described in Section 3.1.3, using sieves of aperture sizes, 180, 125, 63 and 38 µm. The duration of sieving was kept at 15 min for each sieve. Particles of three size fractions, 125 – 180 µm (fraction A), 63 – 125 µm (fraction B) and 38 – 63 µm (fraction C), were obtained. Figure 8 summarises the different size fractions of lactose particles obtained from the various feed powders after fluid-bed coating. Carrier particles of fractions A and B were obtained when feed P1 was used while fractions B and C were obtained when feeds P2 and 3 were used. The roughness of the carrier particles (smoother, intermediate or rougher) were denoted based on the amount of micronized lactose sprayed onto the particles.

3.2.1.5 Physical characterization of lactose carriers

3.2.1.5.1 Particle size

Lactose particles were suspended in IPA and sized in a laser diffraction particle sizer (Small Volume Module, LS 230, Beckman Coulter, USA). The d_x value corresponded to the X^{th} volume percentile under the cumulative undersize distribution curve. The particle size distribution was expressed in terms of span and was calculated as:

$$\text{Span} = (d_{90} - d_{10}) / d_{50} \quad (3)$$

A larger span value indicates a broader particle size distribution.

3.2.1.5.2 Surface roughness

Surface images of the lactose particles were captured as described in Section 3.1.5.1. A total of 150 surface images of size 20 x 20 μm^2 was obtained for each batch of lactose carrier. A band-pass filter with cut-off spatial frequencies of 0.1 and 1.5 μm^{-1} was applied to each surface image and the R_a was calculated as described in Section 3.1.5.4. The coarse carriers were also viewed under the SEM and the images obtained for qualitative surface analysis.

Table 1. Size characteristics of feed powders used in fluid-bed coating

Lactose grade	Fractionation criteria	Particle size (μm)			Span
		d_{10}	d_{50}	d_{90}	
100M	As received[a]	89 (1)	154 (1)	225 (1)	0.88
140M	As received	6 (0)	28 (1)	74 (1)	2.43
	Classified - 7500 rpm[b]	16 (1)	48 (1)	116 (4)	2.08
	Classified - 7500 rpm followed by 2000 rpm[c]	19 (2)	47 (4)	86 (0)	1.43
Micronized	Air-jet milled - 15000 rpm[*]	1.1 (0.1)	2.2 (0.2)	4.2 (0.2)	1.41

[a,b,c]Denote feed P1, P2 and P3, respectively
[*]Denotes micronized lactose dispersed in spray liquid
Values in parentheses represent the respective standard deviation

Table 2. Powders for coating and spray liquids used in fluid-bed coating

Feed	Specific surface area of feed (m^2/g)	Concentration of micronized lactose in spray liquid (%, w/w)	Total mass of spray liquid delivered for a 2 kg feed (g)
P1	0.236	0, 5, 15	600
P2	0.440	0, 15	1200
P3	0.447	0, 15	1200

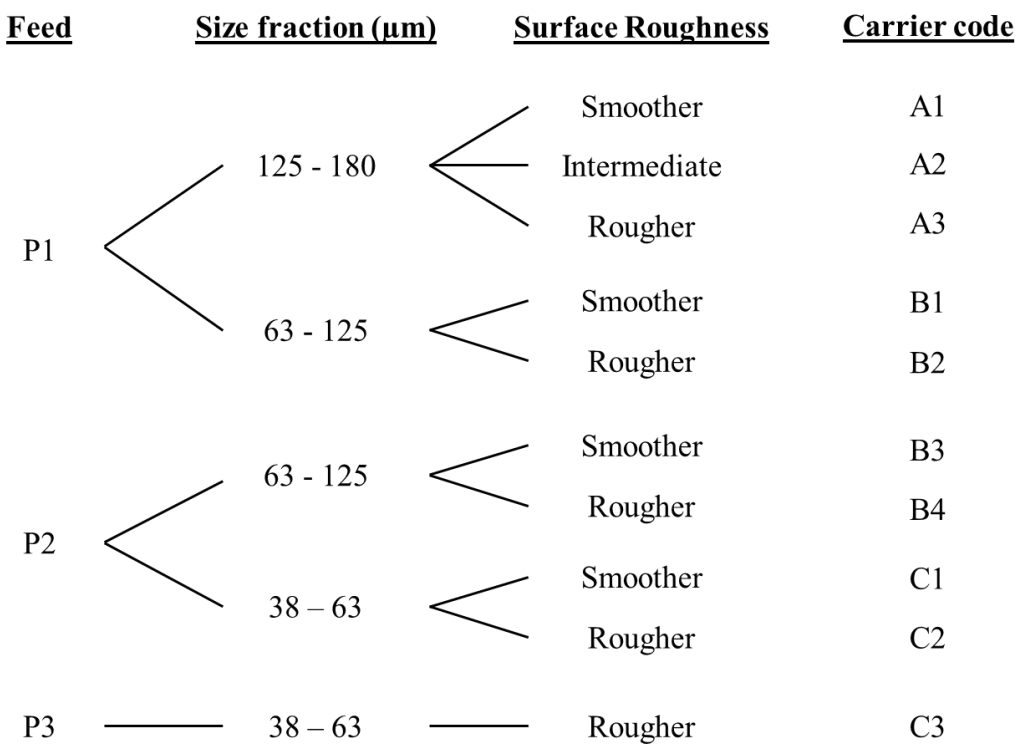

Figure 8. Chart showing the various size fractions and surface roughness of carrier particles which were obtained, by air-jet sieving, from different feed powders after fluid-bed coating.

3.2.1.5.3 Specific surface area

The multi-point BET specific surface area (expressed as m^2/g) was obtained using a surface area analyser (SA 3100, Beckman Coulter, USA) with nitrogen as the adsorbate gas. Vacuum out-gassing was conducted for 15 hours with a furnace temperature of 70 °C to remove residual moisture from the particles prior to surface area analysis.

3.2.2 Part 2B: Dry granulation by roller compaction

3.2.2.1 Rationale of study

In previous work, fluid-bed coating of coarse lactose particles resulted in modification of the small-scale roughness of the particle surfaces. The coated coarse lactose particles retained their general crystal morphologies and were typically tomahawk in shape with flat and planar surfaces. Roughened particle surfaces were due to attachment of the micronized lactose particles on the coarse lactose particles, creating areas on the particle surfaces with micro-scale surface roughness. In order to create particles with a higher degree of surface roughness, the application of compaction forces on the particles may be useful to disrupt the regular crystal structure of the particles. Tablet formation and roller compaction are two common pharmaceutical processes where high compaction forces are applied onto powder materials to form compacts. Compared to tableting, roller compaction offers greater flexibility in powder processibility in terms of the powder flow characteristics. This is because a screw feeder is typically present in a roller compactor to aid in feeding of materials into the compaction zone and no high speed die-filling is required.

Roller compaction was adopted as an alternative method to increase the R_a values of lactose particles by creating macro-scale roughness through compaction of particles. This part of the study investigated the influence of lactose powder properties, such as particle size and flow, and roller compaction parameters on the degree of surface roughening of lactose particles.

3.2.2.2 Preparation of powder blends

Prior to use, all powders were manually sieved using a 355 μm aperture size sieve, to remove or break up any large agglomerates. Lactose 100M, 200M (GranuLac® 200,

Meggle, Germany) and 400M powders were blended in different mass proportions as shown in Table 3. All powders were blended in a double cone blender (AR 400, Erweka, Germany) rotated at 10 rpm for 15 min. Blending was performed immediately before a powder was roller compacted or used for analysis.

3.2.2.3 Physical characterization of powder blends

3.2.2.3.1 Particle size

The particle size of each powder blend was measured as described in Section 3.2.1.5.1.

3.2.2.3.2 Hausner ratio

Bulk and tapped densities of each powder blend were determined for the calculation of the Hausner ratio. The powder was first passed through a sieve of aperture size 1.7 mm into a 100 mL graduated cylinder. The top of the powder was gently levelled with a spatula, powder adhering dusted off and the mass of powder in cylinder accurately weighed. The powder in the graduated cylinder was then mechanically tapped to a constant volume using a tap density tester (Sotax TD2, Switzerland). The final tapped volume was noted and used to calculate tapped density. The Hausner ratio was calculated as follows:

$$\text{Hausner ratio} = \frac{\text{Bulk volume } (\text{cm}^3)}{\text{Tapped volume}(\text{cm}^3)} \quad (4)$$

The value of Hausner ratio was always greater than 1 and larger values indicate poorer powder flow characteristics.

Table 3. Powder blends comprising different mass proportions of lactose 100M, 200M and 400M which were used in roller compaction

Blend code	Percentage by weight (%, w/w)		
	Lactose 100M	Lactose 200M	Lactose 400M
F1	100	-	-
F2	75	25	-
F3	75	-	25
F4	50	50	-
F5	25	75	-
F6	-	100	-
F7	50	-	50
F8	25	-	75

3.2.2.3.3 Basic flowability energy and specific energy

Flow properties of the lactose powder blends were measured using the FT4 powder rheometer (Freeman Technology, UK), equipped with a split vessel with volume of 160 mL and diameter of 50 mm. Each powder sample was first conditioned by a 48 mm helical blade (Figure 9) to achieve a reproducible and low stress packing state. In the conditioning cycle, the blade traversed downwards, followed by upwards, through the powder bed to create a standardised packing state. This was followed by the test cycle, in which the helical blade traversed downward through the powder bed. The axial and rotational forces acting on the blade were measured continuously and used to derive the total energy consumed in driving the blade downward through the powder bed. The total energy was recorded as the basic flowability energy (BFE). The specific energy was

derived as the energy expended per unit weight of powder during the upward movement of the blade.

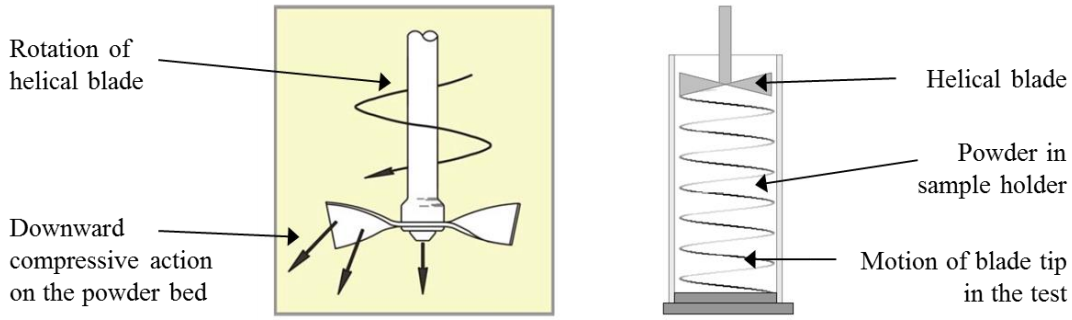

Figure 9. Diagram showing the movement of the helical blade during the flowability test in the FT4 powder rheometer and the compressive action on the powder induced by the blade.

3.2.2.3.4 Cohesion

Powder cohesion was measured using the shear cell module of the FT4 powder rheometer, equipped with a split vessel with volume of 85 mL and diameter of 50 mm. A pre-shear stress of 9 kPa was applied on the powder using a vented piston after the powder was conditioned. A shear head consisting of 18 vertical blades was inserted into the powder and used to apply a series of normal stresses on the powder. After each normal stress was applied, the shear head was rotated slowly and the maximum shear stress was recorded when the powder bed began to shear. The shear stresses of the powder were determined at normal stress values of 3, 4, 5, 6, and 7 kPa. The yield locus was the best-fit line constructed on the plot of shear stress against normal stress. Powder cohesion was obtained from the intercept of the yield locus with the y-axis (i.e., at normal stress = 0 kPa).

3.2.2.3.5 Angle of repose

The angle of repose was determined in a powder tester (PT-N, Hosokawa Micron, Japan). The powder was placed on a vibrating sieve with 1.0 mm apertures and fell gradually through the sieve apertures to form a conical heap on a circular base with diameter of 80 mm. The angle of repose was calculated as the angle between the slope of the conical heap relative to the horizontal base. Generally, smaller angles of repose indicate powders with better flow characteristics.

3.2.2.4 Surface modification of lactose particles by roller compaction

3.2.2.4.1 Roller compaction

The roller compactor (Pharmapaktor L200/30P, Hosokawa Bepex, Germany) used in this study (Figure 10) consisted of 2 fixed rolls with diameters of 200 mm and reduced roll widths of 30 mm. The roll width was reduced to customize the regular production machine for research use. The surfaces of both rolls contain serrations which were cut across the roll width. The maximum depth of the serrations is approximately 0.35 mm while the spacing between adjacent serrations is approximately 1.7 mm (121). A powder hopper houses a vertical feed screw above the rolls which was used to deliver powder material into the compaction zone between the rolls. The roll speed and screw speed could be varied from 2.6 – 20 rpm and 8 – 73 rpm, respectively. The normal operating range of roll force was 0 – 67 kN/cm, beyond which the protective automated shut-down would be activated to stop the compaction process.

Each powder blend was fed into the roller compactor while it was operating in the automatic mode. The roll speed was set at 2.4 rpm. Compacted ribbons were produced at 3 different roll forces, where possible: 10, 20 and 30 kN/cm. In the automatic mode, the

(A)

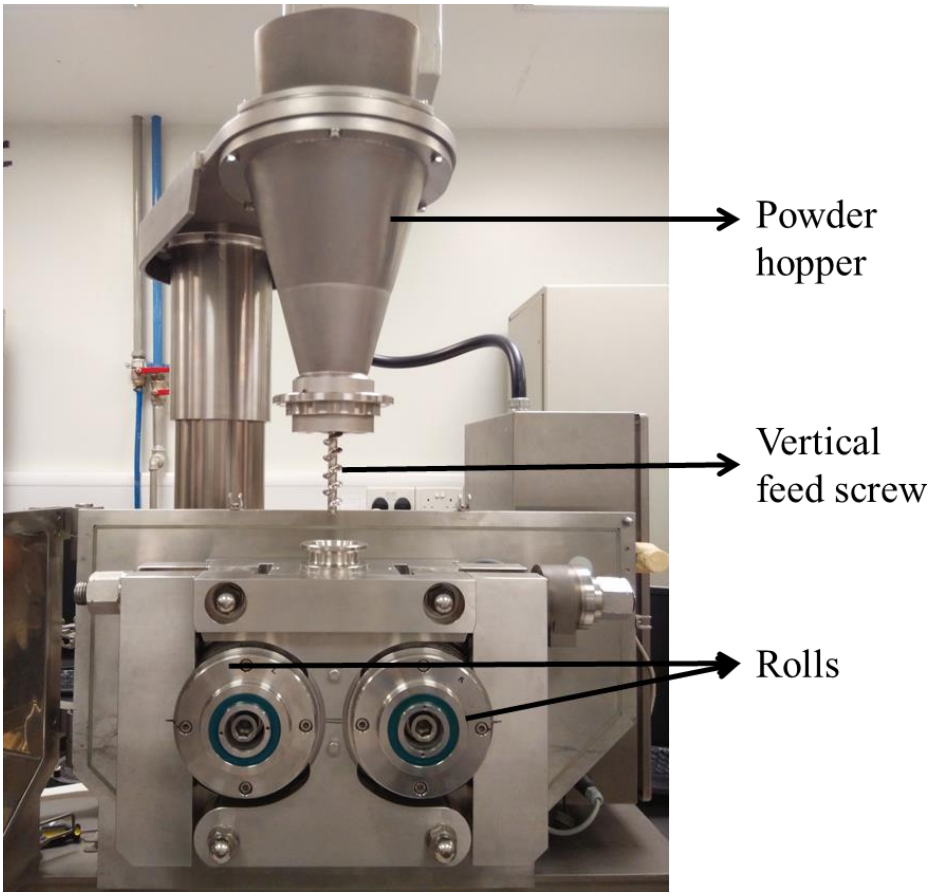

(B)

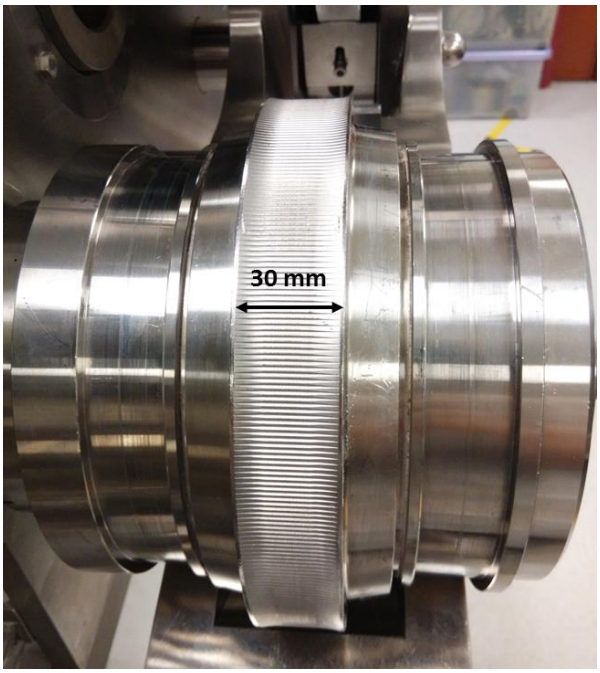

Figure 10. (A) The roller compactor used for the preparation of roughened lactose carrier particles in this study, equipped with (B) serrated rolls having reduced surface widths of 30 mm.

feed screw speed was automatically adjusted by a feedback mechanism to maintain the set roll force. During roller compaction, the roll force, screw speed and roll speed were recorded (Labview 6.0, US) at 1 s intervals. The success or failure of the compaction experiments conducted using different powder blends at various roll forces are presented in Table 4. For certain combinations of powder blend and roll force, the target roll force could not be achieved despite using the lowest roll speed and highest screw speed during compaction. These were denoted as failed compaction runs. All compacted ribbons were collected and manually sieved with a 1.4 mm aperture size sieve to remove any fines before they were further processed.

Table 4. Compaction runs for different powder blends at various roll forces

Blend code	Target roll force used in compaction (kN/cm)		
	10	20	30
F1	✓	✓	✓
F2	✓	✓	✓
F3	✓	✓	✓
F4	✓	✓	-
F5	✓	✓	-
F6	✓	✓	-
F7	✓	-	-
F8	✓	-	-

✓ indicates successful compaction run; - indicates failed compaction run

3.2.2.4.2 Milling and sieving of carrier particles

All roller compacted ribbons were milled in a conical screen mill (Quadro Comil®, Canada). The ribbons were first milled using a grater screen of aperture size 2007 μm, followed by a second grater screen of aperture size 457 μm. A teethed round impeller was used in the first milling step, followed by a round impeller (without teeth) in the second milling step. The impellers were rotated at a speed of 1250 rpm during milling. Carrier particles within the size range of 63 – 125 μm were obtained from the milled material by air-jet sieving. Two control carriers were also air-jet sieved to allow for comparisons with the roller compacted particles. The control carriers consisted of raw lactose 100M, which was not processed by roller compaction, and an inhalation-grade carrier lactose (InhaLac® 230, Meggle Pharma, Germany), denoted as L100M and INH, respectively.

3.2.2.5 Measurement of surface roughness

The measurement of particle surface roughness was carried out as described in Section 3.2.1.5.2.

3.2.2.6 Statistical analyses

One-way analysis-of-variance (ANOVA) was carried out using XLSTAT (Addinsoft, USA) to determine whether the compaction force resulted in statistically significant differences in the mean R_a of the different carrier batches. Post-hoc analysis using the Scheffé's method was then used to identify statistical differences between each pair of mean R_a values.

3.3 Part 3: Investigation of the use of roughened lactose carriers in dry powder inhaler formulations

3.3.1 Part 3A: Evaluation of the *in vitro* fine particle fraction and aerodynamic particle size distribution in interactive mixtures containing rough carriers

3.3.1.1 Rationale of study

In the previous study, two methods of surface roughening, namely fluid-bed coating and roller compaction, were explored. The percentage increase in R_a ranged from about 20 – 60 % after fluid-bed coating and roughness was due to sintering or physical attachment of micronized lactose on the coarse carrier surfaces. On the other hand, significantly rougher carriers which were granular and irregularly-shaped were successfully prepared by roller compaction. The experimental conditions for the preparation of carriers with suitably high R_a values were identified in both methods. Based on the results from Part 2 of the thesis, carrier particles with R_a values spanning a range from about 400 – 1200 nm were prepared using appropriate experimental methods and conditions. The *in vitro* performance of the DPI formulations containing these surface-modified carriers, including the FPF and aerodynamic particle size of released drug, was evaluated using the Next Generation Impactor (NGI).

3.3.1.2 Preparation of lactose carriers

Surface modification by fluid-bed coating was conducted as described in Section 3.2.1.3 using feed P1. Roughened fluid-bed coated carrier particles (denoted as FB_R) were obtained by spraying of 15 %, w/w micronized lactose dispersion while smoothened carrier particles (denoted as FB_S) were obtained by spraying of saturated lactose solution only.

Surface modification by roller compaction was conducted as described in Section 3.2.2.4. The powder for compaction was a blend of lactose 100M and 200M in a 1:1 ratio (w/w). The powder blend was compacted at 2 different roll forces (16.7 and 23.3 kN/cm). After 24 hours, the ribbons were comminuted in a pin mill (ZM 200, Retsch, Germany) with a 12-pin wheel against a sieve with aperture size of 0.5 µm at impactor wheel speed of 10000 rpm. Lactose carrier particles produced at roll forces of 16.7 kN/cm and 23.3 kN/cm were denoted as RC_{50} and RC_{70}, respectively.

Commercially-available inhalation grade lactose carrier (INH), lactose 100M (control) as well as the surface-modified coarse carriers (FB_S, FB_R, RC_{50} and RC_{70}) were fractionated in the air-jet sieve using the procedure described in Section 3.2.1.4. The size range of all carrier particles obtained in this part of the study was 63 – 125 µm. The typical specific surface area of INH was reported to be 0.16 m^2/g by the manufacturer.

3.3.1.3 Physical characterization of lactose carriers

3.3.1.3.1 Particle size

Coarse carrier particles were sprinkled on a glass slide and viewed under a microscope (BX51, Olympus, Japan), connected to a video camera, at 100x magnification. Images of the particles were taken and analyzed using image analysis software (Image Pro Plus 6.3, Media Cybernetics, USA). A sufficient number of images was taken such that at least 600 individual particles from each carrier batch were measured. The diameter of each particle was determined as the average length of the diameters, measured at 2° intervals, joining two outline points and passing through the centroid of the particle. Light microscopy was used for sizing, instead of laser diffraction, as it is better able to detect small differences in particle size due to differences in shape.

3.3.1.3.2 Aspect ratio

Image capture and analysis was conducted as described in Section 3.3.1.3.1. The aspect ratio of each particle was determined as the ratio between the longest and shortest diameters of an ellipse with equivalent area, respectively. The aspect ratio of a particle indicates the degree of elongation of its shape and the values are always greater than 1.

3.3.1.3.3 Convexity

Image capture and analysis was conducted as described in Section 3.3.1.3.1. Convexity was determined as the ratio between the convex perimeter and the actual perimeter of the particle. The actual perimeter follows the exact contours of the particle outline while the convex perimeter can be thought of as the perimeter of an elastic band surrounding the particle (Figure 11). Convexity indicates the degree of irregularity of the boundary of the particle. Particles with smooth outlines will have convexity close to 1 whereas those with irregular outlines will have lower convexity values.

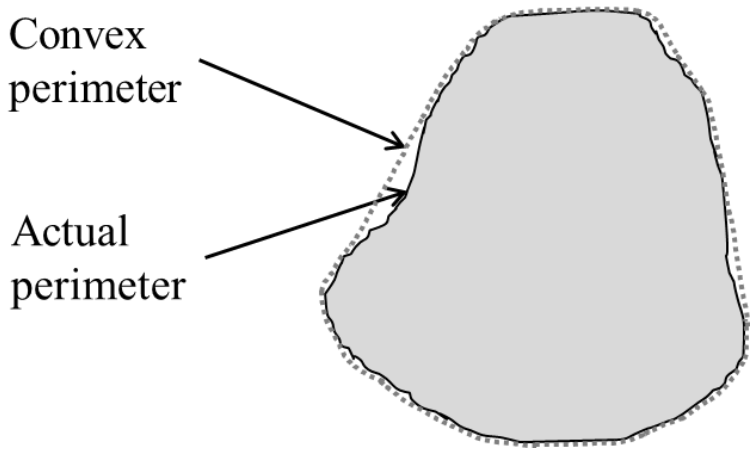

Figure 11. Diagram showing how the actual and convex perimeters of a particle are determined during image analysis.

3.3.1.3.4 Surface roughness

Surface roughness measurements were conducted as described in Section 3.2.1.5.2.

3.3.1.4 *In vitro* drug deposition studies

DPI formulations, prepared with the six types of coarse carriers respectively, comprised (a) various concentrations of fine lactose (0, 0.5, 1, 2, 3, 4.5, 6, 8 and 10 %, w/w) with micronized drug (2 %, w/w) and (b) various concentrations of drug (0.5, 1, 2, 4 and 6 %, w/w) with coarse carriers alone. Fine lactose (d_{50} = 9 µm) was produced by jet milling lactose 100M particles at a grinding air pressure of 4 bars and classifying wheel speed set at 5000 rpm. Isoniazid (Taizhou Tianrui Pharmaceutical, China) was used as the model drug in all DPI formulations and was produced by jet milling the coarser drug particles at a grinding air pressure of 4 bars and classifying wheel speed set at 14500 rpm.

Appropriate quantities of the drug, coarse carrier and fine lactose (where applicable) amounting to a total mass of 1.5 g were carefully weighed out in a glass tube and blended in a vortex mixer (WhirliMixer™, Fisons Scientific, UK) for 10 min. The drug contents in ten random samples of 30 mg were assayed and the coefficients of variation were found to be less than 6 %. Each capsule (Size 3, Qualicaps, Japan), equivalent to one dosage unit, was filled with 30 ± 2 mg of the DPI formulation.

Each collecting stage of the NGI (Copley Scientific Limited, UK) was first coated with a thin layer of 1 %, w/w silicone oil in cyclohexane and allowed to dry completely. The collecting stages, pre-separator, induction port and mouthpiece adaptor were assembled (Figure 12A). The pre-separator was used in all *in vitro* experiments in order to prevent the entry and deposition of the coarse lactose carrier particles in the NGI, particularly on Stage 1. After a capsule was loaded into the Rotahaler® (Glaxo, UK), the inhaler was

twisted to break the capsule and the contents released into the mouthpiece adaptor fitted with the NGI. The liberated particles were drawn through the NGI at an airflow rate of 100 L/min for 2.4 s in each test. The total volume of air drawn through the NGI in each test was 4 L, equivalent to the typical volume of air inhaled by an adult in one breath. The test was repeated for six capsules and the total amount of drug deposited in each part assayed.

3.3.1.4.1 Fine particle fraction

The drug deposited in the inhaler, mouthpiece adaptor, induction port, pre-separator, and stages 1 to 8 of the NGI (Figure 12B) were collected by rinsing each of the parts with a suitable volume of deionised water. The UV absorbance at 262 nm of each rinse fraction was determined by a UV spectrophotometer (3101PC, Shimadzu, Japan) and used to calculate the mass of deposited drug. In the NGI, the drug particles were deposited on the 8 collecting stages according to their aerodynamic particle size. Based on the airflow rate of 100 L/min, the cut-off aerodynamic diameters for the pre-separator and stages 1 to 7 were calculated to be 10, 6.12, 3.42, 2.18, 1.31, 0.72, 0.40 and 0.24 μm, respectively. Stage 8 is also known as the micro-orifice collector (MOC). The FPF and fraction of drug trapped in the pre-separator (F_p) were determined by:

$$\text{FPF} = \frac{M_f}{\sum \text{A}} \times 100\ \% \tag{5}$$

$$\text{F}_\text{p} = \frac{M_p}{\sum \text{A}} \tag{6}$$

where $\sum \text{A}$ is the total amount of drug deposited in the mouthpiece adaptor, induction port, pre-separator and stages 1 - 8, M_f is the amount of drug deposited in stages 2 – 4 and M_p is the amount of drug deposited in the pre-separator.

(A)

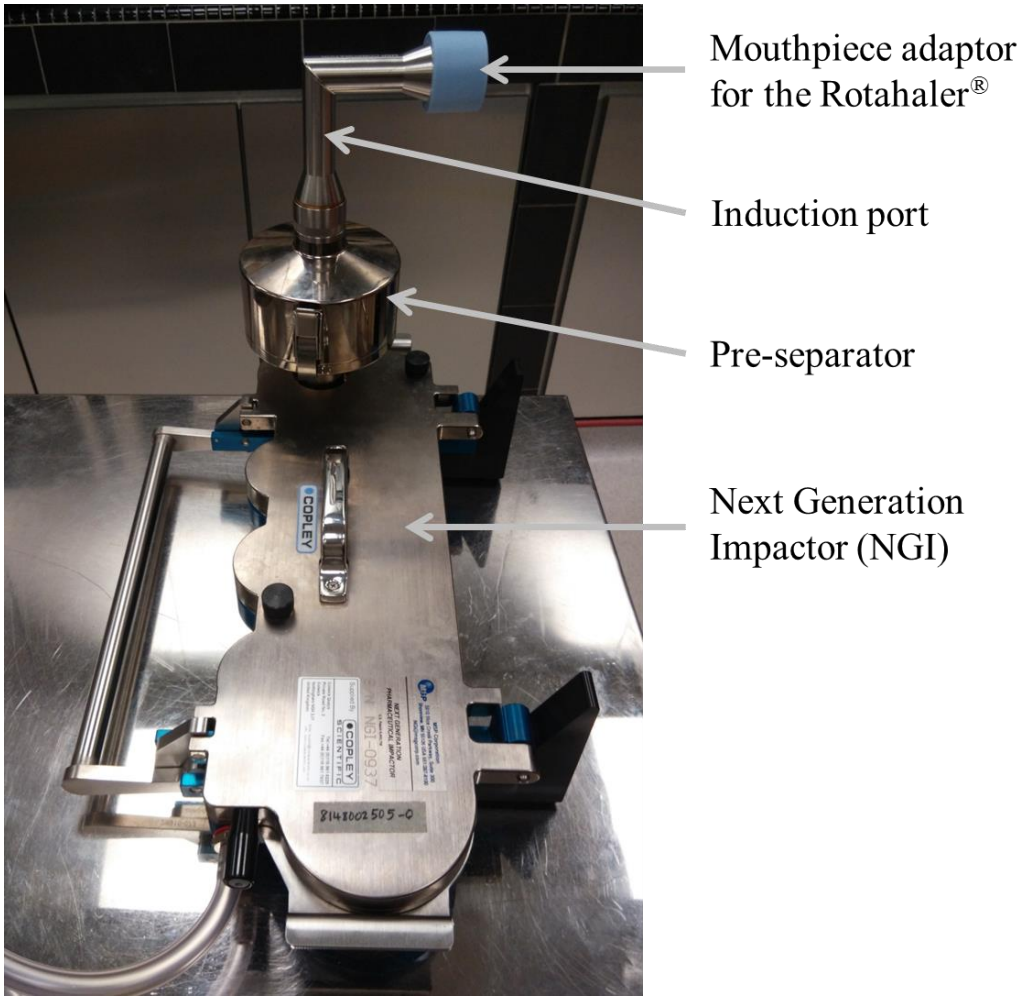

(B)

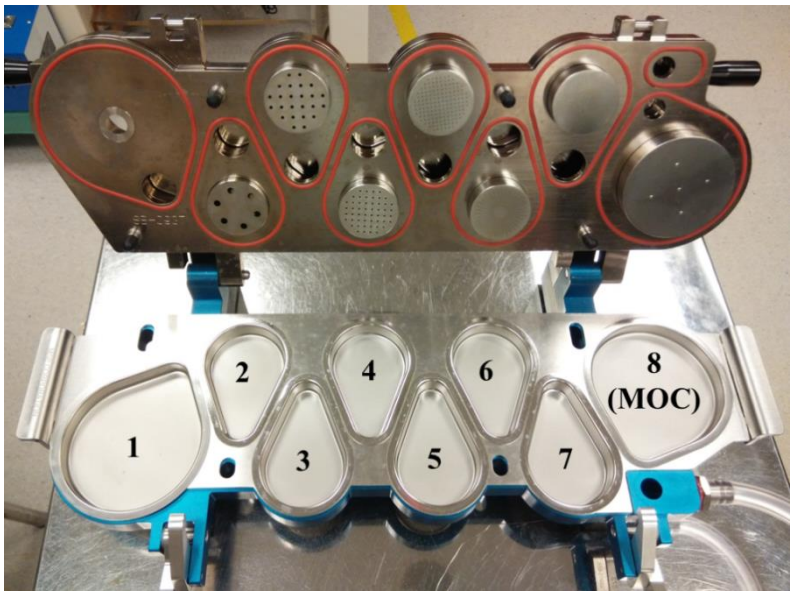

Figure 12. Photographs with labels showing (A) the complete assembly of the NGI, pre-separator, induction port and mouthpiece adaptor for the Rotahaler® and (B) stages 1 to 8 in the NGI.

3.3.1.4.2 Aerodynamic particle size

The mass median aerodynamic diameters (MMAD) of the deposited drug particles were estimated by fitting the actual size distributions, using the method of least squares, to the log-normal distribution (MATLAB®, R2010a, MathWorks, USA). Although there is no theoretical justification for its use, many inhaled pharmaceutical aerosols have been found to be well approximated by the log-normal distribution (122-124). The log-normal function is given by Eqn. (7) and satisfies the condition in Eqn. (8):

$$\mathrm{m(x)} = \frac{1}{\mathrm{x}\cdot\sqrt{2\pi}\cdot\ln\sigma_g}\cdot \mathrm{e}^{\left(\frac{-(\ln \mathrm{x}-\ln \mathrm{d})^2}{2(\ln\sigma_g)^2}\right)} \tag{7}$$

$$\int_0^{\mathrm{d}} \mathrm{m(x)dx} = 0.5 \tag{8}$$

where x is the particle size (µm), d is the MMAD (µm) and σ_g is the GSD (dimensionless). The size distributions were constructed by using the mass fraction of drug within each aerodynamic size range determined from all stages in the NGI in the *in vitro* deposition studies. Each point on the size distribution curve was calculated by taking the mass fraction of drug divided by the size interval and this was then plotted against the midpoint of the size interval.

For size distributions which did not fit well to the log-normal distribution (i.e., goodness of fit $R^2 < 0.85$), the MMAD values were estimated using the cumulative drug deposition data according to the method stipulated in the USP 30 <601>. The second approach was found to be necessary only for formulations containing very low proportions of drug (i.e., 0.5 and 1.0 %, w/w).

3.3.1.5 Geometric particle size of drug

Micronized isoniazid particles were viewed under the SEM using an accelerating voltage of 1.2 kV. A sufficient number of images was taken such that at least 600 individual drug particles were measured. The diameter of each particle was defined as the longest distance between two vertical parallel tangents on the particle. The size distribution of the drug particles was constructed using the fraction of particles (by count) in each size range. The median geometric particle size and GSD were determined by fitting the size distribution to the log-normal distribution as described in Section 3.3.1.4.2.

3.3.1.6 Powder flow characterization using the shear cell

Powder flowability was determined using the 1 mL shear cell module of the FT4 powder rheometer as described in Section 3.2.2.3.4. Five DPI formulations, with 2 %, w/w micronized drug and concentrations of fine lactose ranging from 0 – 10 %, w/w, were prepared for each of the six types of carriers. The powder blends were similarly prepared as for the *in vitro* studies. The yield locus (Figure 13) was constructed from the plot of shear stress against normal stress and the flow function, ff_c, was calculated as follows:

$$ff_c = \frac{\sigma_1}{\sigma_2} \quad (9)$$

where σ_1 is the major principal stress (kPa) and σ_2 is the unconfined yield strength (kPa). The methods for determination of σ_1 and σ_2 are in accordance to widely-used shear testing analysis procedures (125). σ_1 and σ_2 were obtained from the construction of the small and large Mohr circles, which represent the combinations of shear and normal stresses under which the powder would fail. The small Mohr circle is a semi-circle whose circumference passes through the origin and is tangential to the yield locus. The large Mohr circle is a semi-circle whose circumference passes through the pre-shear data

point (at normal stress = 9 kPa) and is tangential to the yield locus. σ_1 is the greater of the two values at which the large Mohr circle intercepts the x-axis while σ_2 is the greater of the two values at which the small Mohr circle intercepts the x-axis. Powders with ff_c between 2 and 4 are considered cohesive powders while those with ff_c between 4 and 10 are free-flowing powders (126, 127).

3.3.1.7 Statistical analyses

One-way ANOVA and regression analyses were carried out using XLSTAT (Addinsoft, USA). The purpose of the one-way ANOVA was to identify statistical differences in carrier physical properties (particle size, aspect ratio, convexity, R_a) among the 6 carrier batches. Contour plots were constructed in MATLAB® using linear interpolation between the original data points.

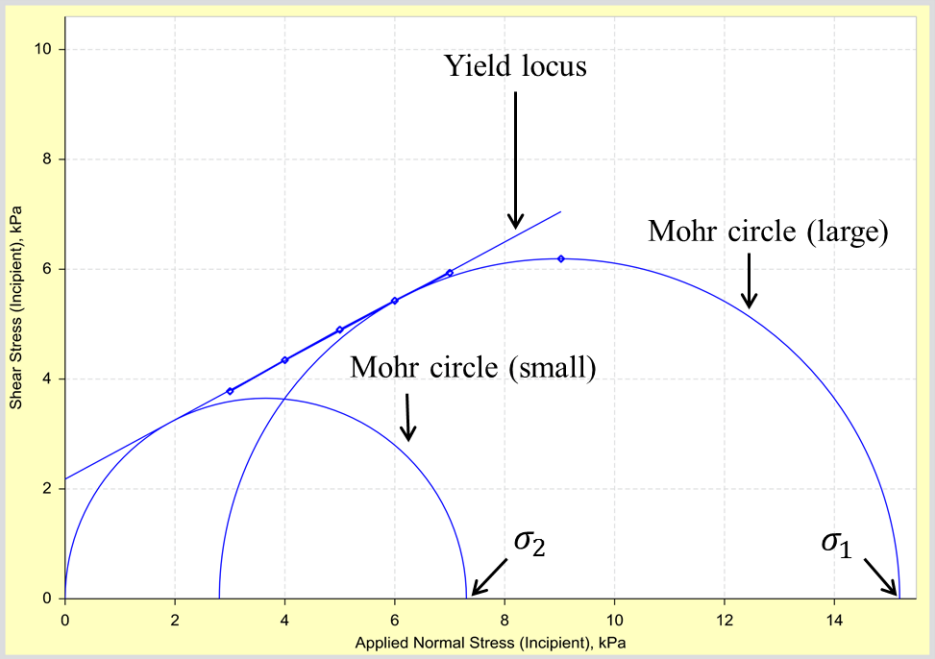

Figure 13. A typical plot of the shear stress against the normal stress after shear testing of powder samples. The yield locus and the large and small Mohr circles are indicated.

3.3.2 Part 3B: Investigation of the surface distribution of micronized drug particles on rough lactose carriers using Raman spectroscopy

3.3.2.1 Rationale of study

In the previous part of the study, the use of rough roller compacted carriers was found to increase the FPF of DPI formulations and the MMAD of deposited drug significantly compared to the smoother control and fluid-bed coated carriers. Rougher carrier surfaces may exert their effects during interactive mixing or during the aerosolization of drug and increase the FPF by the following mechanisms: (a) weaker adhesion of drug to carrier results in lower energies required for drug detachment or dispersion of drug agglomerates or (b) surface asperities on rough carriers increase frictional forces during blending and promote the physical deaggregation of cohesive agglomerates. The first mechanism has been widely discussed in literature with supporting evidence. However, the second mechanism has been relatively less studied due to experimental difficulties in determining the agglomerate distribution on carrier particles.

Raman spectroscopy can be used for the chemical identification of compounds within very small areas of interest. The analysis requires minimal sample preparation and does not disrupt the organization of particles in the interactive mixtures. It may be used to provide chemical information to differentiate between the carrier material and drug, a capability lacking in other common imaging methods (such as light microscopy or scanning electron microscopy). Hence, this study aimed to investigate the feasibility of Raman spectral mapping as a tool to assess the spatial distribution of drug particles/agglomerates on carrier surfaces.

3.3.2.2 Screening of drug markers for Raman spectral analysis

There were 3 main criteria adopted for the preliminary selection of drugs for Raman spectral analysis: (a) the drug is used clinically for treatment of either local or systemic diseases, (b) the drug is delivered through the pulmonary or oral route, and (c) for drug delivered through the oral route only, there should be reported scientific interest in developing inhalable formulations of the drug. The drugs which were identified for preliminary screening were salbutamol sulphate (Fine Drugs and Chemicals, India), budesonide (Jayco Chemicals, India), theophylline hydrate (Janson Chemicals Pte. Ltd., Singapore), rifampicin and isoniazid (Taizhou Tianrui Pharmaceutical, China). Of these drugs, salbutamol sulphate and budesonide are delivered through the inhalation route for the treatment of asthma. Theophylline is largely delivered through the oral route in the form of tablets or syrups for asthma treatment while rifampicin and isoniazid are mainly formulated as oral tablets for the treatment of tuberculosis. The purpose of screening was to select a suitable drug marker for use in the interactive mixtures with lactose carriers. Ideally, the Raman spectrum of the drug marker should contain features that can be clearly distinguished from that of lactose, such as the presence of intense peaks at Raman shifts where the scattering intensity of lactose is very weak.

The Raman spectra of all drugs, together with lactose, were collected using a Raman spectrometer (XploRA, Horiba Scientific, France) equipped with a 532 nm He/Ne laser source and connected to a microscope system (BX41, Olympus, Japan). The software for spectral acquisition was LabSpec (Version 5, Horiba Scientific, France). The powder particles of each pure component were sprinkled on a glass slide and the Raman spectra was obtained through a 10x objective (numerical aperture = 0.25) at an exposure time of 2 s. The diffraction grating was set at 1200 mm^{-1}. The theoretical laser spot diameter was calculated as follows:

$$\text{Laser spot diameter } (\mu m) = \frac{1.22 \times \lambda_{\text{excitation source}}\ (\mu m)}{\text{numerical aperture of objective}}$$

$$= \frac{1.22 \times \frac{532}{1000}}{0.25}$$

$$= 2.59$$

The spectra of all drugs were obtained within the range of 200 – 4000 cm^{-1}. Isoniazid was eventually selected as the drug for Raman spectral mapping as it showed high scattering intensities and had a distinct non-overlapping peak at the Raman shift of 1604 cm^{-1}. The presence of the peak at 1604 cm^{-1} was used to identify the presence of isoniazid particle(s) on the lactose carrier particles.

3.3.2.3 Preparation of interactive mixtures of drug and lactose

Appropriate quantities of the drug, coarse lactose carrier and fine lactose (where applicable) amounting to a total weight of 1.5 g were carefully weighed out in a glass tube and blended in a vortex mixer (WhirliMixer™, Fisons Scientific, UK) for 10 min.

3.3.2.4 Development of method to identify the presence of drug in Raman spectra

3.3.2.4.1 Determination of concentration ratio of drug to lactose

Powder samples were first poured into a well on an aluminum sample holder and gently leveled to ensure that the mapping surfaces were relatively flat. Individual particles were randomly located on the surface of the sample and the Raman spectra were obtained over a square area with defined length (Figure 14). One spectrum was obtained at each position indicated by a black dot on the figure. The total number of spectra within each Raman map was dependent on the sampling step size and the scan length. Baseline correction was applied to the Raman spectrum from every scan point in the map.

Baseline correction was applied by subtracting a polynomial obtained by fitting of each individual spectrum in the software.

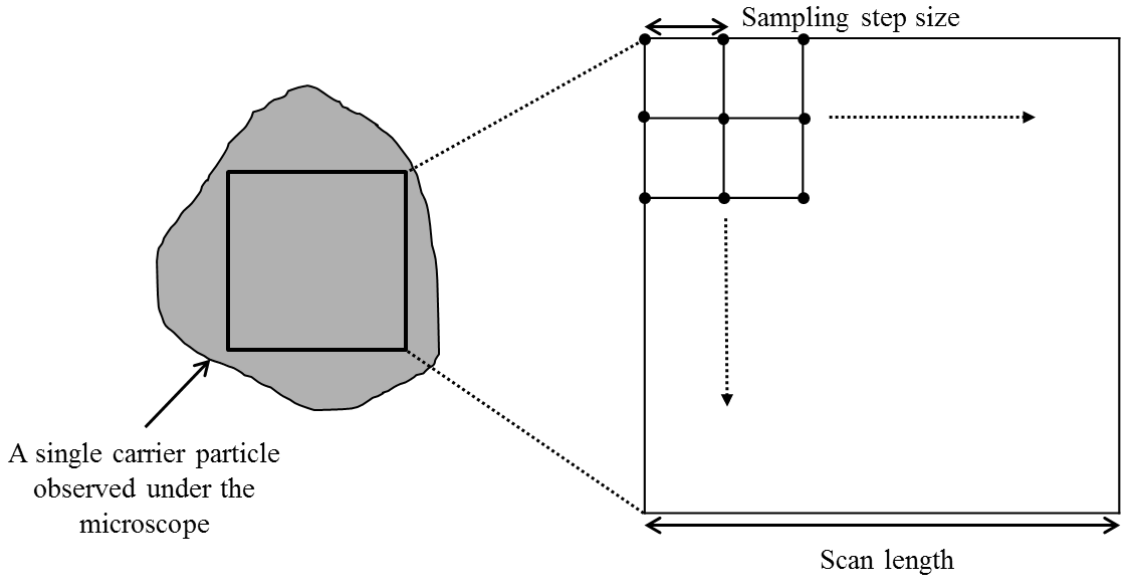

Figure 14. Diagram showing a typical carrier particle and how the Raman spectra are obtained within a square-shaped area of the particle surface.

A peak at the Raman shift of 1080 cm^{-1} in the lactose spectrum was identified as it did not overlap with any peaks in the isoniazid spectrum. The relative intensity of the Raman peaks corresponding to presence of isoniazid (at 1604 cm^{-1}) and lactose (at 1080 cm^{-1}) was calculated by:

$$\text{Peak}_{1080/1604} = \frac{\text{Peak intensity at 1080 cm}^{-1}}{\text{Peak intensity at 1604 cm}^{-1}} \quad (10)$$

The highest intensity values at the Raman shift of 1604 ± 2 cm^{-1} and 1080 ± 2 cm^{-1} were first determined in each spectrum prior to the calculation of the peak ratio. The

allowance of ± 2 cm^{-1} was to account for small shifts in the peak position due to variation in the instrument detector.

A total of 2000 point scans each were first conducted on raw lactose and isoniazid powders and the peak ratios were calculated. The range of ratio values for lactose was 5.9 – 28.5 while that of isoniazid was 0.022 – 0.083. When only lactose was present, the signal intensity at the Raman shift of 1080 cm^{-1} was high while the intensity at 1604 cm^{-1} was low as it formed part of the background noise. None of the ratio values fell below 5.9 when only lactose was present in the sample. Conversely, the signal intensity at 1080 cm^{-1} was part of the background noise while the intensity at 1604 cm^{-1} was high in the isoniazid sample. None of the ratio values were greater than 0.083 when only isoniazid was present in the sample. The ratios calculated from each type of compound (either lactose or isoniazid) varied significantly as they were calculated from the background signals which were affected by variations in small measurement distances and surface curvatures or distortions. From these preliminary scans, the following inferences could be reliably drawn:

(a) Only isoniazid is present in the scan spot when the ratio is smaller than 0.083

(b) Only lactose is present in the scan spot when the ratio is greater than 5.9

(c) Both lactose and isoniazid are present when the ratio is between 0.083 – 5.9

3.3.2.4.2 Calculation of spectral scores

After the $Peak_{1080/1604}$ ratios were obtained, they were further used to derive the spectral scores (SS) for the Raman chemical images. The SS ranged from 0 – 1, where 0 was taken to represent the absence of isoniazid while 1 was taken to represent the presence of isoniazid only. The SS represented the normalized concentration ratio of

isoniazid to lactose at each scan spot. A continuous scoring system was necessary as it has been reported that the Raman spectra obtained from a mixture of components rarely yield the spectra of pure components on individual scan spots. Composite spectra, which are equal to the weighted sum of the Raman spectra of the components present in the sample collection volume, are usually obtained instead (128). For interactive mixtures comprising a low concentration of micronized drug particles (i.e., lower than 5 %, w/w) in coarse lactose particles, literature suggests that the micronized particles are sparsely located as agglomerates on the carrier surfaces. Therefore, considering that the laser spot size was 2.6 μm, majority of the spectra would be expected to be from lactose alone, some would be composite spectra of isoniazid and lactose and an even smaller proportion would be the spectra of drug alone.

The SS was determined as follows:

If $\text{Peak}_{\frac{1080}{1604}} < 0.083$, $\quad SS = 1$

If $\text{Peak}_{\frac{1080}{1604}}$ is between 0.083 – 5.9, $\quad SS = 1 - \frac{\text{Peak}_{1080/1604} - 0.083}{5.9 - 0.083}$

If $\text{Peak}_{\frac{1080}{1604}} > 5.9$, $\quad SS = 0$

The SS represents only a rough approximation of the concentration ratio of isoniazid in lactose in the sampling volume (129) as Raman intensities are generally too noisy for precise quantitative applications. Using the SS, Raman maps containing visual information were constructed in grayscale to indicate the relative amounts of isoniazid present on the carrier surface. The Raman maps were constructed using MATLAB®. The distributions of the SS values were also investigated in histogram plots.

3.3.2.5 Sampling strategies for construction of chemical images

Due to the small laser spot size, relative to the total surface area under analysis, the sampling step size and scan area determine how the information obtained from the Raman spectra can be utilized. Two different scan lengths were investigated: 400 and 100 µm. Considering that the carrier particles were ~ 100 µm, the purpose of using a scan length of 400 µm was to obtain information over larger length scales (i.e., many particles) in the samples. On the other hand, the scan length of 100 µm was used in order to maximize the information that can be obtained from single particle surfaces. Prior to each scan, the position of the particle was adjusted using the stage controls of the microscope to ensure that the scan area fell within the entire surface boundary of the particle. Scans were conducted using two sampling step sizes: 5 and 20 µm.

CHAPTER 4

RESULTS AND DISCUSSION

4 RESULTS AND DISCUSSION

4.1 Part 1: Investigation of the measurement criteria and image processing techniques for reliable attributes to quantify surface roughness of particulates by optical profilometry

4.1.1 Qualitative assessment of the surface morphology of carrier particles

The changes to the surface morphology of particles were qualitatively assessed using the SEM. The carrier morphology, namely their shape and size, did not differ between the two carrier batches. The carrier particles generally had tomahawk shape with flat and distinct surfaces that were characteristic of α-lactose monohydrate crystals. Spraying of micronized lactose dispersion during surface modification had resulted in extensive surface coverage of micronized lactose on the lactose carrier particles (Figure 15). The micronized particles were preferentially deposited in and around large-scale surface features and, to a limited extent, on the flat crystal faces. The lactose particles from both batches were visually distinguishable under the SEM as the smoothened particles had an obvious lack of adhering surface fines.

4.1.2 Surface roughness measurements using the optical profiler

4.1.2.1 Preliminary assessments of raw surface profiles

The following general observations were noted when lactose particle surfaces were initially profiled:

1) Although the scan area measured was 109 x 144 μm, actual particle surfaces that were successfully captured in each scan were always occupying smaller areas. Hence, the real captured area was the composite of areas from different particles.
2) Particle surfaces were almost always tilted with respect to the horizontal plane of measurement.

3) Tilted surfaces which exceeded a certain angle of tilt could not be captured completely.
4) Surface images were rarely of very good quality and often presented with black dots/regions on the image, indicating the loss of data at some pixels.
5) Flat and smooth surfaces resulted in the best quality images while poor quality images were more frequent with rough and tilted surfaces.
6) Particles from the same sample might have surfaces that ranged from being very smooth to very rough.

Although such issues existed for particulate samples and could impact on roughness measurement, they are not well acknowledged or discussed in literature reports.

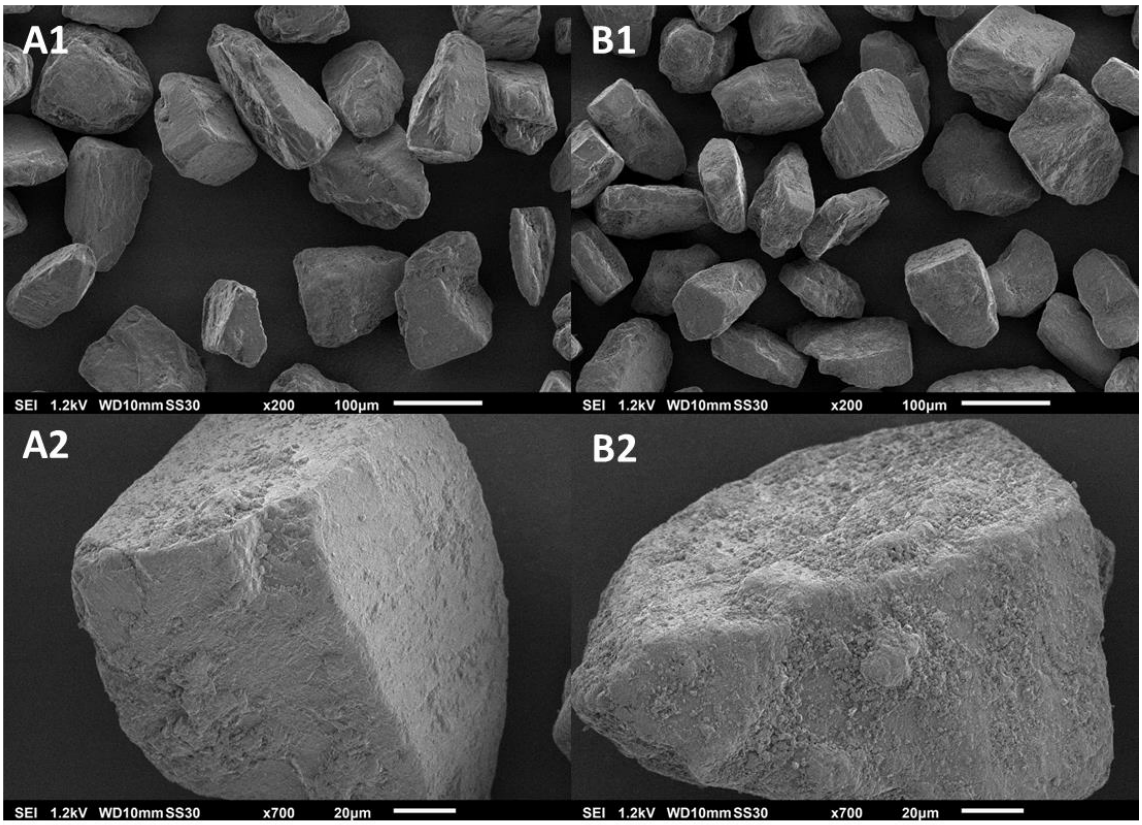

Figure 15. Scanning electron micrographs of (A) smoothened and (B) roughened carrier particles, showing their (1) general particle morphologies and (2) typical surface appearances.

4.1.2.2 Analysis of surface profiles using power spectral density plots

The PSD plots of 10 randomly selected surface images from the smoothened and roughened batches of carrier particles are shown in Figure 16. They provided information on the magnitude of surface heights across varying length scales on each surface. This type of analysis can be applied to any physical signal that can be decomposed into their constituent frequencies, such as a surface profile. The frequencies obtained from surface profiles are expressed in 1/μm, analogous to frequencies on the time scale which are expressed in terms of Hertz (Hz; 1/s). The PSD plot was useful for identifying the overall surface profile because for any given surface, features within a spectrum of length scales can exist, ranging from the micron-sized surface protrusions to the nano-scale surface asperities.

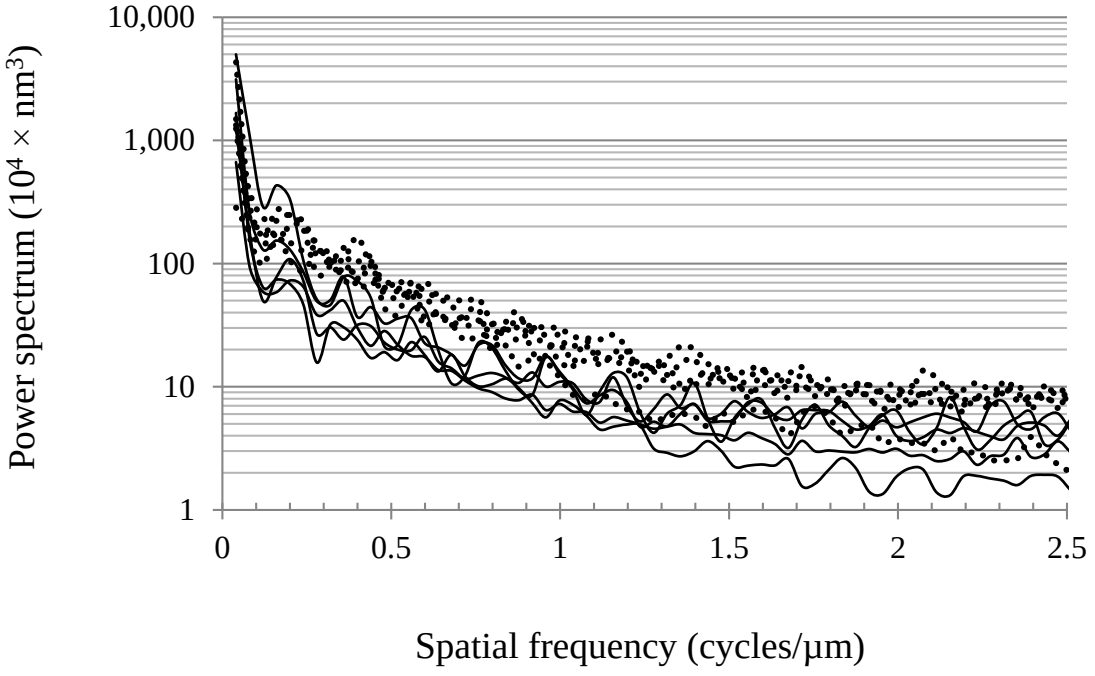

Figure 16. Power spectral density plots of 10 randomly selected surface images, of which 5 images each were taken from the respective batches of roughened (dotted lines) and smoothened (solid lines) carrier particles.

In general, all PSD profiles exhibited a decreasing trend with increasing spatial frequency. This is typical of natural and randomly rough surfaces (130) and indicates that the surface asperities tend to become shorter when they are observed over smaller length scales (i.e., surface components of higher spatial frequency). The most significant decrease in the PSD profile occurred between the frequencies of 0 – 0.1 μm^{-1}, followed by a decrease according to the power law up to 1.5 μm^{-1} (i.e., linear decrease). At frequencies greater than 1.5 μm^{-1}, the graph reached a plateau. As the power spectrum is calculated from the magnitude of surface heights, the initial sharp decrease seen in the graph suggests that surface features of lower spatial frequencies (0 – 0.1 μm^{-1}, corresponding to wavelengths greater than 10 µm) were of the greatest heights. Considering that the image sizes were 20 × 20 µm, these spatial frequencies were understood to constitute the shape of the surface (i.e., tilt or curvature with reference to the horizontal plane). This means that if roughness calculations were performed directly on the raw surface profiles, the order of magnitude of R_a (i.e., whether it is in the tens, hundreds or thousands of nm) will be determined by the shape of the surface. On the other hand, the relatively flat power spectrum beyond frequencies of 1.5 μm^{-1} suggests that the lateral resolution of surface features smaller than 0.66 µm (reciprocal of 1.5 μm^{-1}) in scale was approaching a limit. This observation was in agreement with the lateral resolution value (Page 48; 0.75 µm) provided by the manufacturer of the optical profiler. Hence, very limited useful surface information of this length scale could be extracted from the surface profiles. Since the PSD plots were presented in the log-scale, the absolute differences in surface heights among the roughened and smoothened particle surface images were much higher at the lower frequencies. By comparing the power spectrum of roughened and smoothened samples, it was found that on average, the graphs from the smoothened and roughened particles overlapped when the spatial

frequencies were smaller than 0.1 μm^{-1}. Beyond this length scale, the roughened and smoothened surfaces were distinguishable.

Based on the above observations, a band-pass filter with high and low cut-off spatial frequencies of 0.1 and 1.5 μm^{-1}, respectively, was selected for subsequent processing of surface profiles. The sampling dimensions ($20 \times 20\ \mu m^2$) physically limited the accurate representation of surface features of a similar or larger length scale and therefore the frequencies smaller than 0.1 μm^{-1} had to be filtered out. On the other hand, the scale of roughness associated with spatial frequencies greater than 1.5 μm^{-1} were considered too small to be applicable for this study as the size of micronized drug particles are typically larger than 1 µm. Furthermore, the extreme sensitivity of the optical profiler to environmental vibrations has been reported and roughness at smaller scales would be increasingly being impacted by random noise during the measurements.

The surface images in Figure 17 were used to illustrate the effect of different modes of digital filtering on a raw surface profile. It was also used to visually verify that the selected cut-off frequencies obtained from the PSD plots were relevant. It could be seen that the shape of the surface (Figure 17B; R_a = 2140 nm) was extracted from the unprocessed image (Figure 17A; R_a = 2800 nm) after the low-pass filter was applied. The roughness profile contributed by more closely-spaced surface undulations (Fig 17D; R_a = 169 nm) was extracted by the high-pass filter. Most of the original surface information was still largely preserved by the band-pass filter except that of the two extreme regions of spatial frequencies (i.e., smaller than 0.1 and greater than 1.5 μm^{-1}), which were suppressed in the filtered image (Figure 17C; R_a = 976 nm).

4.1.2.2.1 Effect of surface tilt on the variation of roughness values

It was observed that almost all the raw profiled surfaces exhibited a certain degree of tilt. The degree and direction of surface tilt were random but had always led to a significant increase in the R_a value. This was anticipated as lactose particles were irregular in shape and their surfaces would rarely be flat with respect to the horizontal plane of measurement. Figures 18A and 18B illustrate a surface before and after the removal of linear surface tilt and the R_a value was found to decrease significantly from 1450 to 402 nm after the linear tilt was removed. During the application of the tilt removal, however, only linear tilt can be effectively removed. This is because the raw surface is first fitted to a linear plane and the linear plane is then subtracted from the raw surface to obtain the processed surface image with tilt removed. Any other irregularly-shaped surface could not be reliably removed using this method. The band-pass filter, on the other hand, could be used to suppress irregular surface shapes. Figure 18C shows that band-pass filtering alone resulted in a relatively similar R_a value of 344 nm, suggesting that surface tilt was also successfully removed. The slightly lower R_a value could have resulted from both the removal of linear surface tilt and any irregularly-shaped surface shape, which was an additional benefit of the band-pass filter. Hence, the band-pass filter alone would be used subsequently before any R_a value was derived.

The histogram plot of the number of image pixels with different surface heights is shown in Figure 19. The majority of the highest peaks and valleys (i.e., surface heights between -3000 to -1000 nm and 1000 to 3000 nm) in the surface were retained when applying a low-pass filter, confirming that they were of the lowest spatial frequencies. The surface heights obtained after high-pass filtering were normally distributed and much smaller, suggesting a high degree of randomness. The measured values were likely to include random noise signals as would be typical for any surface profiling instrument sensitive

to environmental vibrations. Combining the analyses of the PSD plots, the histogram plot and from the visualization of derived surface images, it was concluded that the surface tilt (a part of surface shape) constituted the lower spatial frequencies and had contributed most significantly to the order of magnitude of R_a (typically between 1000 – 3000 nm). The removal of surface tilt, which had no bearing on the surface properties, was therefore necessary as it was an inevitable consequence of the surface analysis of particulates.

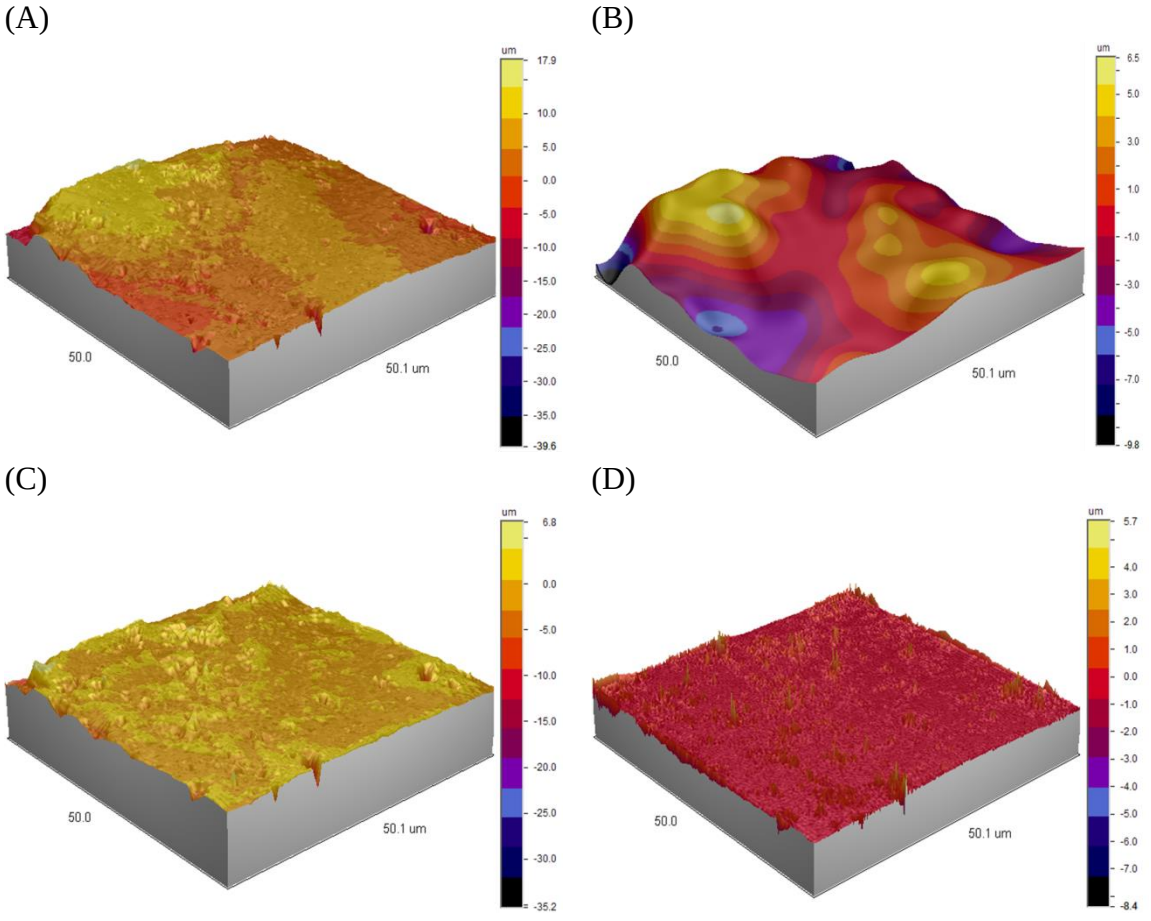

Figure 17. (A) Raw unprocessed surface image and surface profiles after (B) low-pass filtering, (C) band-pass filtering and (D) high-pass filtering. The R_a values of the extracted profiles in A – D were 2800 nm, 2140 nm, 976 nm and 169 nm, respectively. The vertical scales in the four images are not equal.

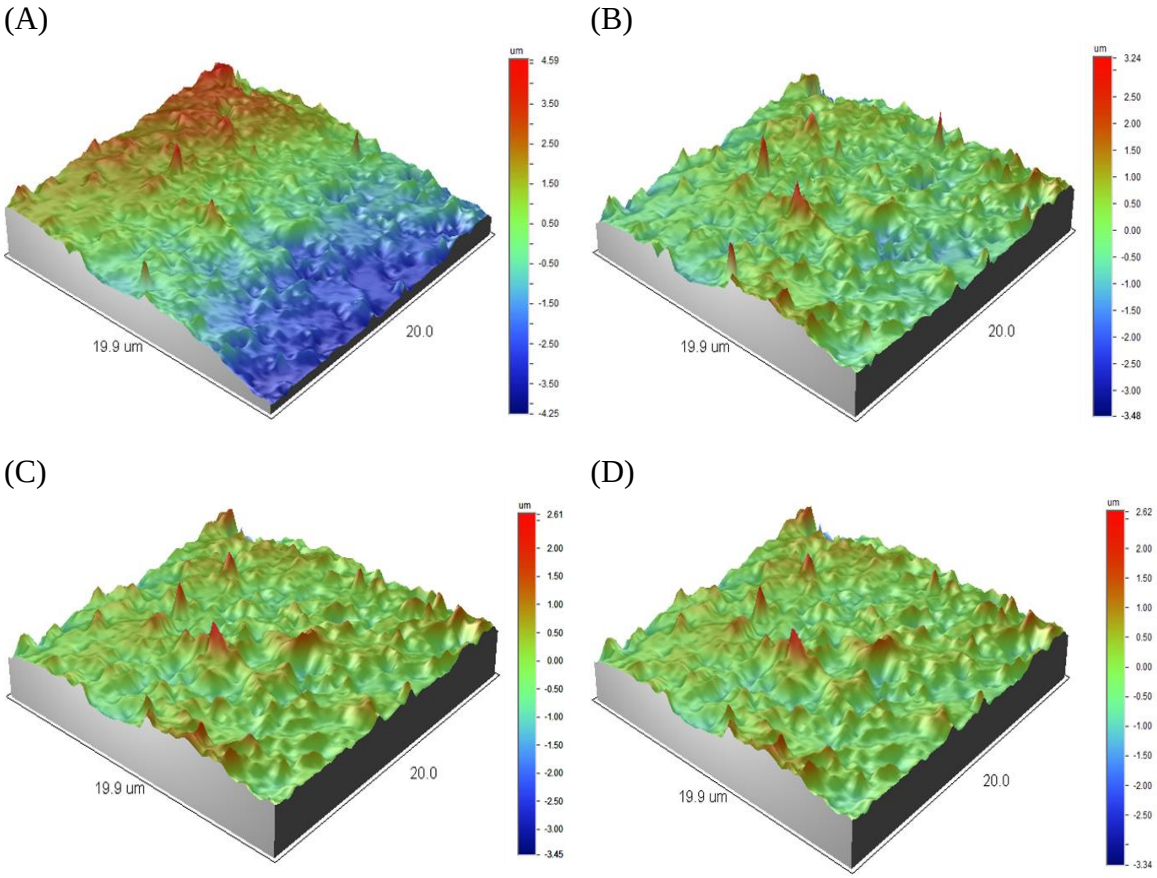

Figure 18. (A) Raw unprocessed surface image and the same surface after (B) the linear tilt was removed, (C) a band-pass filter was applied and (D) both linear tilt was removed and a band-pass filter was applied. The R_a values of surfaces in A – D were 1450 nm, 402 nm, 344 nm and 347 nm, respectively. The vertical scales in the four images are not equal.

4.1.2.2.2 Effect of sample size on the magnitude of roughness values

Unlike for the measurement of particle size, no statistically acceptable sample size for roughness measurements of particulates has been proposed in the literature. Surface profiling is not a bulk measurement method and can be highly variable and very dependent on the method of measurement and treatment of measurement data. Thus, the accuracy and statistical reliability of the measurements were deemed to be highly critical. A statistically appropriate sample size also depends on the inherent variation of roughness values in the same sample and the expected real differences in roughness

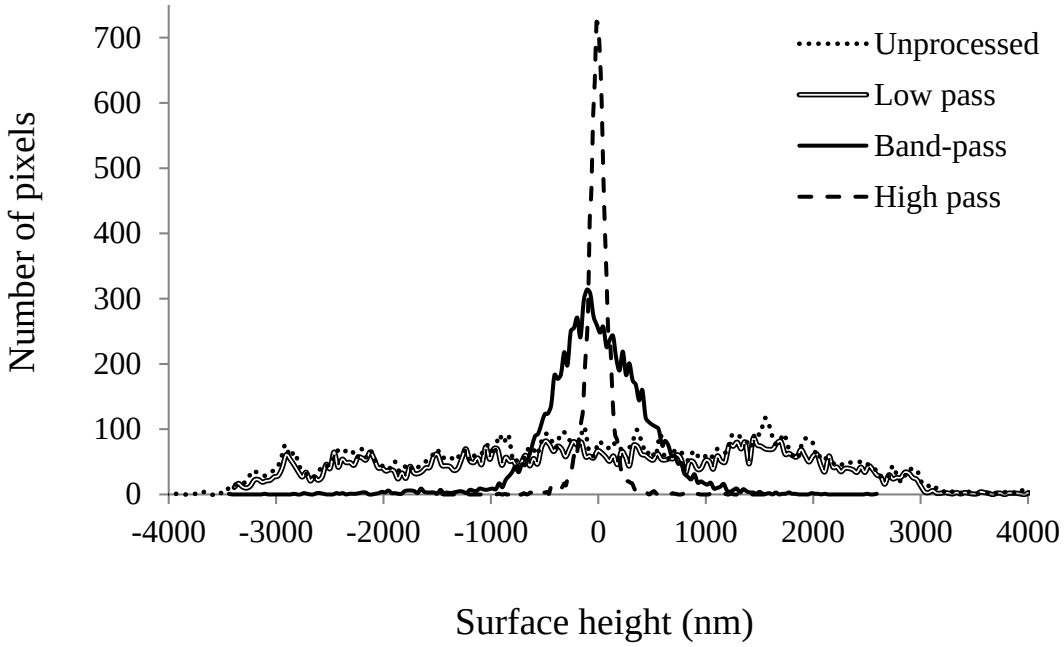

Figure 19. Histogram plot of the number of pixels with different surface heights after low-pass, band-pass and high-pass filtering.

values between different samples. If the variability in a sample was higher and the expected differences between samples were smaller, larger samples sizes would be required to demonstrate statistical differences with the same level of confidence. The variability of roughness measurements within a sample was found to be inherently high, with the coefficients of variation typically above 30 %. Figure 20 illustrates the moving averages of R_a and R_q calculated using different samples sizes (N). With N values of 20, 60 and 80, the spread of values were high and individual average values deviated by 100 – 250 nm from the mean line. The fluctuations were reduced to an approximately 50 nm range with samples sizes of 120 and above. Regardless of the N value, the moving averages had fluctuated about the same approximate mean of 420 nm. The results in Table 5 show that when N was greater than 120, the relative standard errors of both the mean R_a and R_q were less than 5 %. This was taken to be the acceptable limit for the

purposes of this thesis. The use of a larger N only ensures that the mean value would be reasonably close to the true mean but has no impact on the variability of roughness. From the results, N = 150 was selected for subsequent roughness measurements.

4.1.2.2.3 Effect of image size on the magnitude of roughness values

Table 6 shows the R_a of both the smoothened and roughened particles when they were obtained using three different image sizes. The maximum image size of 30 × 30 μm^2 was selected based on the feasibility of obtaining statistically acceptable numbers of surface images from particles within the range of 125 – 180 µm. The smaller image sizes of 20 × 20 μm^2 and 10 × 10 μm^2 were also investigated to make provisions for roughness measurements for particles within a smaller size range. When the images were unprocessed, larger image sizes always resulted in higher R_a and R_q values. It has often been suggested that higher roughness values with larger scan sizes was due to the inclusion of more prominent surface features on a larger length scales. At the same time, the surface tilt would also be more significant with larger image sizes. The effect of image size was greatly reduced by the band-pass filter. It was anticipated that particles of different sizes could be measured in subsequent work. Thus, the possibility to use different image sizes was established and suitable processing steps ensured comparable roughness values were obtained.

4.1.2.2.4 Relationship between R_a and R_q

The R_a and R_q values are amplitude parameters commonly used to express the degree of surface roughness of particulates. Due to the nature of their calculation methods, R_a and R_q values provide slightly different quantitative information about the surface. The R_a parameter is less sensitive to atypical surface features (tall surface asperities and deep valleys) as they would be averaged out in the final value. The R_q value, on the other hand,

is more sensitive to atypical surface features because the surface height values are squared in its calculation. For this reason, the R_q values were always higher than the R_a values. The R_a and R_q values occur as pairs as they are simultaneously calculated from each surface image. In order to investigate if the R_q would provide any additional information about the surface, the R_a and R_q values for all surface images were plotted against each other in Figure 21. They were found to be linearly related (R^2 = 0.99). Hence, only the R_a value would be needed and used to represent the surface roughness of lactose carrier particles in subsequent studies.

Table 5. Statistical parameters calculated from the moving averages obtained using different values of N

Sample size (N)	No. of elements*	Roughness parameter			
		R_a (nm)		R_q (nm)	
		Average	RSE (%)	Average	RSE (%)
20	381	416.9	12.7	723.7	13.9
60	341	418.3	5.1	711.5	7.5
80	321	418.7	4.2	707.7	5.3
120	281	416.7	3.1	705.6	2.9
150	251	416.2	2.6	704.2	2.8
200	201	416.0	1.6	702.7	2.2
250	151	416.2	0.9	704.2	1.4

*Number of elements in the moving average, calculated from 400 individual values
RSE refers to the relative standard error

(A)

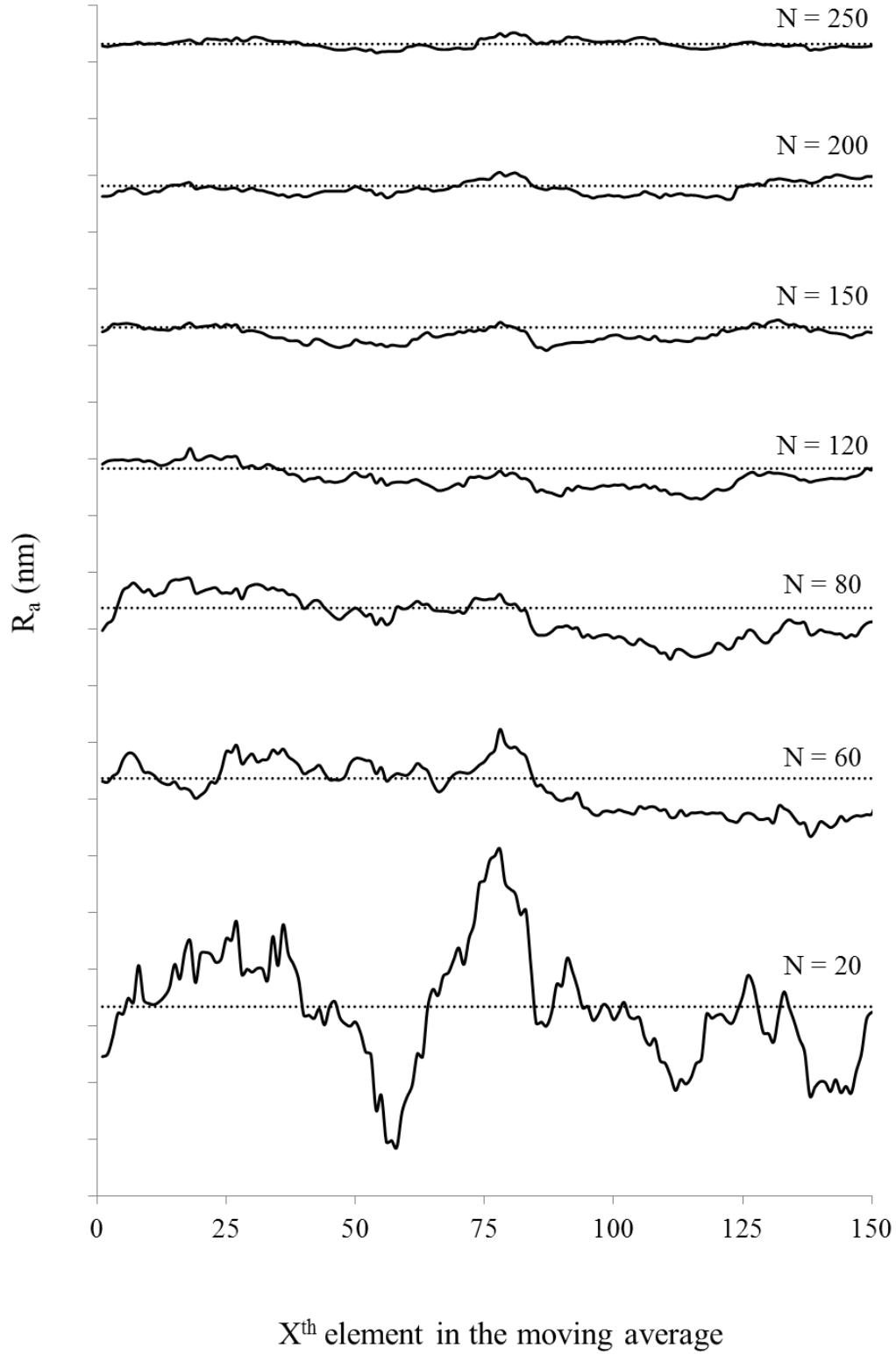
N = 250
N = 200
N = 150
N = 120
N = 80
N = 60
N = 20
R_a (nm)
0
25
50
75
100
125
150
X^{th} element in the moving average

(B)

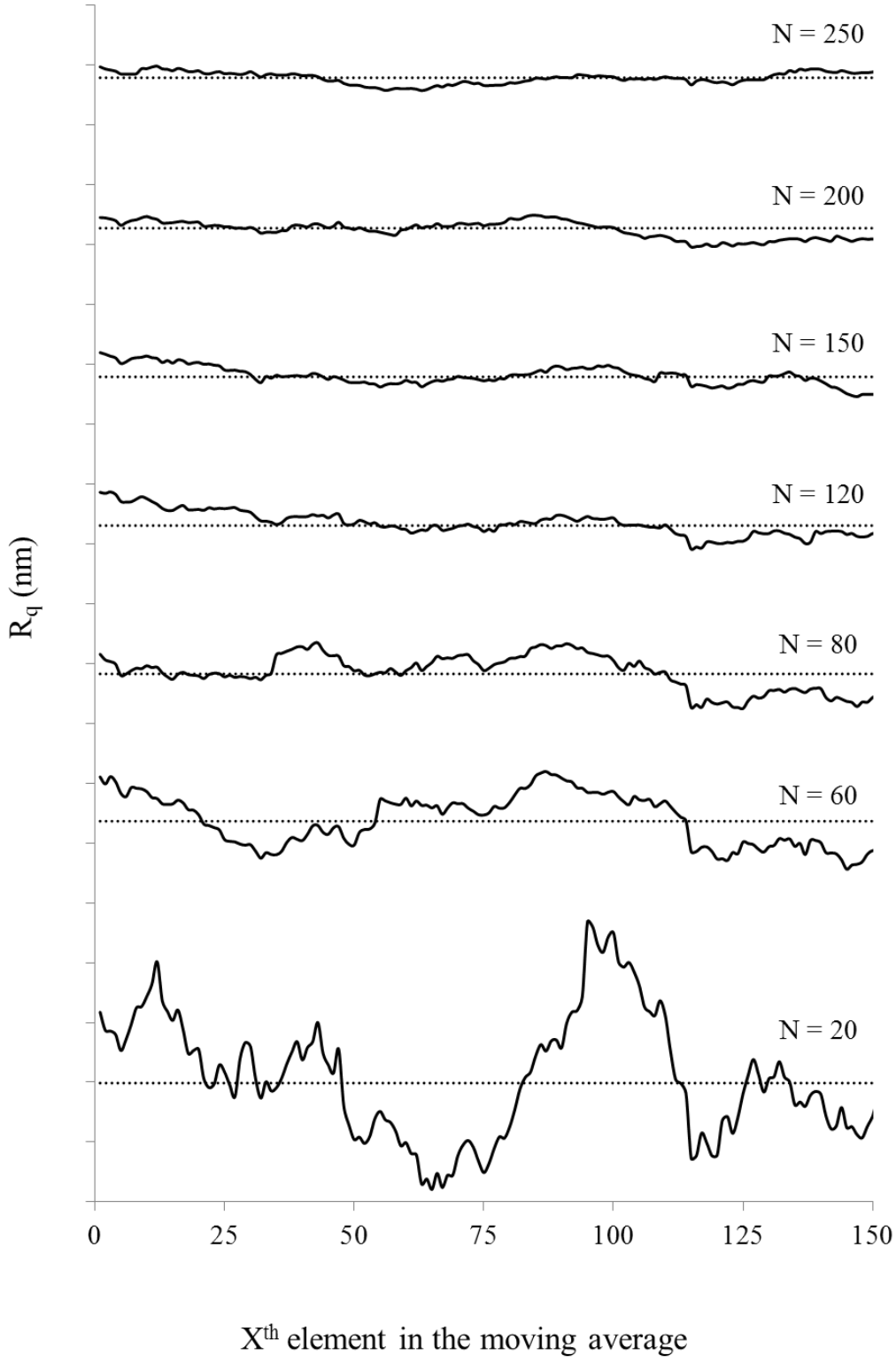

Figure 20. Moving averages of (A) R_a and (B) R_q calculated using different sample sizes for the smoothened lactose particles. The dotted lines represent the overall averages of all elements in the series for each N value used. Each division on the y-axis represents 50 nm and 100 nm in the graphs in (A) and (B), respectively.

Table 6. Roughness parameters obtained from the smoothened and roughened carrier particles when different image sizes, with and without band-pass filtering, were used

Smoothened carrier particles

Image size (μm^2)	Unprocessed		After band-pass filtering	
	R_a (nm)	R_q (nm)	R_a (nm)	R_q (nm)
30 x 30	1642 (704)	2050 (866)	484 (256)	750 (398)
20 x 20	1285 (583)	1634 (724)	437 (215)	657 (332)
10 x 10	827 (446)	1110 (573)	431 (219)	631 (360)

Roughened carrier particles

Image size (μm^2)	Unprocessed		After band-pass filtering	
	R_a (nm)	R_q (nm)	R_a (nm)	R_q (nm)
30 x 30	3303 (1850)	4020 (2186)	772 (288)	1125 (403)
20 x 20	2088 (1173)	2585 (1397)	726 (275)	1013 (376)
10 x 10	1362 (735)	1703 (862)	683 (291)	924 (375)

Values in parentheses represent the respective standard deviation

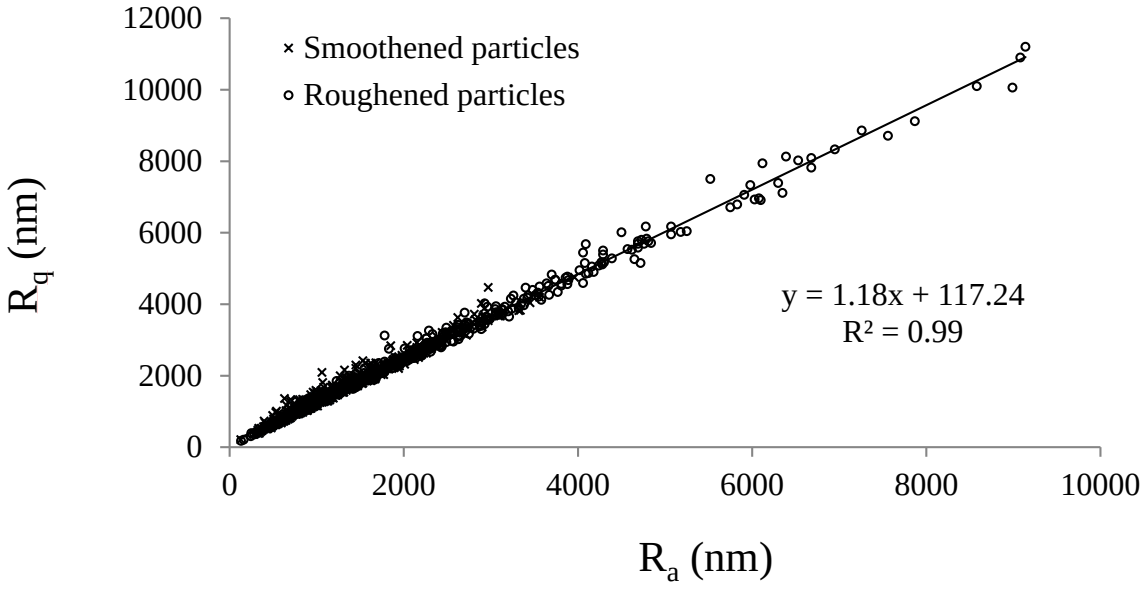

Figure 21. Relationship between R_a and R_q for all analysed surface images from both the roughened and smoothened carrier particles.

4.1.3 Summary of Part 1

Measurement and image processing criteria such as the sample size, sample tilt, scan area and type of filter applied were shown to influence the magnitude of R_a significantly. Due to the particulate nature of the samples, roughness measurements were challenging to perform as the general shape and surface tilt were highly variable among different image areas. The scale of observation was found to be the most critical factor which influenced the magnitude of R_a values. As the surfaces were profiled with increasing detail (i.e., over smaller areas), the R_a value showed a corresponding decrease. The band-pass filter was a useful tool as it had achieved the following objectives: (a) removal of any surface tilt, (b) extraction of surface components of impact, (c) elimination of inherent noise due to environmental vibrations and (d) allowed the use of different image sizes but enable the determination of comparative roughness values to be made.

The lack of useful and comparable roughness values reported by various researchers stemmed from a lack of standardization in conditions for roughness measurement as well as data pre-processing. From this study, a set of measurement conditions was defined for the determination of R_a: N = 150, band-pass filtering with cut-off spatial frequencies of 0.1 and 1.5 μm^{-1} and surface image areas in the range from 10 × 10 μm^2 to 30 × 30 μm^2. These conditions were employed in all subsequent studies. It should be noted that this set of criteria was selected for lactose particles with a size range of approximately 40 – 200 µm and is suitable for studying only this particular length scale of surface information. Where there are vast differences in the size of profiled images or the resolution of other surface profiling instruments, the criteria for image processing are likely to differ but may be investigated using a similar experimental protocol.

4.2 Part 2: Investigation of two methods to prepare roughened lactose carrier particles

4.2.1 Part 2A: Fluid-bed coating

4.2.1.1 Particle size and size distributions of lactose carriers

A total of 10 different types of lactose carriers was obtained and they were labeled according to their size range and degree of surface roughness as indicated in Figure 8 (Page 57). The size and size distribution of all lactose carriers are presented in Table 7. In general, carrier particles which were fractionated using the same sieve aperture sizes exhibited similar d_{50} even though they were obtained from powders of different particle sizes (i.e., feed P1, P2 and P3). The d_{50} values were approximately 170, 110 and 60 µm for Fractions A, B and C respectively. The span values increased as the size fraction increased. The preparation of carriers of consistent and narrow size ranges allowed for a more accurate study of the surface roughening effect on particles of different sizes during fluid-bed coating.

4.2.1.2 SEM images of lactose carrier particles

The changes to the surface morphology of the carrier particles were qualitatively assessed using SEM images. Representative SEM images of selected lactose carriers are shown in Figure 22. Attachment of the micronized lactose to the surfaces of the roughened carrier particles (Figure 8; A2, A3, B2, B4, C2, C3) was evident in all the size fractions, albeit to different extents. In all cases, the micronized particles were more heavily deposited in the large-scale irregular regions on the particle surface. It was also observed that more micronized lactose were deposited on the flat planar surfaces of roughened particles in fraction A compared to fraction B. Smoothened particles could be clearly differentiated by the lack of micronized lactose adhering to the particle surfaces.

Table 7. Size and span parameters of fluid-bed coated lactose carrier particles

Carrier code	Particle size (μm)			Span
	d_{10}	d_{50}	d_{90}	
A1	135.0 (1.8)	175.8 (1.0)	225.4 (4.1)	0.51 (0.03)
A2	130.0 (7.0)	170.9 (3.2)	217.8 (4.3)	0.51 (0.03)
A3	135.9 (0.6)	176.9 (2.1)	226.8 (5.3)	0.51 (0.02)
B1	82.3 (5.3)	122.6 (2.2)	160.0 (1.4)	0.63 (0.05)
B2	79.1 (11.3)	123.5 (3.2)	162.1 (3.4)	0.67 (0.08)
B3	72.4 (0.5)	112.0 (0.8)	152.7 (1.8)	0.72 (0.01)
B4	71.0 (0.4)	110.7 (0.3)	149.9 (2.3)	0.70 (0.02)
C1	38.6 (0.4)	63.5 (0.2)	92.7 (0.2)	0.85 (0.01)
C2	39.2 (0.4)	63.6 (0.2)	92.8 (1.1)	0.84 (0.02)
C3	41.2 (2.3)	63.3 (0.5)	92.2 (1.7)	0.81 (0.06)

Values in parentheses represent the respective standard deviation

4.2.1.3 Effect of particle size of feed powder on surface roughening effect

The sizing data for the three powders used for fluid-bed coating used are presented in Table 1 (Page 56). Feed P1 had the largest particle size (d_{50} = 154 μm) and the smallest span value (span = 0.88). Feed P2 and P3 had similar d_{50} values (48 and 47 μm). However, feed P3 had smaller span value than feed P2 because particles larger than 100 μm had mostly been removed from feed P3. The effect of powder classification could be clearly seen from the 30 μm decrease in the d_{90} values of feed P3 compared to feed P2. Due to the differences in particle size of the feed powders, the amounts of micronized lactose sprayed on the coarse particles were adjusted based on their measured specific surface areas (Table 2). This adjustment was taken to ensure that the extent of surface roughening would theoretically be similar, assuming that the efficiency of adhesion of

micronized lactose was the same for all feed powders. Collectively, the use of these 3 feed powders allowed the surface roughening effect on particles ranging from 40 – 200 μm to be studied.

The R_a values and specific surface areas for all fluid-bed coated carriers are shown in Table 8. The standard deviations of R_a were calculated from the R_a of individual surface images and were large in magnitude compared to the mean R_a. This observation suggested that there was very high intrinsic variability of R_a at the level of individual particles in a population. Nevertheless, valid comparisons can still be made using the mean R_a when a sufficiently large sample size is used. Comparing the coated carriers A1 – A3, it can be clearly seen that the increase in R_a was related to the amount of micronized lactose sprayed. Carrier A2 was of intermediate roughness (R_a = 522 nm) compared to carrier A1 (R_a = 437 nm) and carrier A3 (R_a = 726 nm). It should be recalled that the amount of micronized lactose powder sprayed on carrier A2 was one-third of that sprayed on carrier A3. Hence, the quantitative change in roughness suggests that the extent of surface roughening was dependent on the amount of micronized lactose sprayed on the coarse particles.

The extent of surface roughening for different carrier batches from different feed powders was evaluated based on the percentage increase in R_a and specific surface area in each carrier batch, relative to the smoothest carrier obtained from the same feed powder. In general, it was found that the carrier batches (A1 – B2) obtained from feed P1 showed greater increase in both the R_a values as well the specific surface areas compared to those obtained from feed P2 and P3. In particular, carrier B2 exhibited a 59 % increase in the R_a value compared to 37 % in carrier B4 even though the R_a of the corresponding smooth particles were similar. Therefore, the surface roughening effect was shown to increase when the feed powder had a larger particle size.

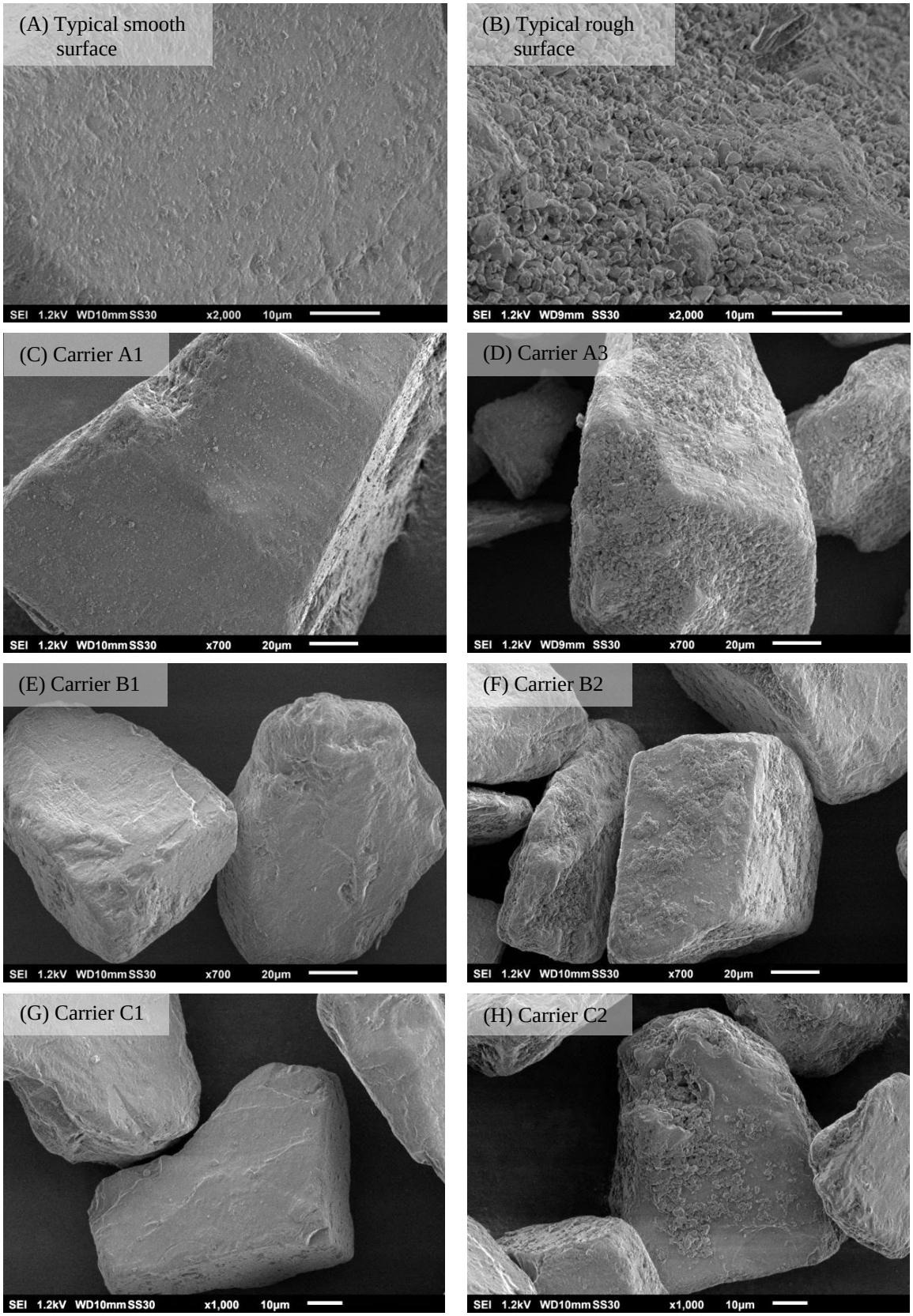

Figure 22. Scanning electron micrographs of the surfaces of roughened and smoothened carrier particles. Images (A) and (B) are representative smoothened and roughened surfaces at higher magnification of 2000x and (C) – (H) are the smoothened and roughened particles from different size fractions at lower magnifications of 700x and 1000x.

Table 8. Surface roughness and specific surface area of fluid-bed coated lactose particles

Carrier code*	Mean R_a (nm)	Coefficient of variation (%)	Change in R_a (%)**	Specific surface area (m^2/g)	Change in specific surface area (%)**
A1	437 (215)	49	-	0.230 (0.023)	-
A2	522 (299)	57	+ 19	0.258 (0.019)	+ 12
A3	726 (275)	38	+ 66	0.282 (0.014)	+ 23
B1	442 (237)	54	-	0.278 (0.019)	-
B2	703 (229)	33	+59	0.322 (0.059)	+16
B3	478 (258)	54	-	0.281 (0.020)	-
B4	653 (288)	44	+ 37	0.310 (0.005)	+ 10
C1	639 (392)	61	-	0.356 (0.024)	-
C2	635 (306)	48	- 0	0.415 (0.044)	+ 17
C3	698 (318)	46	+9	0.414 (0.004)	+ 16

*Carriers A1 – B2 were obtained when feed P1 was used. Carriers B3 – C2 were obtained when feed P2 was used. Carrier C3 was obtained when feed P3 was used.

**% change in R_a and specific surface area of the roughened lactose carriers were calculated with reference to the smoothened carrier, which was obtained from the same feed powder and had the same particle size range. The reference lactose carrier was (i) A1 for carriers A2 and A3, (ii) B1 for carrier B2, (iii) B3 for carrier B4 and (iv) C1 for carriers C2 and C3.

Values in parenthesis represent the respective standard deviation

There are several reasons which may account for the lower degree of surface roughening when feed powders of smaller particle sizes were used; larger specific surface area, segregative flow in the fluid-bed chamber and more agglomeration between the smaller particles during fluidization. An attempt was made to reduce the effect of the differences in specific surface area of feeds P1, P2 and P3, by adjusting the amount of micronized lactose sprayed based on the total surface area of the feed powder. It was more difficult to avoid segregative suspension heights of the fluidizing material as particle size and span were the primary variables investigated. Segregation was more likely to occur in feed P2 due to the larger span value of 2.08 compared to 0.88 in feed P1. Interestingly, it has been reported that the addition of fines to a mixture of small and large particles further enhances segregation during fluidization (131). Computer simulations in the same study suggested that segregation increased when as low as 1 %, w/w fines were present. This was because the inter-particle interactions between small and large particles were reduced noticeably. In the present study, micronized lactose accumulated in the product chamber with the increase in spraying time. Hence, the efficiency of surface roughening in small particles would be expected to decrease even further with time. Lastly, the degree of particle agglomeration in the fluid-bed chamber was expected to increase as the particle size was decreased due to the cohesiveness of smaller particles. This would in turn hinder the wetting and deposition of spray droplets around the surfaces of the smaller feed particles when compared to the larger particles.

4.2.1.4 Extent of surface roughening in particles of different sizes within the same feed powder

The results in Table 8 also show that the extent of surface roughening was always greater in the larger carrier particles that were fractionated from the same feed powder. This suggests non-uniformity in surface roughening of particles within the same feed powder.

There was a larger percentage increase in R_a for carrier A3 (+ 66 %) compared to B2 (+ 59 %) as well as for carrier B4 (+ 37 %) compared to C2 (- 0 %). The differences in R_a between different-sized particles were smaller in feed P1 than in feed P2. There could be 3 possibilities for the above observations: (a) the specific surface area of smaller particles are greater and more micronized fines have to be deposited around the particles to achieve the same R_a values, (b) the tendency for adhesion of micronized fines to particle surfaces is lower for smaller particles and (c) segregation of particles during fluidization leads to much lower probability of smaller particles passing through the spray zone located at the lower region of the fluid-bed chamber. Of these various possibilities, the segregation effect could be studied by repeating the fluid-bed process using feed particles of comparable d_{50} value but with narrower size distribution.

Feed P3 was used to investigate whether the segregation effect could be reduced when the size distribution of the feed powder was narrower. The particle size data in Table 1 (Page 56) and Table 7 (Page 100) show that carrier C3 was derived from the largest particles in feed P3. The size ranges (i.e., d_{10} – d_{90}) of feed P3 and carrier C3 were 16 – 86 µm and 41 – 92 µm, respectively. Hence, carrier C3 was expected to be efficiently roughened at the spray zone near the bottom of the chamber even when segregation of the feed based on particle size was significant during coating. Surprisingly, only a marginal increase in the R_a was observed and this suggests that segregation may not be the predominant reason for the poor surface roughening effect for smaller particles. It has been reported elsewhere that finer particles are fluidized in the form of cohesive agglomerates (132). Larger particles, on the other hand, can exist individually in the fluidizing bed (133). The agglomeration and subsequent separation of small particles would have prevented the spray droplets from wetting of single particles effectively and thus, prevented the surface deposition of fines on smaller particles. In addition, there is

an increased tendency of wetted particles to form larger aggregates in the fluid-bed. It was reported that the capillary liquid bridge forces were generally stronger than the fluid drag and particle-particle collision forces and restricted the motion of individual particles in wet agglomerates (134). The presence of 60 %, v/v IPA in the suspension media for micronized lactose was meant to reduce the agglomerative effects since the solubility of lactose in IPA is minimal and the latent heat of vaporization of the mixture was decreased significantly (48). Therefore, if agglomeration occurs during fluid-bed coating, the liquid and solid bridges formed between the particles would be weak and likely to break down during fluidization. Agglomeration is detrimental to the fluid-bed coating process as particle surfaces within the agglomerates would be shielded and remain un-coated. The reduction in particle-particle agglomeration and increased rate of drying may be achieved with higher airflow rates. However, it was observed that higher airflow rates led to finer particles being rapidly trapped in the filters and decreased the product level in the chamber. The minimum airflow rate required for fluidization, just sufficient to keep the entire powder bed in motion, was therefore maintained during the processes. Lastly, the size of spray droplets is not likely to be a major contributory factor to non-uniform surface roughening of large and small particles in the same feed batch. Researchers have reported that spray droplets produced from a two-fluid spray nozzle, with 1 mm nozzle diameter at an atomizing pressure of 2.5 bars, ranged from approximately 1 – 15 µm (135). This droplet size range on exiting the spray nozzle was still considerably smaller than the particles in the range of 38 – 63 µm. Hence, there were limited improvements which could be effected from changes in other experimental conditions. The poorer surface roughening action for particles smaller than 80 – 100 µm appeared to be a limitation of fluid-bed coating to produce roughened carrier particles.

4.2.2 Part 2B: Dry granulation by roller compaction

4.2.2.1 Particle size distributions of raw lactose powders and powder blends used in roller compaction

The particle size distributions of the raw powders (lactose 100M, 200M and 400M) are shown in Figure 23. Lactose 100M had the largest d_{50} value of 161 µm and the narrowest size distribution. Lactose 200M and 400M had d_{50} values of 34 µm and 10 µm, respectively. By blending lactose 100M with either one of the finer lactose grades (Table 3, Page 61), powder blends with different size distributions and flow characteristics for roller compaction were obtained. It can be deduced that the size distributions of these blends would not follow the 'model' normal or log-normal distributions but would generally be bimodal in nature.

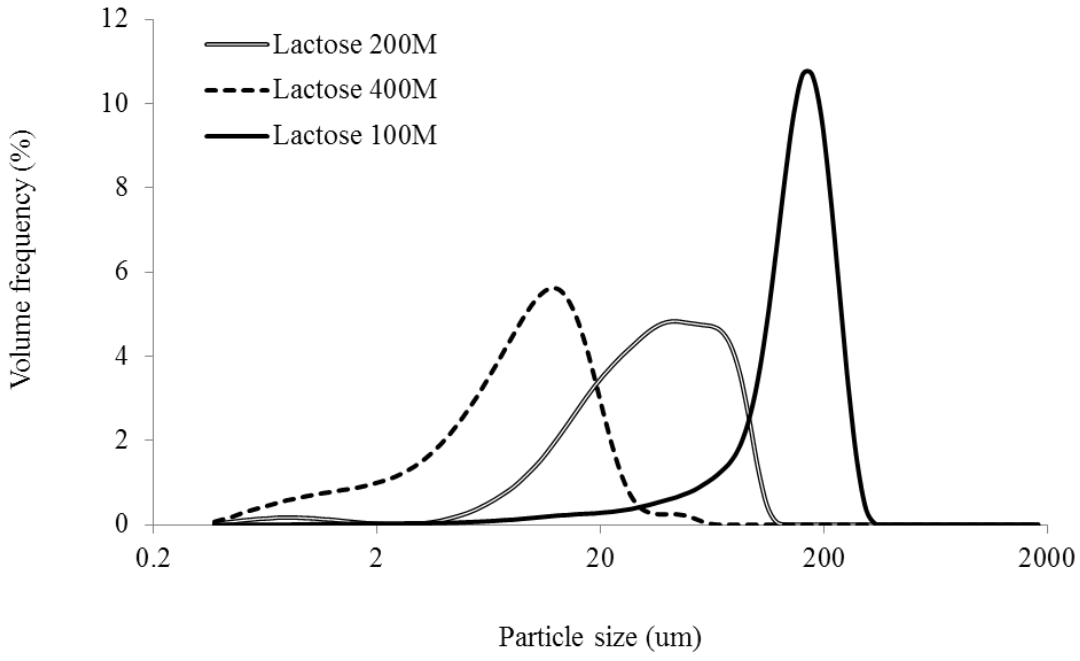

Figure 23. Particle size distributions of lactose 100M, 200M and 400M.

The particle size distribution of each powder blend is presented in Table 9. The blend codes were labeled according to decreasing d_{50} for the ease of data analysis. The d_{50} values had varied predictably according to the proportion and size of fine lactose added to the blends. The addition of the finer grades of lactose 200M or 400M to coarser particles of lactose 100M always led to the decrease in d_{50} values but the increase of the span values. Compared to blends with lactose 200M (F2, F4, F5), the addition of increasing proportions of lactose 400M (F3, F7, F8) resulted in much greater decrease in the d_{10} and to a lesser extent, the d_{50} and d_{90} values. Interestingly, blends F7 and F8, which consisted of 50 % and 75 %, w/w of lactose 400M respectively, had almost the same d_{10} and d_{50} values compared to lactose 400M on its own. However, the span value of blend F7 was the greatest among all the blends. The above trends were not observed with lactose 200M.

4.2.2.2 Flow properties of powder blends

Powder flow properties of the blends were evaluated using flow parameters/methods described in the USP; angle of repose, Hausner ratio, cohesion (shear cell). The blends were also tested in the powder rheometer and 2 other flow parameters, BFE and specific energy, were obtained. The bulk densities and Hausner ratios are presented in Figure 24. The bulk densities decreased as the particle size decreased. According to the classification scale of powder flowability in the USP (136) based on the Hausner ratios, the flowability of the powder blends used in this study ranged from ‘passable’ (F1) to ‘very very poor’ (F8). The Hausner ratio and powder cohesion described very similar trends in flow among the blends. In general, a decrease in the particle size increased powder cohesion and led to larger Hausner ratios. A wider size distribution in blend F3 contributed to deviations from the general trends for bulk density, Hausner ratio and

Table 9. Particle size distributions of powder blends used in roller compaction

Powder	Particle size (um)			Span
	d_{10}	d_{50}	d_{90}	
F1	68 (2)	161 (0)	237 (1)	1.0 (0.0)
F2	25 (1)	140 (1)	229 (0)	1.5 (0.0)
F3	5 (0)	90 (6)	189 (6)	2.1 (0.1)
F4	14 (1)	73 (3)	182 (10)	2.3 (0.0)
F5	11 (0)	45 (3)	143 (20)	2.9 (0.3)
F6	10 (3)	34 (3)	86 (6)	2.2 (0.4)
F7	2 (0)	12 (0)	60 (8)	5.0 (0.6)
F8	2 (0)	11 (0)	23 (1)	1.9 (0.1)
Lactose 400M	2 (0)	10 (0)	20 (0)	1.9 (0.0)

F1 and F6 represent lactose 100M and lactose 200M, respectively
Values in parenthesis represent the respective standard deviation

powder cohesion. The d_{90} values of F3 and F4 (about 180 μm) were similar. However, the d_{10} of F3 (5 μm) was much smaller that of F4 (14 μm), indicating that F3 has a relatively larger proportion of fines below 5 μm. The results suggest that a larger proportion of such fines had a significant detrimental effect on the packing density and powder flow.

The large angles of repose in all powder blends (Figure 25) indicate that the powders ranged from having poor to very poor flowability. The trends in the angle of repose coincided with the trends in powder cohesion for blends F1 – F5 but not for F6 – F8 (i.e., typically the greater the powder cohesion, the larger the angle of repose). This was likely due to the tendency for the formation of spherical cohesive agglomerates in very

cohesive powders (blends F6 – F8) as they passed through 1.0 mm sieve apertures during the measurement of angle of repose. These cohesive agglomerates exhibited slightly better flow properties than the individual particles in less cohesive powders, resulting in a lower angle of repose. Hence, the results suggest that the angle of repose may not be a suitable flow parameter for assessing flow of lactose powders when their cohesion exceeded 2 kPa, corresponding to the cohesion value of blend F5.

The BFE and specific energies of each powder blend is shown in Figure 26. The BFE decreased with decreasing d_{50} while the specific energy showed the opposite trend. Both these parameters are energy parameters which describe the amount of work required to induce powder flow under different stress states of the powder. Due to the helical shape of the blade, some compressive action is generated in the region of powder immediately below the blade as it traverses downwards into the powder column. Different degrees of compressive action may be induced by separately modifying the rate of rotation of the blade as well as the rate that it moves vertically downwards into the powder bed. The BFE is a measure of the energy required to drive the rheometer blade through the powder bed, originally in a loosely packed state, while inducing powder flow when the powder is in a slightly compressed state. The specific energy, on the other hand, is the energy expended per unit weight of the powder during the upward motion of the blade which results in gentle lifting and flow in a low stress state of the powder.

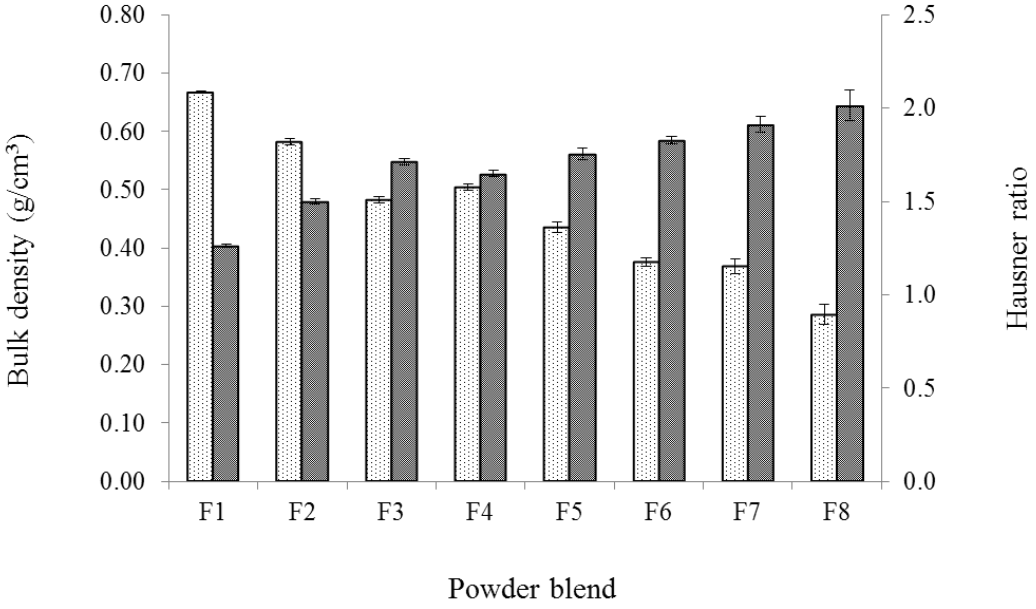

Figure 24. Bulk densities (□) and Hausner ratios (▩) of powder blends used in roller compaction.

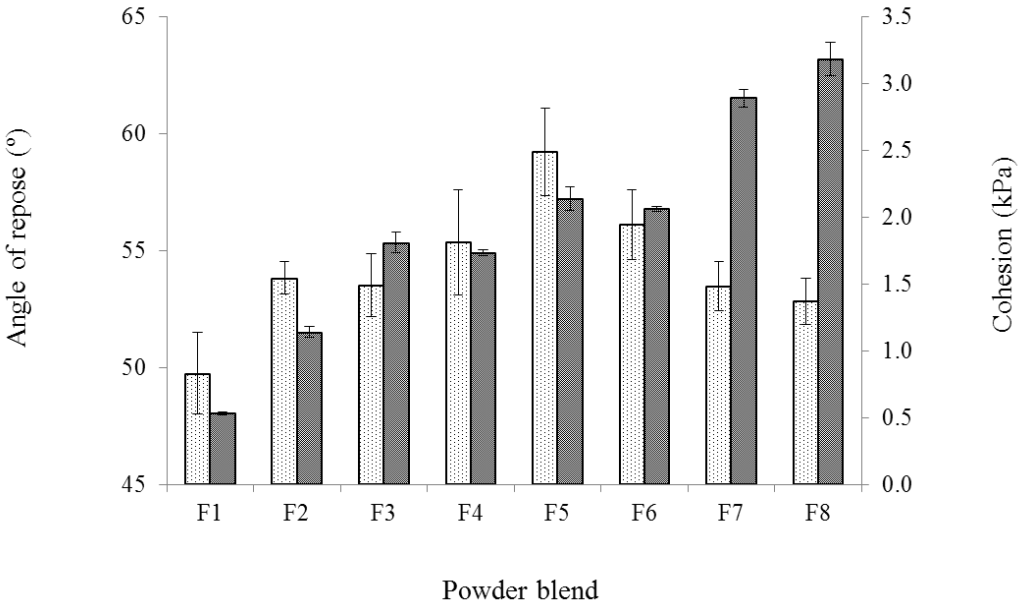

Figure 25. Angles of repose (□) and cohesion (▩) of powder blends used in roller compaction.

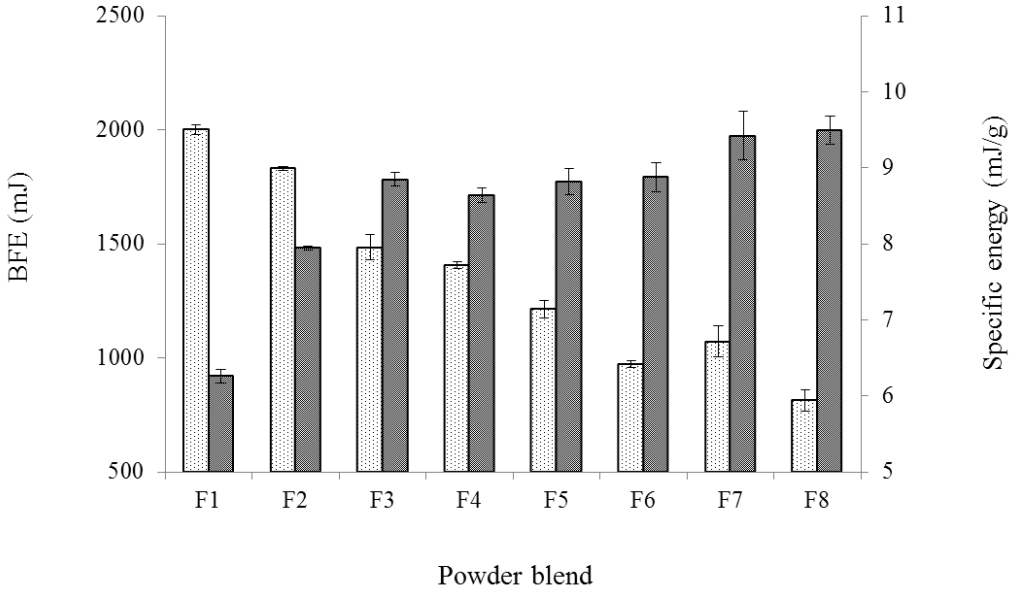

Figure 26. Basic flowability energies (BFE; ⊡) and specific energies (▩) of the powder blends used in roller compaction.

4.2.2.2.1 Correlations among flow parameters

The Hausner ratio is a much more widely-used and reported flow parameter compared to the BFE and specific energy. Therefore, the suitability of the BFE and specific energy in the evaluation of powders with 'passable' to 'very very poor' flow properties (i.e., Hausner ratio between 1.25 – 2.0) was established by correlating them to the Hausner ratio. The linear correlation coefficients between the Hausner ratio and both the BFE and specific energy are shown in Figure 27. The linear correlation coefficients between the cohesion and both the BFE and specific energy are shown in Figure 28. Both the BFE (R^2 = 0.93) and specific energy (R^2 = 0.92) were found to exhibit stronger linear relationships with Hausner ratio than powder cohesion.

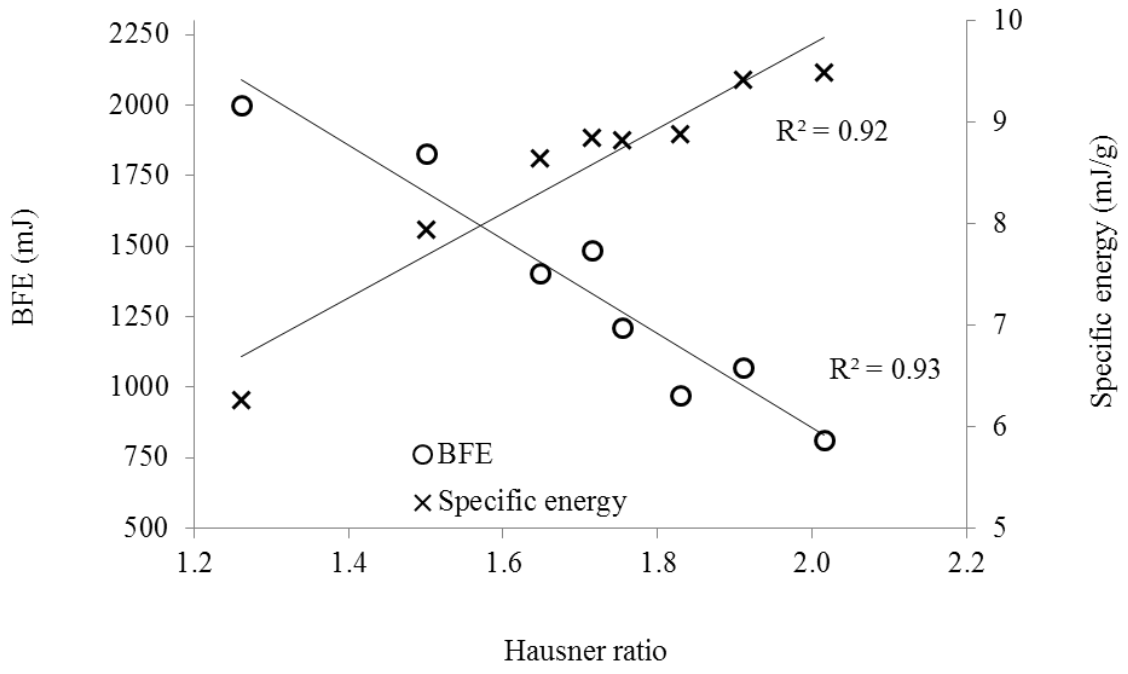

Figure 27. Relationships between the different flow parameters of the powder blends: Hausner ratio, BFE (basic flowability energy) and specific energy.

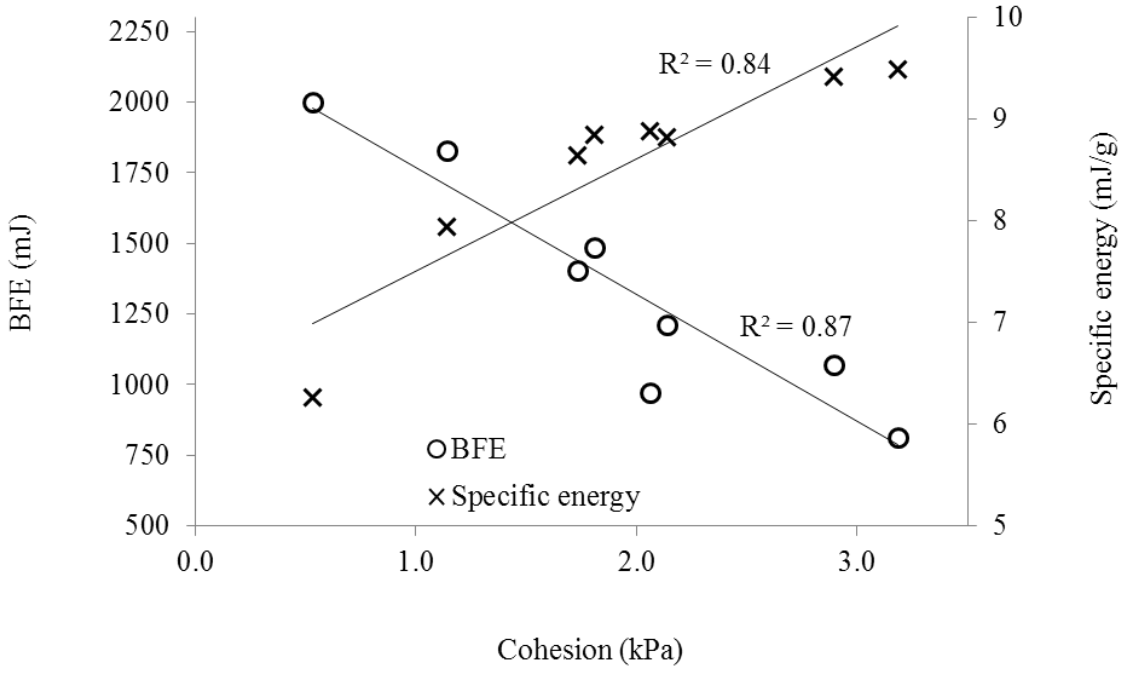

Figure 28. Relationships between the different flow parameters of the powder blends: cohesion, BFE (basic flowability energy) and specific energy.

4.2.2.2.2 Correlations between particle size and flow parameters

As a result of their bimodal size distributions, the d_{50} values of the powder blends did not always correlate well with powder flow. It was observed previously (Tables 3 and 9) that the addition of a small proportion of fine lactose (i.e., 25 %, w/w) to coarse lactose 100M resulted in the largest degree of change in the d_{10} compared to the d_{50} or d_{90} values. When a sufficiently small proportion of lactose fines is present with the coarse particles (or vice versa), the flowability of the powder will be altered but the d_{50} value may be unchanged due to the small volume percentage of the fines. It was thought that certain flow parameters would be influenced to a greater extent by the presence of fine particles than others. In order to investigate the effect of the size distribution on each of the four flow parameters used in this study, a series of d_x values (d_{10}, d_{15}, d_{25}, d_{35}, d_{60}, d_{75}, d_{90}, d_{95}) of each powder blend was calculated (Table 10). Discrete values of d_x were employed because most of the powder blends were unable to fit to commonly utilized model distributions such as the log-normal or Weibull distributions. This can clearly be seen from the size distribution graphs of the various powder blends plotted in Figure 29.

The linear correlation coefficients of every set of d_x values with the four flow parameters were obtained and are shown in Figure 30. It was observed that the highest correlation was obtained for the d_{50} with the cohesion, Hausner ratio and BFE, while the d_{15} was best correlated with the specific energy. Across the various d_x values, however, the trends in the correlation coefficients were found to be very different for the different flow parameters. For the cohesion and Hausner ratio, the correlation coefficients ranged between 0.71 – 0.92 and were lower for d_{10} – d_{35} as well as for d_{60} – d_{95} as compared to the d_{50} value. For the specific energy, the correlation coefficients were greater than 0.95 for d_{10} – d_{25} and decreased steadily from 0.88 – 0.60 for d_{35} – d_{95}. An opposite trend was

Table 10. Particle sizes at different volume percentages of powder blends used in roller compaction

Blend code	Particle size (μm)								
	d_{10}	d_{15}	d_{25}	d_{35}	d_{50}	d_{60}	d_{75}	d_{90}	d_{95}
F1	68.0	83.9	120.5	121.8	161.0	161.2	200.7	236.7	234.1
F2	25.3	35.2	72.6	101.1	140.3	146.8	187.8	228.9	234.1
F3	5.1	7.2	12.2	16.7	90.0	121.8	159.2	189.4	194.2
F4	14.4	18.3	29.6	39.8	73.1	95.1	145.5	181.9	182.6
F5	11.3	14.3	22.5	28.4	45.1	54.5	96.4	143.1	148.1
F6	9.8	12.4	19.2	22.9	34.4	37.5	58.8	86.4	92.4
F7	2.3	3.4	6.4	7.7	11.6	12.6	18.5	59.9	67.9
F8	2.1	3.2	6.2	7.4	11.0	11.8	16.2	23.1	32.0

(A)

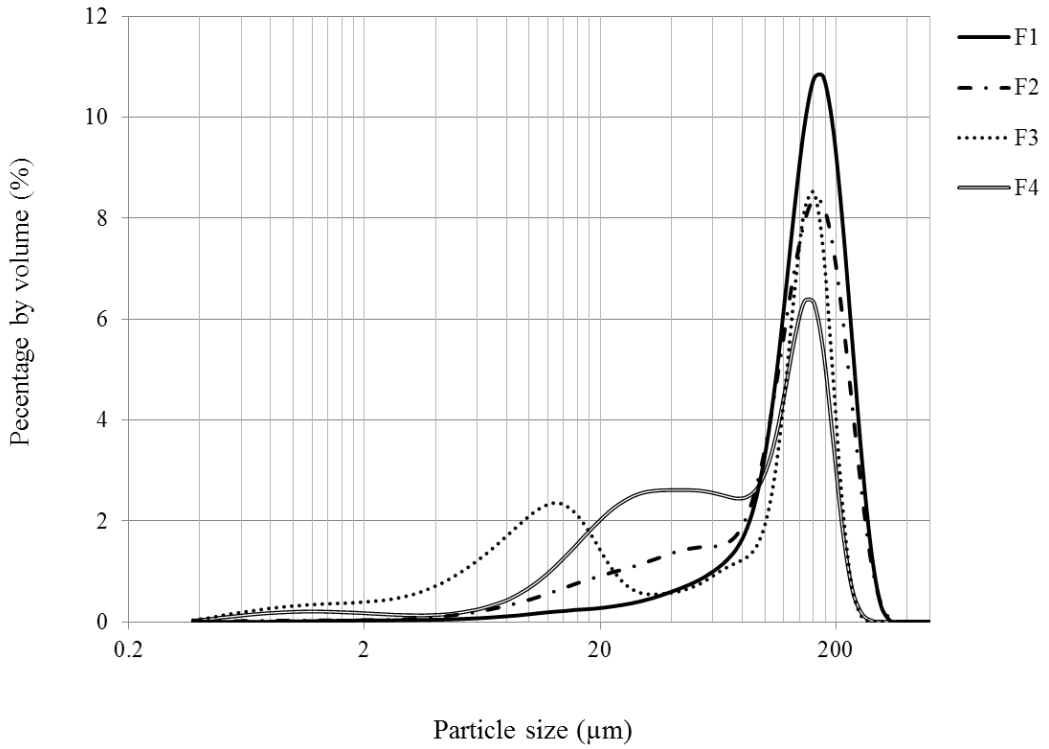

(B)

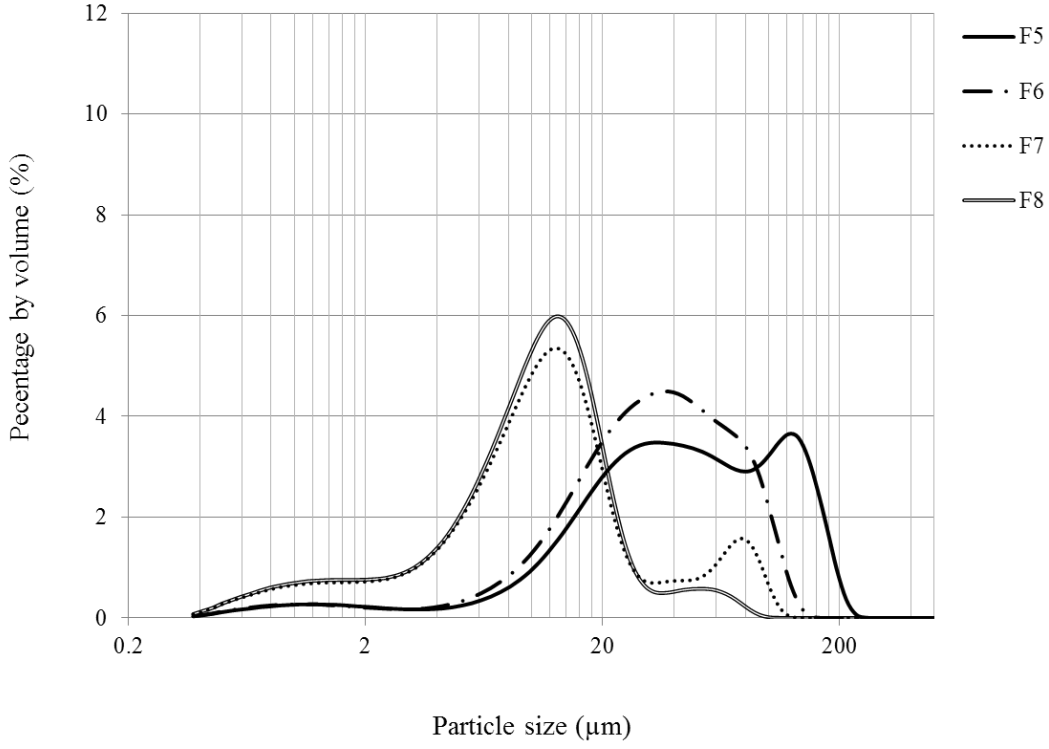

Figure 29. Particle size distributions of powder blends (A) F1 – F4 and (B) F5 – F8 used in roller compaction.

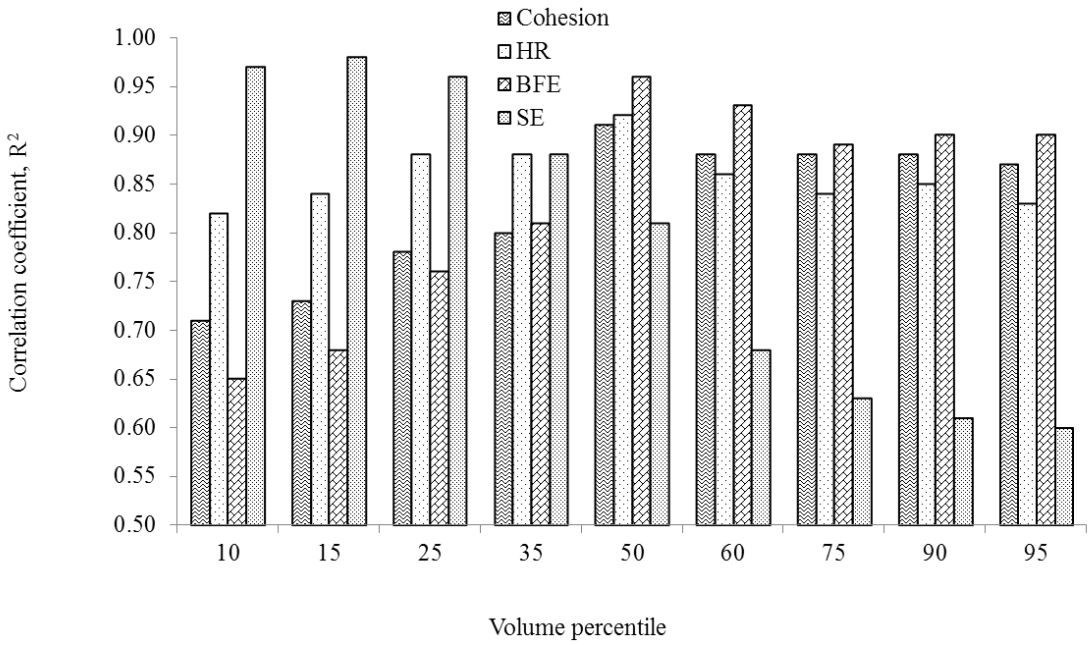

Figure 30. Linear correlation coefficients (R^2) obtained when different d_x values were plotted against the 4 flow parameters: cohesion (▨), Hausner ratio (⊡), basic flowability energy (▨) and specific energy (▨). Each R^2 value was obtained by plotting the particle sizes corresponding to the x^{th} volume percentile (d_x) of all powder blends (F1 – F8) against the corresponding values of the flow parameter.

observed for the BFE, where the coefficients were greater than 0.90 for d_{50} and above but decreased to 0.81 – 0.65 for d_{35} and below. The results suggest that the specific energy was much more sensitive to the size of the finer particles in the blend while the BFE was more dependent on the composition of the entire blend. The BFE has been reported to be partly dependent on the bulk compressibility of the powder (126), since it was a measure of the energy required to generate a compressive action by the blade during the test. This was also observed from the good linear relationship between BFE and bulk density shown in Figure 31. As slightly higher linear correlation coefficients could be obtained for the BFE and specific energy (compared to the cohesion/Hausner

ratio) when the suitable d_x value was selected, these 2 flow parameters could potentially be used as better predictors of powder flow.

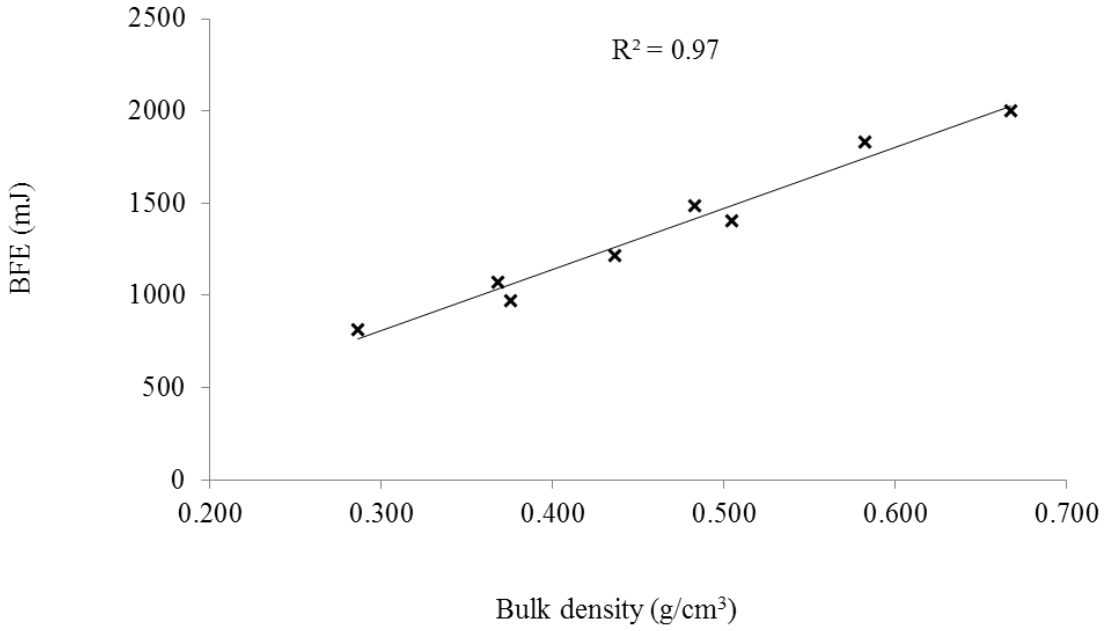

Figure 31. Graph showing the linear relationship between the BFE and bulk density of powder blends.

4.2.2.3 Variation in roll force during compaction

The results in Table 11 show the mean roll force and screw speed recorded for each powder blend during each successful compaction run. Consistent compaction parameters during compaction generally lead to smaller variation in the quality of ribbons produced. Reduced variation in the degree of particle fragmentation/bonding during compaction is always more desirable as it leads to reduced variation in the resultant surface roughness. The compaction parameters set might vary during compaction due to the influence of the feed materials. Several observations could be made regarding the size and flow

properties of the blends and the roller compaction parameters. It was noted that there was greater difficulty in achieving the higher roll forces in powder blends with smaller particle size or poorer flow. Blends F7 and F8 could not be successfully compacted at 20 kN/cm while blends F4 – F8 could not be successfully compacted at 30 kN/cm. Blends F1 – F3, on the other hand, could be successfully compacted at all the three roll forces used. The variation of roll force recorded was also found to differ significantly among the powder blends. It was observed that blend F1, despite having the largest particle size and best flowability, resulted in the most significant variation of roll force during compaction. This could be inferred from the larger standard deviations of the roll force and screw speed recorded. Blends F3 and F6 – F8 were also found to exhibit higher variation in roll force when compacted at 10 kN/cm. A similar trend could be observed in blends F1, F3 and F6 at the roll force of 20 kN/cm and in blends F1 and F3 at the roll force of 30 kN/cm. Hence, it could be seen that certain intrinsic powder properties had contributed to the variation in roller compaction parameters regardless of the compaction force used.

Interestingly, the particle size distributions of the blends which resulted in greater variation in the compaction parameters (F1, F3 and F6 – F8) could be divided into two categories: (a) powders of very coarse particle size and with minimal amount of particles smaller than 50 μm (F1) and (b) powders with greater than 15 % (by volume) of fine particles smaller than 10 μm. It appeared that an optimal particle size distribution, such as that of blend F2, was required to achieve both a wide range of target roll forces (10 – 30 kN/cm) as well as minimal variation in roll force during compaction. Figure 32 is a schematic diagram of the roller compactor showing the counter-rotating rolls and the nip region where powder is being densified and compacted into ribbons. For blends with

Table 11. Mean roll force and screw speed recorded for different powder blends during roll compaction

Blend code	Target roll force (kN/cm)					
	10		20		30	
	Roll force (kN/cm)	Screw speed (rpm)	Roll force (kN/cm)	Screw speed (rpm)	Roll force (kN/cm)	Screw speed (rpm)
F1	9.9 (4)	21.5 (5.3)	19.8 (1.5)	50.4 (3.4)	29.7 (1.1)	56.9 (2.0)
F2	10.0 (0.4)	24.4 (0.2)	19.8 (0.6)	39.3 (1.1)	30.0 (0.8)	46.5 (0.4)
F3	10.0 (0.9)	30.2 (2.0)	20.2 (1.3)	37.5 (2.7)	29.8 (1.2)	44.7 (2.0)
F4	10.0 (0.6)	28.2 (0.7)	19.4 (0.9)	43.3 (4.0)	-	-
F5	10.0 (0.6)	27.8 (0.3)	18.1 (0.8)	52.9 (7.7)	-	-
F6	9.8 (1.0)	31.5 (2.9)	19.2 (2.1)	49.5 (6.8)	-	-
F7	10.0 (1.2)	43.8 (2.5)	-	-	-	-
F8	8.8 (1.0)	46.3 (6.5)	-	-	-	-

Values in parenthesis represent the respective standard deviation

poor flow and low bulk densities (F3 and F6 – F8), the roll force fluctuations were likely to be due to the intermittent feeding of material into the nip region. The feed remained largely static around the slip region immediately after discharge from the hopper until a substantial amount of powder had been accumulated and cascaded towards the nip region. On the other hand, the most free-flowing powder (F1) caused rapid flooding into

the nip region and the excessive built-up powder between the rolls caused the spikes in the roll force. Consequently, the feedback controls resulted in drastic decrease in the screw speed, which in turn reduced the feed delivery and the roll force significantly. In both situations, the automatic adjustments in screw speed by the roller compactor was ineffective at maintaining a continuous and consistent feed flow which translated into the recorded peaks and troughs instead of a constant roll force.

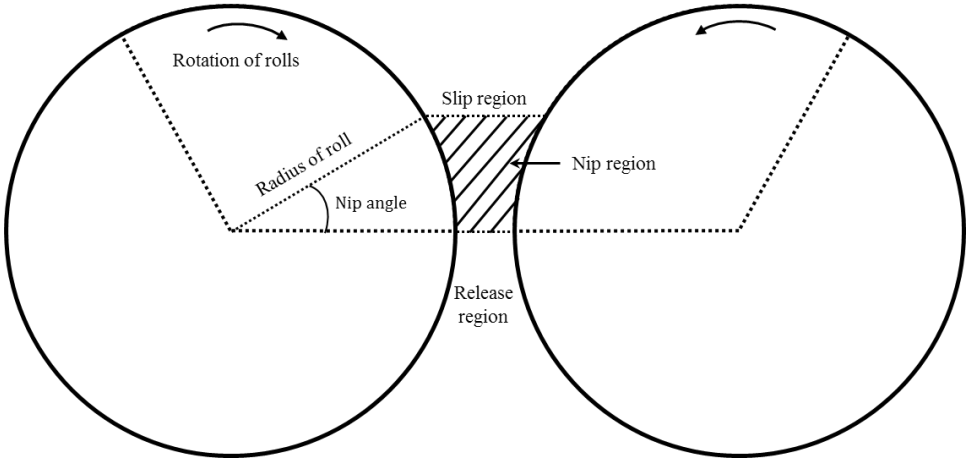

Figure 32. Schematic diagram of the roller compactor showing the slip, nip and release regions.

4.2.2.3.1 Prediction of roll force variations using flow parameters

The powder blends were ranked according to their flowability in Figure 33. Powder blends which resulted in greater variability in roll force and screw speeds are encircled. With the exception of the angle of repose, the ranked order for each flow parameter shows that there was greater agreement among the flow parameters when the flow properties were at the extreme ranges. More discrepancies among the flow parameters were observed for powders exhibiting intermediate flow properties. It should be recalled

that F1, F3 and F6 – F8 showed greater variation in compaction parameters during compaction. The specific energy appeared to be the only flow parameter which reflects this best. The ranked sequences of the other flow parameters were not always related to the variation in roll force encountered. Powder blends with specific energy in the range of 7.9 – 8.8 mJ/g (blends F2, F4 and F5) were found to result in more consistent compaction parameters during compaction.

Flow parameter	**Rank in powder flowability**							
	Least free-flowing → Most free-flowing							
Hausner ratio	F8	F7	F6	F5	F3	F4	F2	F1
Cohesion	F8	F7	F5	F6	F3	F4	F2	F1
Angle of repose	F5	F6	F4	F2	F3	F7	F8	F1
BFE	F8	F6	F7	F5	F4	F3	F2	F1
Specific energy	F8	F7	F6	F3	F5	F4	F2	F1

Figure 33. Powder blends ranked according to their flowability based on the values of each flow parameter. The blend codes encircled indicate blends that showed higher variability in both the roll force and screw speed during compaction.

4.2.2.4 Surface roughness of roller compacted carrier particles

The R_a values of the carriers obtained from all formulations at the three different roll forces are presented in Table 12. There were no clear relationships between the type of powder blend and the resultant carrier roughness. Most notably, however, carriers obtained from powders comprising higher percentages of lactose 400M (i.e., F7 and F8) resulted in relatively low R_a values among other carriers. Compared to the composition

of the powder blend, the magnitude of compaction forces exerted on the powders had a greater influence over the R_a values and thus was investigated using the ANOVA. The results in Table 13 show that the R_a of the INH (573 nm) and L100M carriers (562 nm) were not significantly different from each other ($p = 0.42$). The R_a values of the roller compacted carriers were significantly higher ($p < 0.01$) than the INH or L100M carriers, regardless of the roll force used. Among the roller compacted carriers, the R_a values of those compacted at 20 kN/cm were significantly higher ($p < 0.01$) than those compacted at 10 kN/cm but were not statistically different ($p = 0.77$) from those compacted at 30 kN/cm. These results suggest that roller compaction was effective in increasing the R_a value from 10 – 20 kN/cm but there was no evidence of further increase from 20 – 30 kN/cm.

Table 12. Surface roughness of carrier particles prepared by roller compaction at different roll forces

Blend code	R_a (nm)		
	Target roll force (kN/cm)		
	10	20	30
F1	998 (46)	1055 (63)	1022 (19)
F2	855 (96)	1086 (30)	1104 (42)
F3	900 (171)	828 (38)	952 (147)
F4	739 (177)	1117 (147)	-
F5	969 (189)	1177 (136)	-
F6	804 (227)	1006 (26)	-
F7	702 (146)	-	-
F8	494 (211)	-	-

Values in parenthesis represent the respective standard deviation

Table 13. Results of the one-way ANOVA on the R_a of different batches of carrier particles

Pair of samples under comparison					
	INH	L100M	$Carrier_{10}$	$Carrier_{20}$	$Carrier_{30}$
INH	-	0.42	< 0.01	< 0.01	< 0.01
L100M	-	-	< 0.01	< 0.01	< 0.01
$Carrier_{10}$*	-	-	-	< 0.01	< 0.01
$Carrier_{20}$*	-	-	-	-	0.77
$Carrier_{30}$*	-	-	-	-	-

Values in the table refer to the p-values and $p < 0.05$ denotes statistical significance

*$Carrier_{10}$, $Carrier_{20}$ and $Carrier_{30}$ denotes all carrier batches produced by roller compaction at roll forces of 10, 20 and 30 kN/cm, respectively

Representative SEM images of carrier particles produced at different compaction forces are shown in Figure 34. Gradual morphological changes were observed as the compaction force increased. Figure 34A shows the general morphologies of uncompacted α-lactose monohydrate crystals. Figure 34B shows that the morphologies of the particles were retained after being subjected to a low compaction force of 10 kN/cm. However, the surfaces were slightly more irregular compared to the crystallized particles due to some fusion of finer lactose on coarse particle surfaces. At compaction forces of 20 and 30 kN/cm, particle fragmentation was evident and the carrier particles were irregularly-shaped aggregates of particle fragments (Figure 34C and D). The results suggest that highly irregular rough carrier particles are obtained only when the compaction force was high enough to cause extensive particle fragmentation, followed by the bonding of particle fragments.

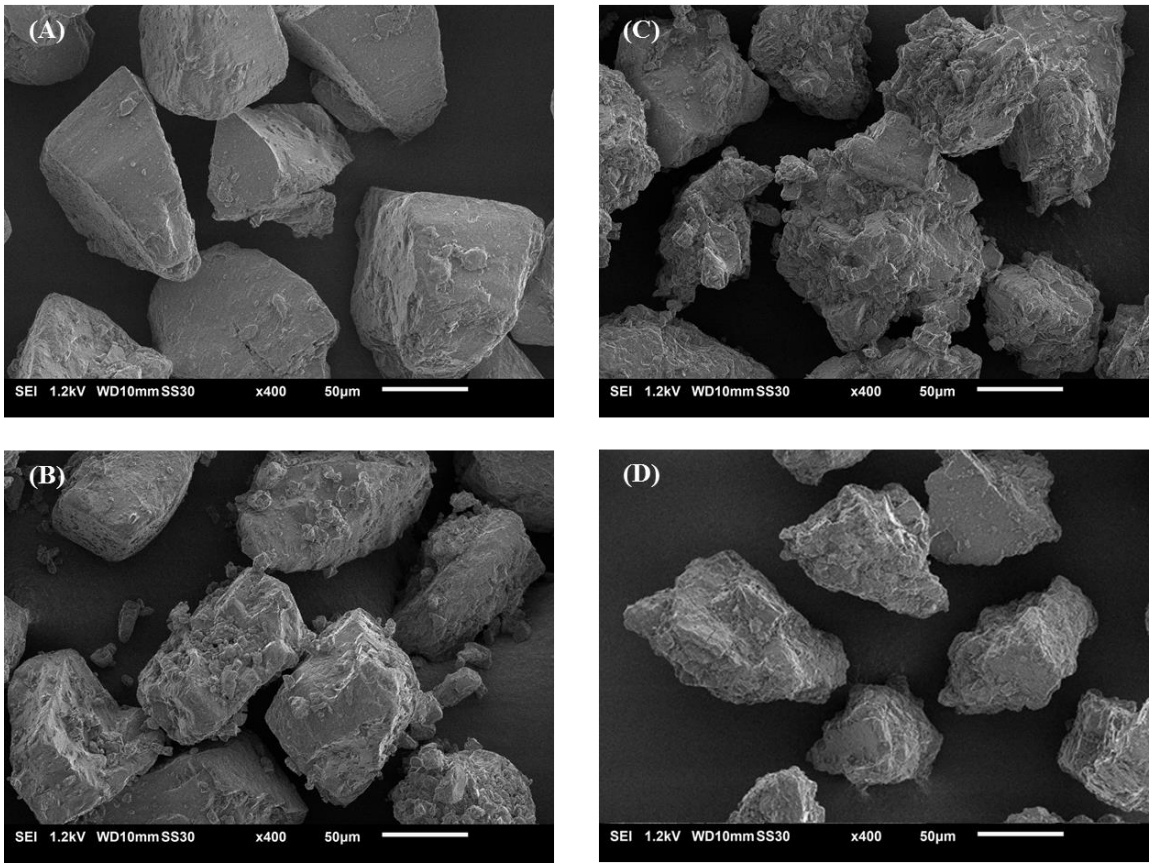

Figure 34. SEM images showing the gross morphologies as well as surface roughness of the different lactose carriers. The images show (A) the INH carrier and the roller compacted carriers obtained by compaction of (B) F8 at 10 kN/cm, (C) F5 at 20 kN/cm and (D) F2 at 30 kN/cm.

4.2.3 Summary of Part 2

In this study, in-depth investigations into the two carrier surface modification methods were carried out. The primary goal in Parts A and B of the study was to identify the physical properties of lactose powders and the processing conditions in each method that would result in lactose carriers with suitably high R_a. In surface roughening by fluid-bed coating, the larger starting particle size of the core was the most important factor leading to higher carrier R_a. Surface roughening effects were not very significant when the size of core particles were predominantly smaller than 100 µm, even after the amount of

sprayed micronized lactose was adjusted for the total surface area of the core particles. Surface roughening was not improved significantly even though the segregation tendency during fluidization was reduced by processing core particles with a narrower size distribution. The most probable cause was identified to be the intrinsic agglomeration of smaller cohesive particles during fluidization. This had prevented efficient wetting, spreading and drying of the spray droplets for deposition of micronized lactose on the coarser particles. Alternative strategies for obtaining carriers with higher R_a include: (a) increasing the amount of micronized lactose sprayed (only applicable to core particles larger than 100 μm) and (b) obtaining larger particle fractions from the processed powders.

In surface roughening by roller compaction, carriers with significantly higher R_a values were produced. For successful compaction of powder blends at the desired roll force, the particle size, bulk density and powder flow had to exist within a certain range of values. The variation of roll force in different compaction runs was also investigated. Powder blends with the largest and smallest particle sizes showed greater variation in compaction parameters than those with the intermediate particle size. Significantly lower variations in roll force were observed when powders were compacted at higher roll forces. The various flow parameters (angle of repose, cohesion, Hausner ratio, BFE, specific energy) showed slight differences in the rank order of the powder blends used. This was probably because the size distributions of the powder blends were bimodal in nature. Each flow parameter assessed powder flow under slightly different stress states and packing conditions. The angle of repose was found to be anomalous for very cohesive powders (cohesion greater than 2 kPa) as the angles decreased with increasing cohesion. The Hausner ratio, cohesion and BFE generally showed better agreement with each other. The specific energy was found to be most sensitive to fine particles in the

powder blends and could best account for the trends in the variation of roll force. Along with the above considerations on the processibility of powders, carrier particles of higher R_a could be produced with higher roll forces.

4.3 Part 3: Investigation of the use of roughened lactose carriers in dry powder inhaler formulations

4.3.1 Part 3A: Evaluation of the *in vitro* fine particle fraction and aerodynamic particle size distribution in interactive mixtures containing rough carriers

4.3.1.1 Size and shape of carriers

It has been reported that the study of the effect of a single physical property of any carrier (such as size, shape and surface texture) on DPI performance is virtually impossible because of the inter-dependence of the properties on one another and on the presence of fine particles (137). By the use of different conditions in fluid-bed coating and roller compaction, six coarse carriers were produced. Their mean diameters, aspect ratios and convexity values were evaluated (Table 14) to account for possible confounding factors on their DPI performance. The aspect ratio and convexity determined using optical microscopy (lateral resolution of 1.3 µm) were employed as particle shape descriptors in this study even though other researchers have used convexity as a roughness parameter (31, 46, 138). The results of the ANOVA conducted on all physical properties of the coarse carriers are shown in Table 15. The size and shape properties of the fluid-bed coated carriers (FB_S and FB_R) were not significantly different from each other ($p > 0.05$). The roller compacted carriers (RC_{50} and RC_{70}) were also similar in their shape but RC_{70} was smaller in size. The size of the INH carrier (106 µm) was more similar to the RC carriers (RC_{50}, RC_{70}; 101, 97 µm) while the size of the control carrier (113 µm) was more similar to the FB carriers (FB_S, FB_R; 118, 117 µm). The differences in size between the FB and RC carriers could be attributed to the slightly more elongated shapes of the FB carriers that allowed larger particles to pass through the same sieve apertures during air-jet sieving.

Table 14. Size, shape and surface roughness of coarse carriers

Carrier code	Physical property			
	Diameter (μm)	Aspect ratio	Convexity	R_a (nm)
Control	113 (22)	1.42 (0.26)	0.95 (0.02)	562
INH	106 (15)	1.32 (0.21)	0.97 (0.02)	573
FB_S	118 (19)	1.47 (0.28)	0.97 (0.02)	557
FB_R	117 (20)	1.47 (0.28)	0.97 (0.02)	907
RC_{50}	101 (20)	1.41 (0.26)	0.96 (0.02)	1175
RC_{70}	97 (21)	1.42 (0.27)	0.96 (0.01)	1355

Values in parentheses represent the respective standard deviation

The small differences in the absolute mean convexity values (range; 0.95 – 0.97) as well as the overlapping groups (Table 15; Tukey's test, $p > 0.05$) suggest that, with the exception of the control carrier, the differences in convexity among the carriers were not large. When the convexity and R_a were compared (Tables 14 and 15), it was clear that convexity did not reflect differences in surface roughness between the carrier batches adequately or reliably. This show that the degree of irregularity of particle outlines, when viewed under the microscope, was not a good measure of its surface properties in this study. This was probably related to the lower resolution of the optical microscope and its ability to measure only the 2D surface outlines of each particle. R_a was evaluated using the optical profiler which had higher resolution of 0.75 μm and was able to map out the 3D surface structures. It is noteworthy from these results that assessment of particle surface properties was dependent on the scale at which the particles are viewed under (i.e., resolution of the imaging method) (139).

Table 15. Statistical analyses (one-way ANOVA) of the size, shape and surface roughness of coarse carriers

Carrier code	Physical property			
	Diameter (μm)	Aspect ratio	Convexity	R_a (nm)
Control	A	A	A	A
INH	B	B	B, C	A
FB_S	C	C	B, D	A
FB_R	C	C	D	B
RC_{50}	D	A	C, E	C
RC_{70}	E	A	E	D

For each physical property, carrier batches which do not share the same letter are statistically different (Tukey's test, $p < 0.05$)

4.3.1.2 Surface roughness of coarse carriers

The distribution of R_a of each type of carrier is presented in Figure 35 and the median R_a values are presented in Table 14. The R_a of the control, INH and FB_S carriers were statistically similar while those of the FB_R, RC_{50} and RC_{70} carriers increased in the same order. Since the variability of R_a is much wider than its magnitude, it is more appropriate to present distributions of R_a values rather than a single median/mean R_a value. The R_a distribution of the FB_S carrier was largely unchanged compared to the control carrier. The R_a distribution of the INH carrier was found to be comparable to the control and FB_S carriers, suggesting that their profiles of the R_a distribution typically describe the macro-scale roughness of crystallized α-lactose monohydrate particles. By comparing the control with the FB_R carrier, it was clear that the range of R_a values (100 – 2100 nm) did not change after fluid-bed coating. Instead, a significant shift of the modal roughness from 400 to 800 nm had occurred mainly as a result of the adhesion of micronized

lactose on coarse lactose surfaces. This suggests that there was a limit to the roughening effect (up to about 1500 nm) by this method. For the roller compacted carriers, the range of R_a values (100 – 3000 nm) increased significantly compared to the control. A significant proportion of particles with very rough surfaces (R_a greater than 2000 nm) was created. This was accompanied by significant decreases in fractions of smooth particles and more uniform distribution of R_a across a wider range. The SEM images of the coarse carrier particles are shown in Figure 36.

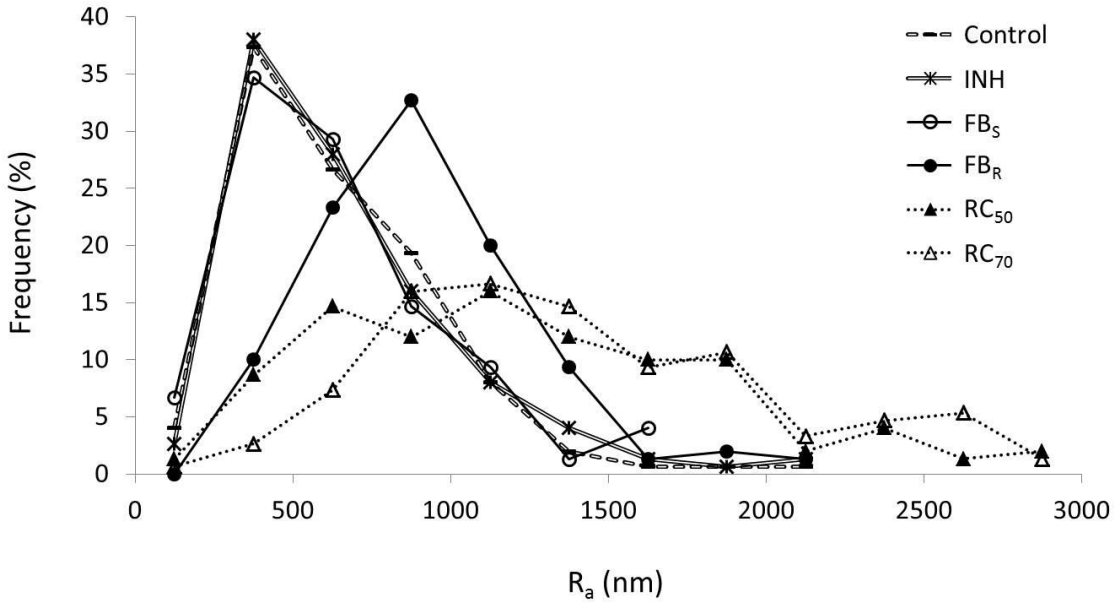

Figure 35. Distribution of R_a values (N = 150) of the six different types of coarse carriers.

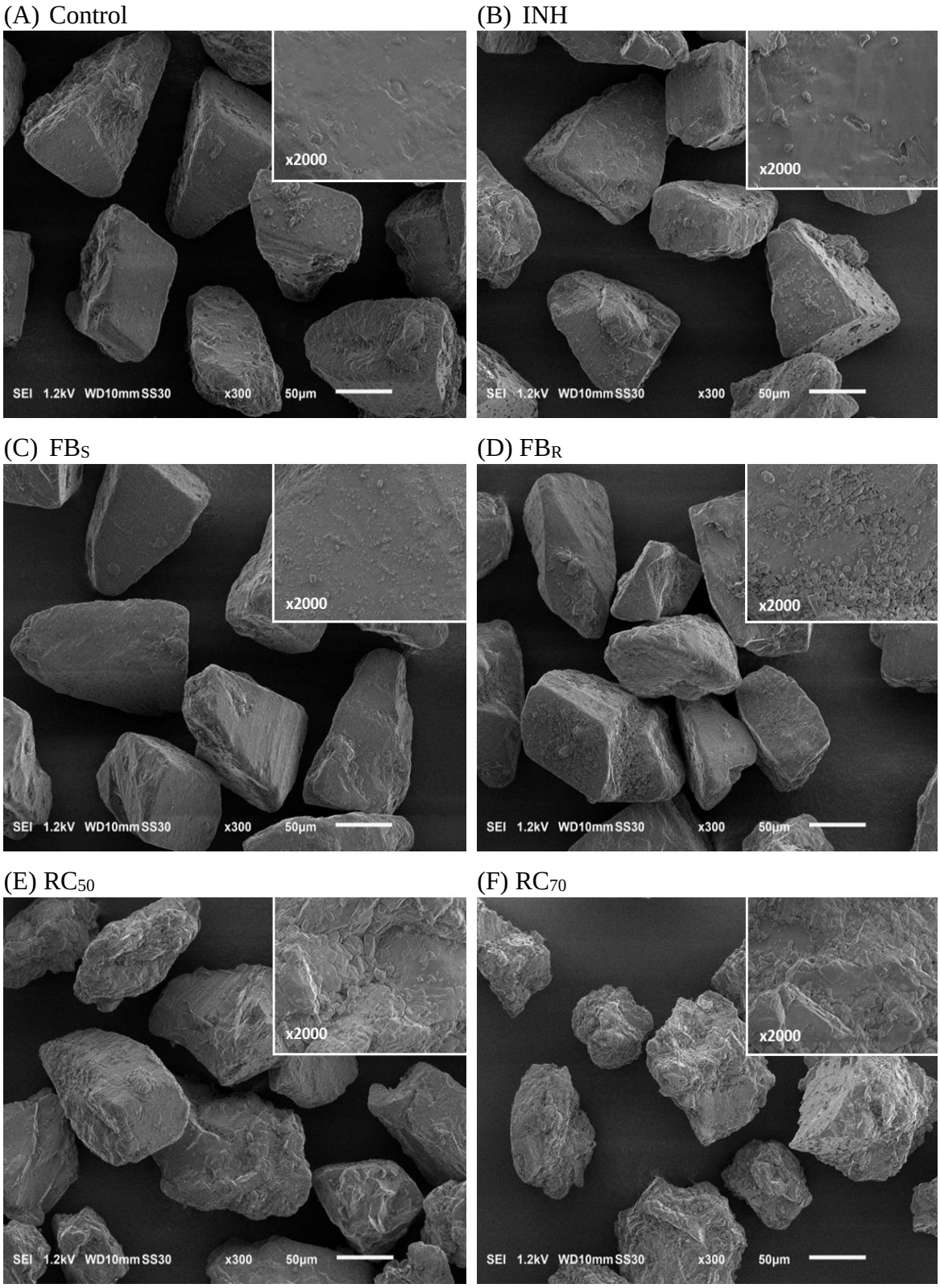

Figure 36. SEM images of lactose particles and their typical surfaces (top right corner) from the (A) Control, (B) INH, (C) FB_S, (D) FB_R, (E) RC_{50}, and (F) RC_{70} carrier batches.

4.3.1.3 Fine particle fractions of dry powder inhaler formulations

4.3.1.3.1 Formulations containing various concentrations of fine lactose

A contour plot (Figure 37) was constructed to illustrate the effects of surface roughness and concentration of fine lactose on the FPF. The effect of carrier roughness appeared to be most significant when the concentration of fine lactose was between 0 – 3 %, w/w. By tracing the contour lines, it was clear that the roughest particles (R_a greater than 1100 nm) had achieved almost the same FPF values (approximately 35 %) in the absence of fine lactose as when 2 %, w/w of fines was added to the smoothest particles (R_a smaller than 800 nm). The FPF of the RC carriers were relatively unaffected by fine lactose concentration as only less than 40 % increase in FPF was observed within the range of 0 – 10 %, w/w of fine lactose. In comparison, the FPF of the control, INH and FB carriers were approximately doubled by the presence of 10 %, w/w of fine lactose. The improvement in FPF with addition of fine lactose has been widely discussed in literature (140-146). The mechanisms by which fine lactose increases FPF are: (a) the saturation of high energy sites (147) and (b) formation of mixed agglomerates of drug and fines (148) which require less detachment and dispersion energy.

Powder cohesion of the DPI formulations with increasing concentrations of fine lactose was determined using shear cell tests (Table 16) in order to investigate whether the FPF was associated with powder flowability. The tests showed that all the DPI formulations containing up to 10 %, w/w of fine lactose could be classified as free-flowing powders since their ff_c were greater than 4. The addition of fine lactose resulted in the decrease of ff_c even though the FPF increased. There were no apparent relationships between the particle size, shape or roughness of the carriers and their flow properties. Powder cohesion did not seem to be directly related to the FPF. This was most apparent in DPI

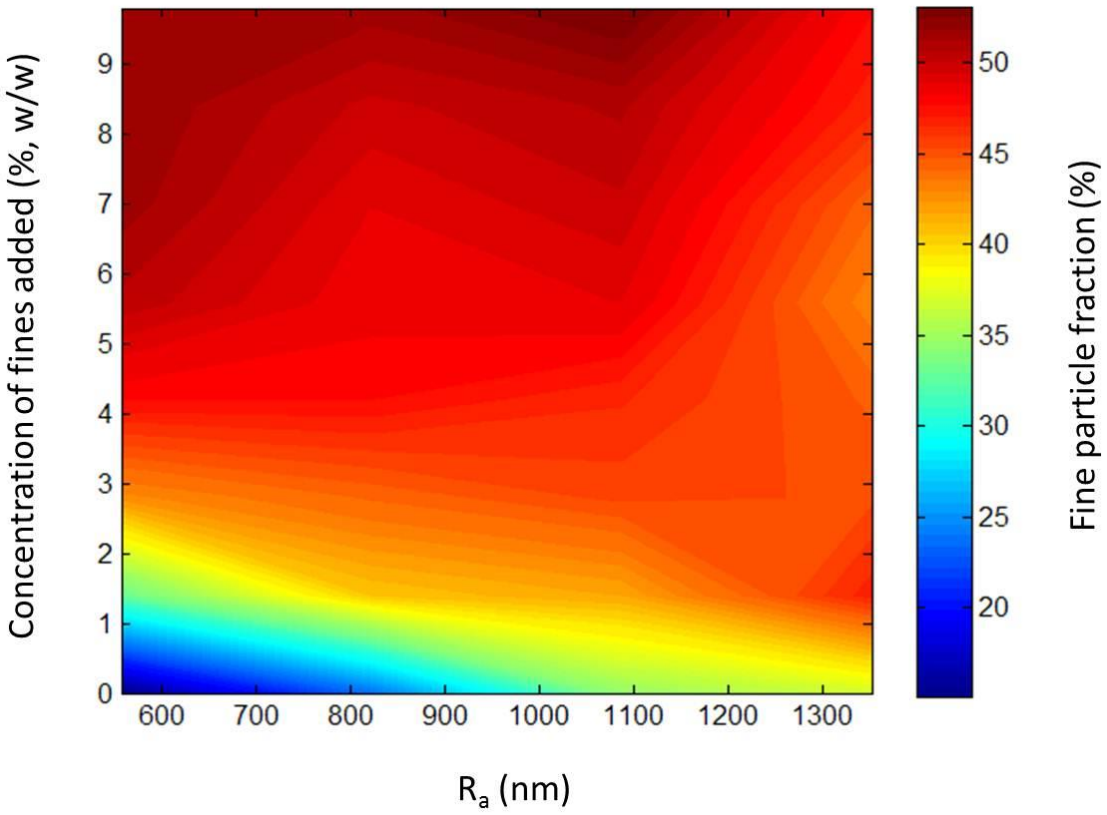

Figure 37. Contour plot showing the relationships among surface roughness, concentration of fine lactose and FPF of the micronized drug. The drug load was kept constant at 2 %, w/w in all experiments.

formulations containing no fine lactose as the RC_{50} carrier showed significantly higher FPF despite having similar ff_c to the control and FB_S carrier. At concentrations of fine lactose less than 7 %, w/w, the ff_c values of the RC carriers were slightly higher than other carriers. As the fine lactose concentration was increased to 10 %, w/w, ff_c values between the different carriers became more similar as powder flow became more dominated by the fine lactose/drug instead of the coarse carriers.

Table 16. Flow function (ff_c) of DPI formulations containing different concentrations of fine lactose

Carrier code	ff_c				
	Concentration of fines added (%, w/w)				
	0	2	4	7	10
Control	7.3 (0.9)	5.6 (0.3)	5.1 (0.0)	4.4 (0.1)	4.2 (0.2)
INH	6.4 (0.3)	5.9 (0.1)	5.5 (0.1)	4.7 (0.3)	4.3 (0.0)
FB_S	7.5 (0.5)	5.8 (0.1)	5.3 (0.3)	4.5 (0.1)	4.0 (0.2)
FB_R	6.8 (0.4)	6.2 (0.3)	5.5 (0.3)	4.9 (0.3)	4.2 (0.4)
RC_{50}	7.4 (0.2)	6.8 (0.0)	6.3 (0.1)	5.0 (0.3)	4.1 (0.2)
RC_{70}	6.4 (0.1)	6.2 (0.3)	5.8 (0.2)	5.1 (0.3)	4.4 (0.2)

Values in parentheses represent the respective standard deviation

4.3.1.3.2 Formulations containing various concentrations of drug

The FPF of formulations containing various concentrations of drug are shown in Table 17. The effects of surface roughness and drug load on the FPF can be seen from the contour plot in Figure 38. Rougher RC carriers performed significantly better than smoother carriers. The FPF values of RC carriers containing 1 %, w/w drug was almost equivalent to the other smoother carriers containing 3 %, w/w of drug. Differences in the FPF values between the different carriers were pronounced when up to 6 %, w/w of drug was added. Comparing these results with those of Figure 37, it is clear that addition of fine lactose had improved the FPF values more efficiently than the increase of drug load. This was because the FPF of all carriers with 6 %, w/w of drug was about 30 – 40 %, which was considerably lower than the maximum FPF (45 – 50 %) that could be achieved by the addition of 10 %, w/w of fine lactose.

Table 17. Fine particle fractions (FPF) of formulations containing various concentrations of micronized drug in the absence of fine lactose

Carrier code	FPF (%)				
	Concentration of drug (%, w/w)				
	0.5	1.0	2.0	4.0	6.0
Control	13.3	22.5	23.5	33.8	29.2
INH	10.7	14.9	19.8	27.4	39.2
FB_S	4.5	10.0	15.1	33.5	31.0
FB_R	7.1	12.9	24.9	29.4	32.7
RC_{50}	35.0	36.4	39.4	41.7	41.6
RC_{70}	21.9	32.2	36.8	39.9	38.8

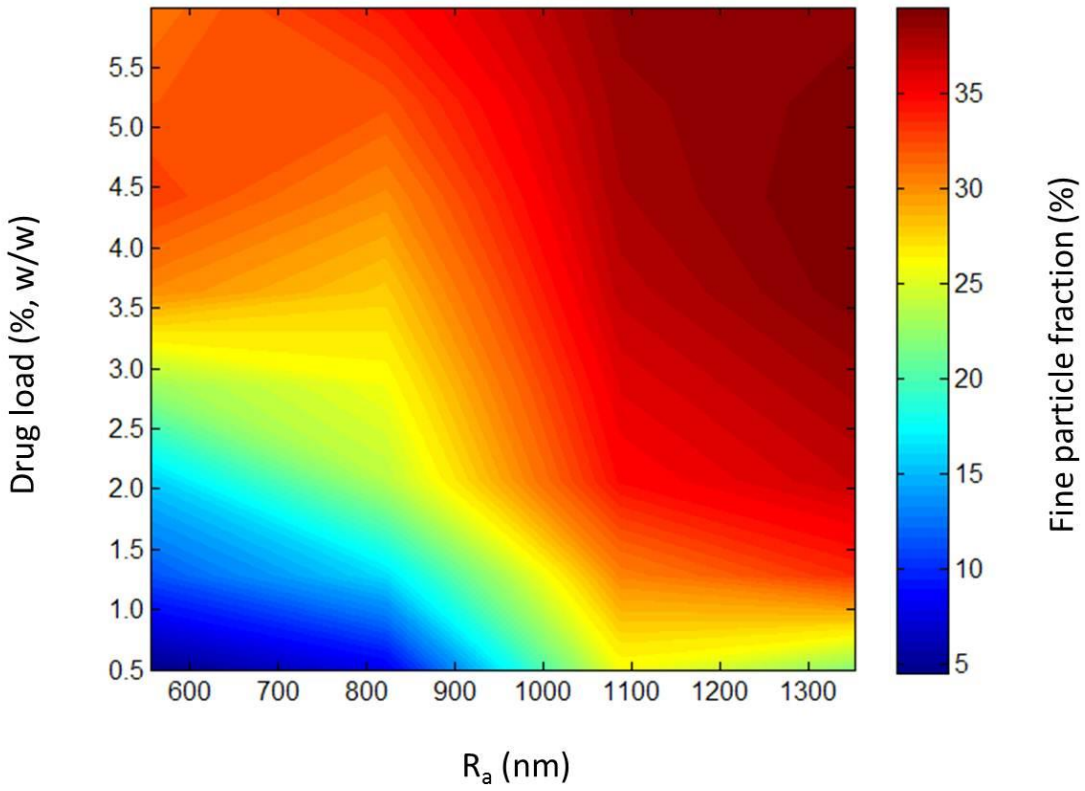

Figure 38. Contour plot showing the relationships among surface roughness, drug load and FPF of the micronized drug. The DPI formulations contained only coarse carriers and drug.

4.3.1.4 Aerodynamic size distributions of deposited drug

The aerodynamic size distribution of a drug, represented by the MMAD and GSD, is useful for assessing the size distribution of drug particles detached from the carrier particles during aerosolization. Although the MMAD should preferably fall within the size range of 1 – 5 µm, it is not always directly related to the FPF since the MMAD is a parameter of size distribution, but not the actual amount, of drug deposited in the NGI. Therefore, the efficiency (FPF) and pattern (MMAD) of drug deposition have been evaluated separately in this discussion. The geometric size distribution of drug particles in the DPI formulation (before aerosolization) showed log-normal distribution (R^2 = 0.96), with median geometric diameter of 2.52 µm and GSD of 1.40. The geometric size of particles was not equal to their aerodynamic size as the drug particles could not be assumed to be perfectly spherical with a density of 1.0 g/cm^3 (124). However, it was assumed that the aerodynamic size distribution of these drug particles would follow a log-normal distribution. After aerosolization of the dose, these drug particles were divided into two major fractions: (a) drug particles detached from carrier particles and deposited in NGI stages and (b) drug particles which remain adhered to the carrier particles and deposited in the pre-separator. The graph in Figure 39 shows that the FPF was linearly related with F_p (R^2 = 0.95), the fraction of drug trapped in the pre-separator. This was strong indication that drug particles which were not deposited in the NGI were likely to remain adhered to carrier particles trapped in the pre-separator. The x-intercept of the best-fit line suggests that all drug particles would be recovered from the pre-separator when the FPF is 0 %. The y-intercept of the same line suggests that even when all the drug particles have completely detached from the carrier particles, a minimum of 30 % of drug would be deposited in the mouthpiece adaptor, induction port and stages 1

and 5 – 8 of the NGI. Hence, the probable maximum FPF that can be achieved in the entire set of DPI formulations used in this study is about 70 %.

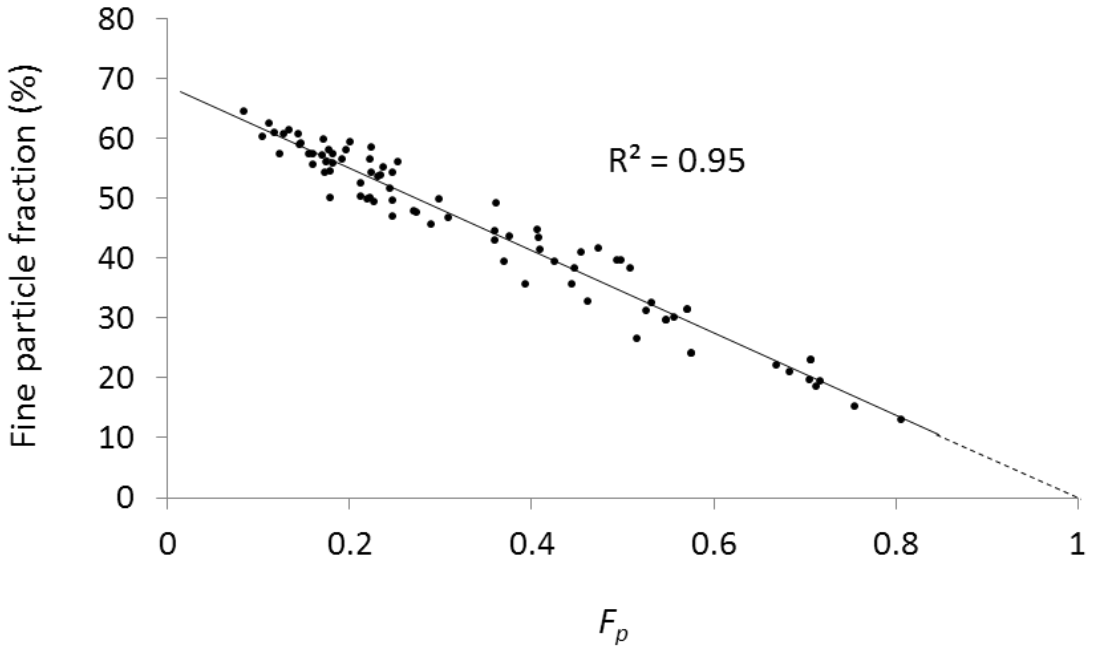

Figure 39. Graph showing linear relationship between FPF and F_p, using data points from all *in vitro* experiments.

The aerodynamic size distribution of drug particles which remain on the carrier particles cannot be directly determined by conventional methods since they cannot be completely recovered in the dry state from the carrier particles. However, changes in this size distribution may be inferred from corresponding shifts in the MMAD. The shifts in the MMAD values were used as indirect measures of the changes in the size distributions of the drug particles remaining on the carrier surfaces after aerosolization. Changes in the MMAD may be attributed to either one of the two factors; (a) changes in the size of drug (or drug-lactose) agglomerates formed in the ordered mixture or (b) preferential adhesion

of smaller-sized (or larger-sized) drug particles to carrier surfaces. To date, few research papers have provided information on the potential differences in the interaction behavior between the carrier surface and drug particles of different sizes. Different-sized drug particles are unlikely to behave in the same way; smaller particles are likely to be more strongly adhering to carrier surfaces due to the shorter distance of separation, stronger van der Waals forces and have higher likelihood of being entrapped in surface crevices than the larger particles. When the degree of surface roughness is increased, however, larger drug particles can also be entrapped in wider surface crevices. By comparing the MMAD values among the carriers with different surface roughness, it was possible to identify if there was preferential adhesion of particles based on their particle size to carrier surfaces of different roughness. Figure 40 is a graphical representation of the concept described above.

4.3.1.4.1 Formulations containing various concentrations of fine lactose

The MMAD values of drug deposited in the NGI were calculated for all DPI formulations (Figure 41). As the fine lactose concentration increased from 0 – 1 %, w/w, there was an initial decrease in the MMAD of deposited drug when the smooth carriers (control, INH and FB_S) were used. The same was not observed for the FB_R and RC carriers as the MMAD remained relatively constant regardless of the fine lactose concentration. Although the FPF values increased by almost 2 – 3 folds when the fine lactose concentration was increased from 1 to 10 %, w/w in the control, INH and FB carriers, the MMAD values did not change (Figures 37 and 41). The results suggest that the increasing concentration of fine lactose had an effect on the drug deposition patterns (i.e., size distributions) only at low fines concentration in the smooth carriers. When the concentration of fines was beyond 1 %, w/w for any carrier or as long as rough RC carriers were used, fine lactose had little effect on the drug deposition patterns.

Interestingly, carrier roughness appeared to exert greater influence on the MMAD as the MMAD of drug using the INH carrier were the lowest while that of the RC_{70} carrier was the highest regardless of the fine lactose concentration. Hence, the MMAD values were more dependent on the carrier type than the fine lactose concentration or FPF.

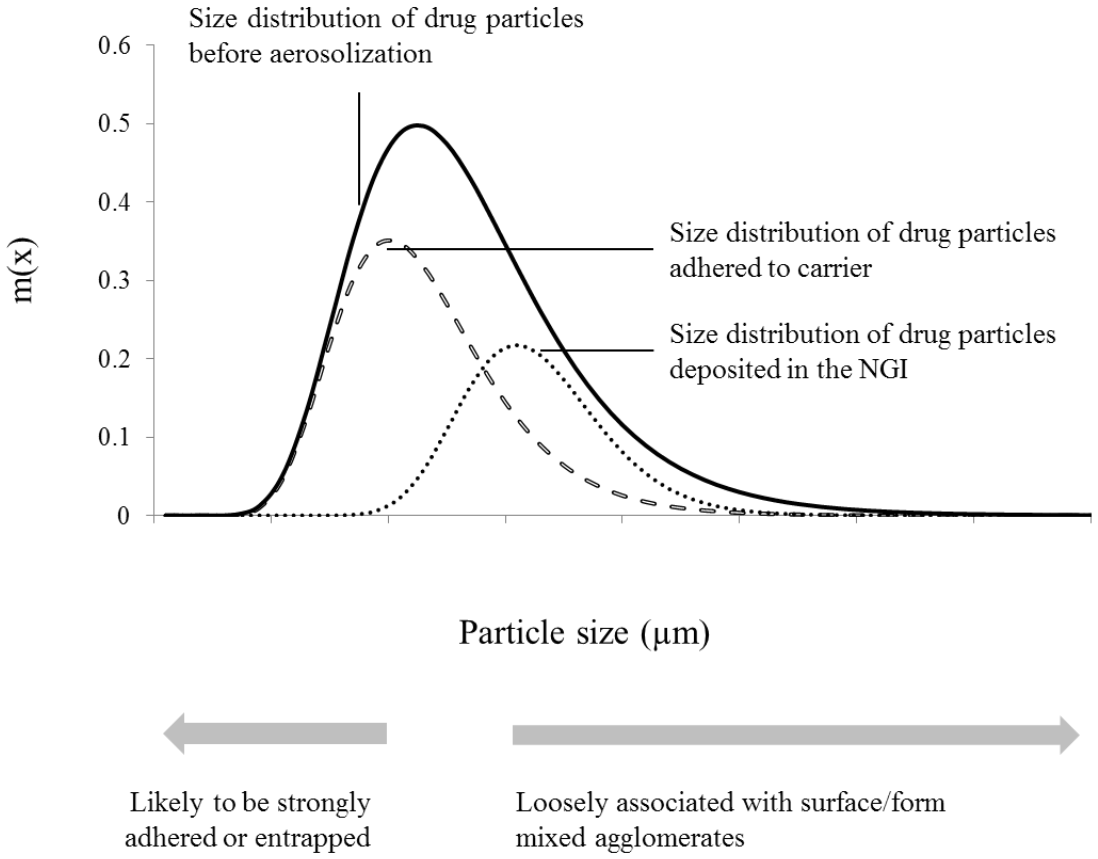

Figure 40. Graph depicting three different possible size distributions of drug particles; in the DPI formulation before aerosolization, deposited in the NGI and adhered on the carrier particles after aerosolization.

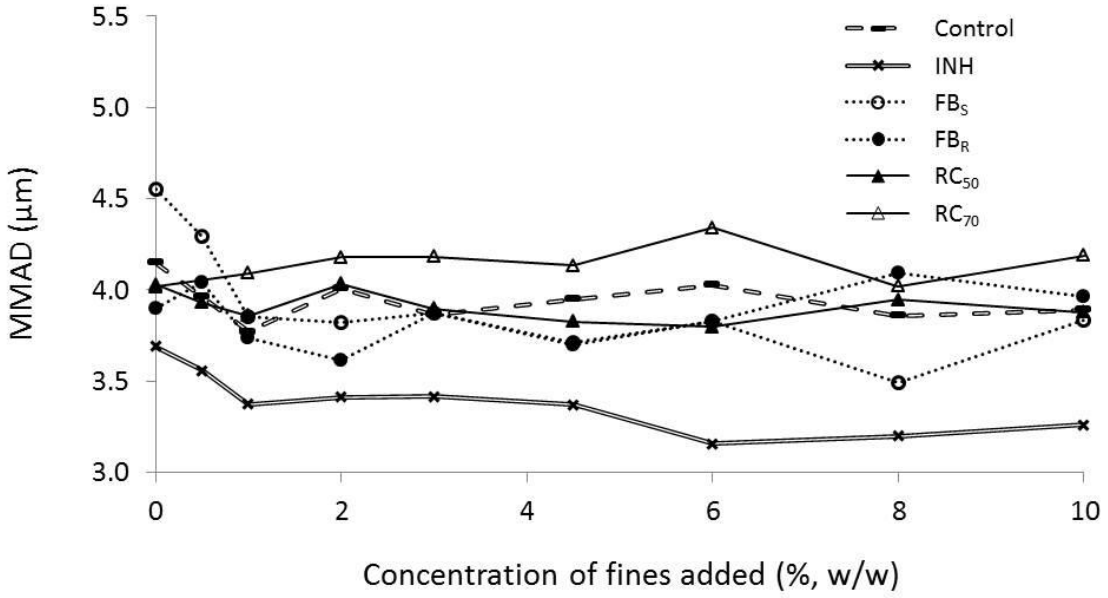

Figure 41. Relationship between MMAD of micronized drug and the concentration of fine lactose added to DPI formulations. The drug load was kept constant at 2 %, w/w in all experiments.

The higher MMAD values of drug in formulations containing rougher carriers may be attributed to increased entrapment of the finest drug particles. The same trend has been observed in another investigation with a similar reasoning being suggested (37). The R_a values from the optical profiler suggest that the magnitude of roughness was in the order of 500 – 3000 nm in the roller compacted particles. Fine particles in the size range in the order of the roughness values would be more easily entrapped on the surface crevices compared to larger particles. It has been suggested that fine lactose particles can physically displace drug particles adhering to active sites on the carrier surface after they have been blended with the carrier and drug particles (137). The fine lactose used in this study had a d_{10} of 2 µm and hence, very low amounts of fine particles were small enough (either comparable or smaller than drug particles) to physically displace the entrapped drug particles. As a result, the differences in MMAD of drug between the formulations

containing different carriers remained relatively constant at all concentrations of fine lactose when the drug load was 2 %, w/w (Figure 41). The presence of up to 10 %, w/w of fine lactose had little effect on reducing the entrapment of finer drug particles and hence, the FPF was not significantly affected. The results suggest a need to reassess the current understanding of drug entrapment on carrier surfaces and its consequences on DPI performance (9, 60). As shown in this study, increased entrapment of drug particles on rougher carrier surfaces was not always detrimental to DPI performance. Rather, considerations about the preferential entrapment of drug particles of comparable size to the magnitude of surface roughness as well as its effects on both the FPF and MMAD also have to be made.

4.3.1.4.2 Formulations containing various concentrations of drug

When the MMAD values were plotted against the drug load for all six types of carriers (Figure 42), the initial decrease of MMAD was observed most significantly for the FB_S, followed by the INH, FB_R and control carrier. The decrease in MMAD of drug was much reduced in the RC_{50} carrier and not observed in the RC_{70} carrier. With a simultaneous decrease of the MMAD and increase of FPF when the drug load was increased from 0.5 to 1 %, w/w, two conclusions could be drawn about drug adhesion to the carrier at a lower drug load of 0.5 %, w/w (Figures 38 and 42). The lower FPF value could be attributed to stronger adhesion of drug particles to the carrier at lower drug loads. More specifically, the finer drug particles may have been more strongly adhered to the carrier than the larger drug particles since the MMAD was higher when the drug load was 0.5 %, w/w. Changes in the MMAD values were no longer observed when drug loads were further increased to greater than 2 – 4 %, w/w. As the drug load increased beyond 2 %, w/w, the differences in MMAD of drug among all the carriers became much reduced. The trend was different from that shown in Figure 41, where differences in MMAD

between the carriers could be observed even at the highest concentration of fine lactose. This finding suggests that surface roughness of the carrier had decreasing influence on the drug deposition patterns when the availability of drug particles was increased relative to the available carrier surface.

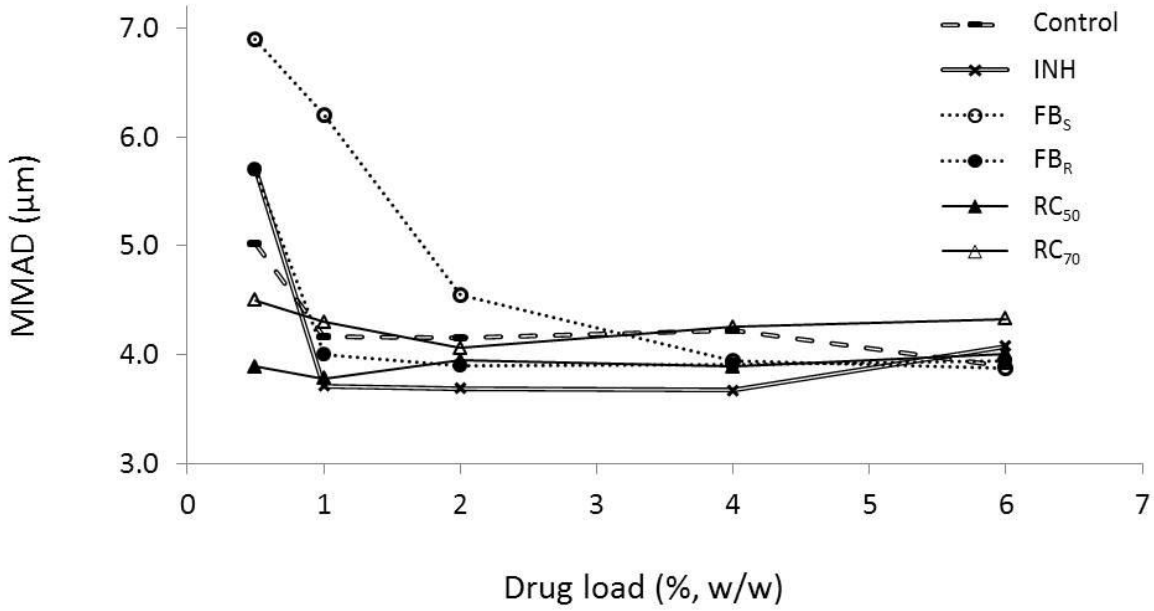

Figure 42. Relationship between MMAD of micronized drug and the drug load in the DPI formulations. The DPI formulations contained only coarse carriers and drug.

4.3.1.5 Strategies to improve fine particle fraction

Favorable spatial conditions of drug particles in the ordered mixture should be established in the formulation and/or blending stages in order to improve DPI performance. This in turn depends on the surface properties of the carrier. For smoother carriers, the formation of lactose-drug agglomerates by incorporation of fine lactose is an

effective strategy. For rougher carriers, limited effect on the FPF was observed with the addition of fine lactose. Roughening of carrier lactose can allow a greater degree of separation of drug particles on carrier surfaces and smaller/weaker drug agglomerates. It was noted in this study that the MMAD of drug from the RC_{70} carrier formulation were greater than 4 µm in most experiments and this is not ideal considering that the aerodynamic size range requirement for optimal drug deposition in the lung is 1 – 5 µm. The MMAD of drug when smoother carriers were used were generally smaller than 4 µm and the lowest range of 3.2 – 3.4 µm was achieved with the INH carrier. Hence, it is likely that a slight decrease in the particle size of the drug (to decrease its aerodynamic diameter) may be required for rougher carriers compared to the smoother ones.

It has also been reported that only the very small lactose particles that can be co-deposited with the drug were useful in improving DPI performance (149) and strong linear relationships between FPF and fraction of fine lactose less than 10 µm have been observed (141). Based on the results of this study, lactose of very small size (preferably close to the size of drug particles) should be used with rougher carriers in order for them to displace the drug particles entrapped on the surfaces more efficiently. Collectively, these strategies are aimed at reducing the energy requirement for dispersion of drug agglomerates during aerosolization. Thus, it is likely that the size requirement of both the drug and fine lactose for maximal DPI performance may vary with the nature of the carrier surfaces among others.

4.3.2 Part 3B: Investigation of the surface distribution of micronized drug particles on rough lactose carriers using Raman spectroscopy

4.3.2.1 Raman spectrum of α-lactose monohydrate

The Raman spectrum of α-lactose monohydrate is shown in Figure 43. Lactose was shown to exhibit auto-fluorescence since the baseline of the raw spectrum was elevated from around 200 – 1800 cm^{-1} and increased gradually beyond 1800 cm^{-1}. Intense and well-defined peaks occurred at 1080 cm^{-1} and in the region of 2800 – 3000 cm^{-1}. The peak at 1080 cm^{-1} was reported to be characteristic of bending and stretching vibrations of the bridge COC group (150, 151) in the lactose molecule. By applying a baseline correction to the raw spectrum, the fluorescence background could be suppressed.

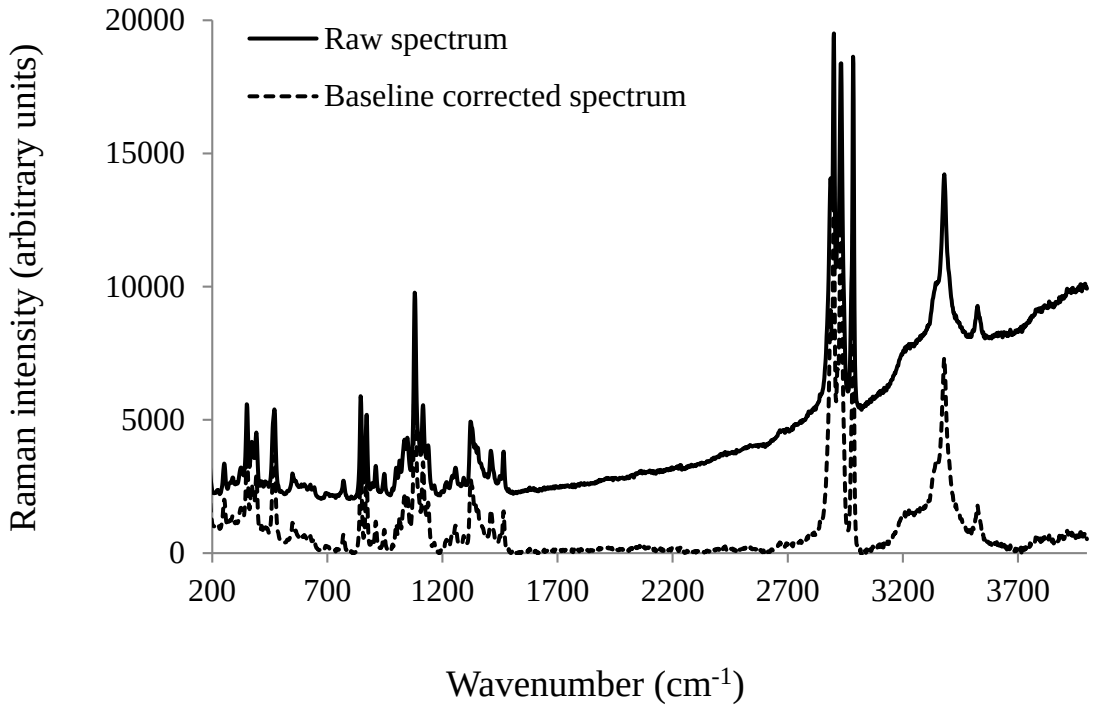

Figure 43. Raw and baseline-corrected spectra of α-lactose monohydrate.

4.3.2.2 Raman spectra of drugs

The raw Raman spectra of all drugs used are shown in Figure 44. Since the intensity of the Raman signals were dependent on how well the sample was focused, the spectra were all taken at the point of maximum focus of each sample. The intensities of the Raman peaks were highest at the point of maximum focus and this was achieved by slowly adjusting the stage while observing the real-time spectrum until the strongest signals were obtained. Hence, direct comparisons of the Raman signal intensities were possible and this helped in the selection of the model drug to use. Drugs with higher Raman scattering intensities were more desirable as there is a greater confidence of detection of the drug especially when the drug is present in very low concentrations in the interactive mixtures. Baseline correction was not applied to the spectra in order to compare the fluorescence effect of each drug, relative to the intensities of its Raman signals.

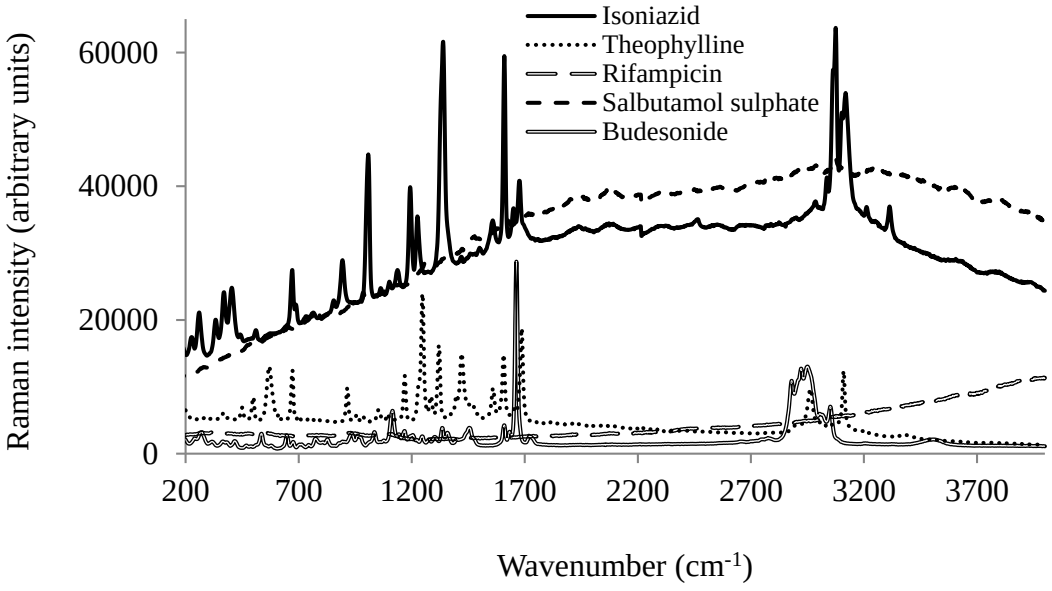

Figure 44. Raman spectra of drugs in the spectral range of 200 – 4000 cm^{-1}.

It can be clearly seen that the scattering intensities of salbutamol sulphate and rifampicin were very weak compared to the other compounds. Therefore, they were not very suitable as drug markers for this work. The scattering intensities of theophylline were slightly weaker than that of isoniazid or budesonide. Isoniazid showed a stronger fluorescent background compared to theophylline and budesonide. The spectral region of 200 – 2000 cm^{-1} was found to contain the majority of the useful information needed, in the form of intense and sharp peaks, for isoniazid, budesonide and theophylline.

The spectra of the three selected drugs and that of lactose were compared within the range of 200 – 2000 cm^{-1} and are presented in Figure 45. The purpose of this was to determine the feasibility of using univariate analysis to identify the presence of lactose and/or drug when given any spectrum obtained from an interactive mixture comprising only the lactose carrier and the drug. The most important criterion for univariate analysis is the presence of a distinct and non-overlapping peak in the drug spectrum, when compared against that of lactose. As the intensity of the Raman signal at each wavenumber is directly proportional to the number of molecules in the sample volume, the absolute peak intensity/area can theoretically be used to determine the amount of sample present. In reality, however, the absolute intensities of Raman signals are seldom useful without complex pre-processing of the spectra to separate the signals from noise (128). This is because the signal intensities are dependent on a multitude of factors such as random fluctuations and instrument noise. The correct setting of focus at each scan spot was also found to influence the intensities significantly. Instead of the absolute amount of drug at each scan spot, the concentration ratio of drug and lactose provides more reflective quantitative information for the purposes of this work.

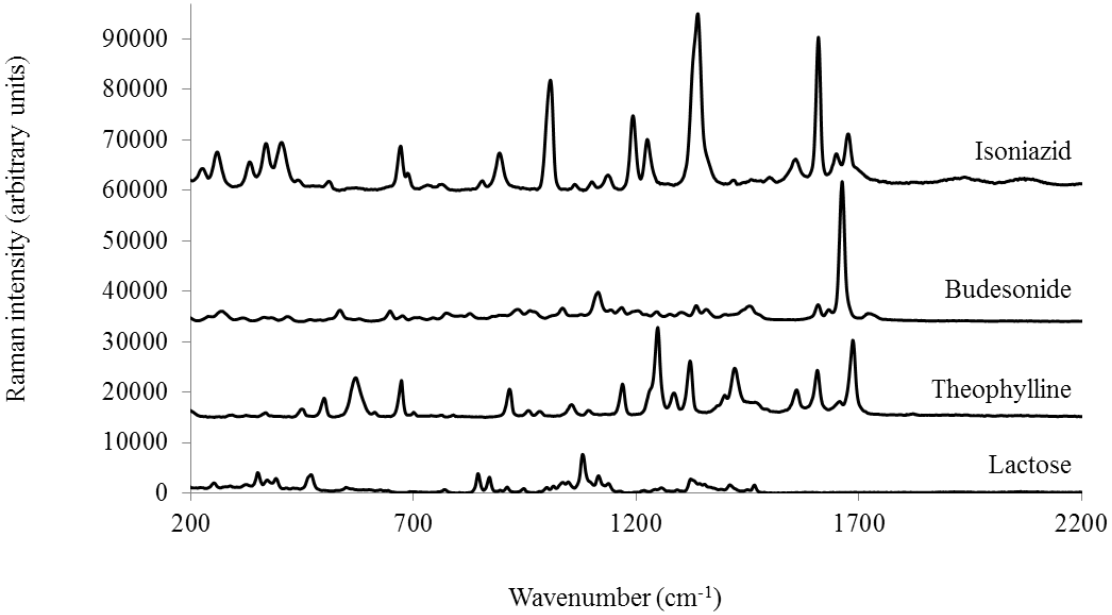

Figure 45. Comparison of the Raman spectra of lactose and three drugs (isoniazid, budesonide and theophylline) for assessment of suitability for use in Raman spectral mapping.

From Figure 45, it can be seen that the Raman spectral features of lactose are concentrated in the region of 200 – 1450 cm^{-1}. To minimize the effect of overlapping peaks, the spectral region beyond 1500 cm^{-1} was most ideal for selection of comparative peaks in the drug spectra. There was at least one intense peak located in this region in each drug spectrum: at 1604 cm^{-1} for isoniazid, 1663 cm^{-1} for budesonide and 1689 cm^{-1} for theophylline. The absolute peak intensity at 1689 cm^{-1} for theophylline was the lowest while the peak intensities in the spectra of isoniazid and budesonide at 1604 cm^{-1} and 1663 cm^{-1}, respectively, were of similar magnitude. Hence, either isoniazid or budesonide could be used as drug markers for Raman spectral mapping of the DPI formulations. Isoniazid was chosen as the drug in subsequent studies since it had slightly higher peak intensity at 1604 cm^{-1} and was used previously in the *in vitro* NGI studies. The peak at Raman shift of 1080 cm^{-1} in the lactose spectrum did not overlap with any

peak in the isoniazid spectrum and was therefore chosen for relative quantification purposes.

4.3.2.3 Ratio of peak intensities in lactose and isoniazid

The spread of the $Peak_{1080/1604}$ values (Page 79) for both lactose and isoniazid are shown Figure 46. It can be seen that the values were approximately normally distributed over 2000 spectra. For lactose, the mean $Peak_{1080/1604}$ value and standard deviation were 13.9 ± 3.3 while that of isoniazid were 0.047 ± 0.008. By assuming normal distribution of $Peak_{1080/1604}$ and calculating for 2 standard deviations on either side of the mean values, there was a 98 % chance that $Peak_{1080/1604}$ would be: (a) greater than 7.21 if lactose alone was present and (b) smaller than 0.063 if isoniazid alone was present on the scan spot. Therefore, the threshold range of 0.083 – 5.9 (Page 80) meant that the probability of falsely detecting isoniazid in any scan spot would be much lower than 2 %.

4.3.2.4 Effect of mapping parameters and mixture composition on Raman images

The important considerations in the construction of Raman chemical images from interactive DPI mixtures are summarized in Figure 47. The variable factors in this study include the concentration of drug, step size and scan length. The particle size of drug and coarse carrier, blend uniformity and laser spot size were taken to be fixed variables. The long duration of time for data acquisition and processing was the major limiting factor for Raman spectral mapping. The average time for spectra acquisition in a 20 × 20 grid array typically took about 30 – 40 min. The time was inclusive of the exposure time for spectra acquisition and stage movement and settling time. This had posed a limit to the number of images that could be generated for the study.

(A)

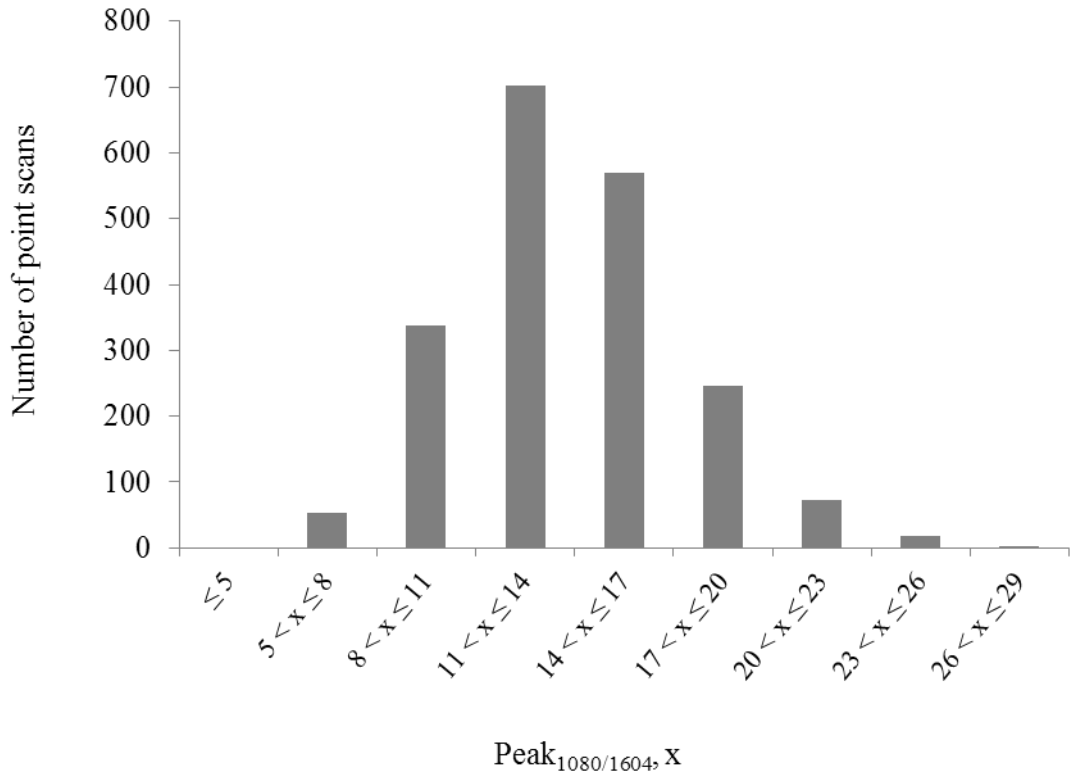

(B)

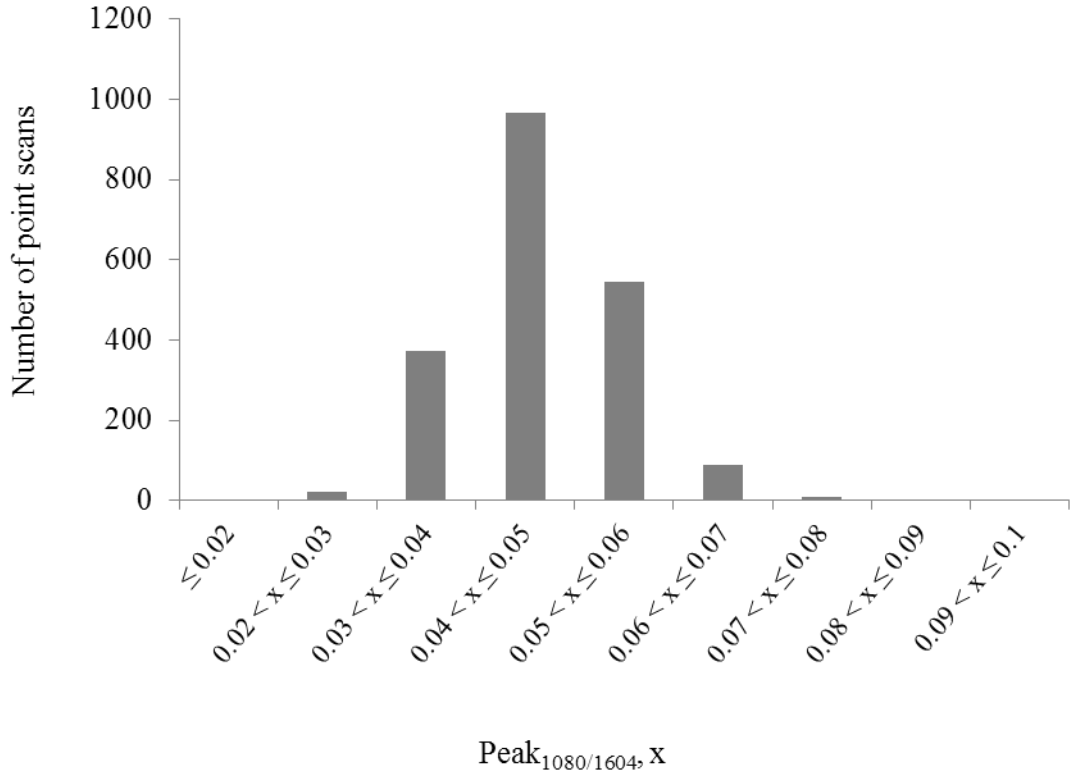

Figure 46. Histograms showing the spread of ratios of the peak intensity at 1080 cm^{-1} to the peak intensity at 1604 cm^{-1} when 2000 points scans were conducted on (A) lactose and (B) isoniazid.

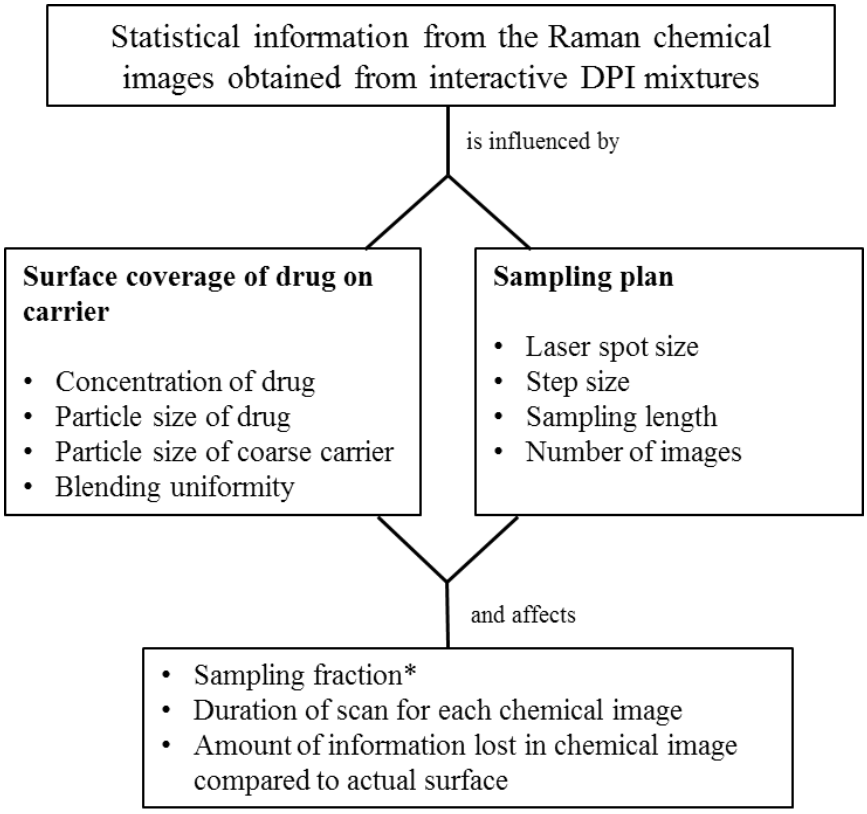

Figure 47. Chart showing the important considerations for obtaining Raman chemical images from interactive DPI mixtures containing micronized drug and coarse carrier.

4.3.2.4.1 Sampling step size and scan length

A total of four different mapping experiments were performed on various sampling step sizes, scan lengths and drug concentrations in the interactive mixtures. The purpose of this was to determine the type of visual/statistical information that can be provided by Raman spectral analysis under these various conditions. This is because the scan spot of the laser is extremely small, in the order of a few µm, compared to the typical area for analysis (hundreds of µm to the mm range). The Raman maps were constructed using either the step size of 5 µm and sampling length of 100 µm or the step size of 20 µm and

sampling length of 400 µm. The Raman maps were constructed using the SS of the scan spots and are presented in Figures 48 and 49. A map obtained using a scan length of 100 µm captured only one particle surface while a scan length of 400 µm captured approximately 10 – 20 particles in the scan area. The use of 20 µm step size resulted in the loss of more information in between each scan point compared to the 5 µm step size. Hence, it can clearly be seen that the maps obtained using the step size of 5 µm provided more visual information regarding the distribution of drug on the surface of each carrier particle. The step size of 20 µm provided more useful statistical information about the distribution of drug particles across different particle surfaces. Based on visual analysis, the drug particles appeared to be well distributed over all carrier particles as the location of grid points containing isoniazid was random in most areas of the entire map (Figure 48). In comparison, more non-uniformity in the distribution of particles was observed when the scale of observation was reduced to individual particle surfaces (Figure 49). The drug particles appeared to be present as agglomerates with widely varying sizes, in the order of tens of µm. It is also apparent from Figure 49 that the surface coverage of drug on the carrier may be calculated based on the total percentages of grid points containing drug. In other studies, surface coverage of micronized drug particles on spherical glass beads has been calculated by assuming a monolayer of spherical drug particles with the densest packing on the bead surfaces (152). Unlike Raman chemical imaging, these calculations do not usually take into consideration the variation of drug particle size, the non-homogeneity of the surface as well as formation of drug agglomerates.

(A)

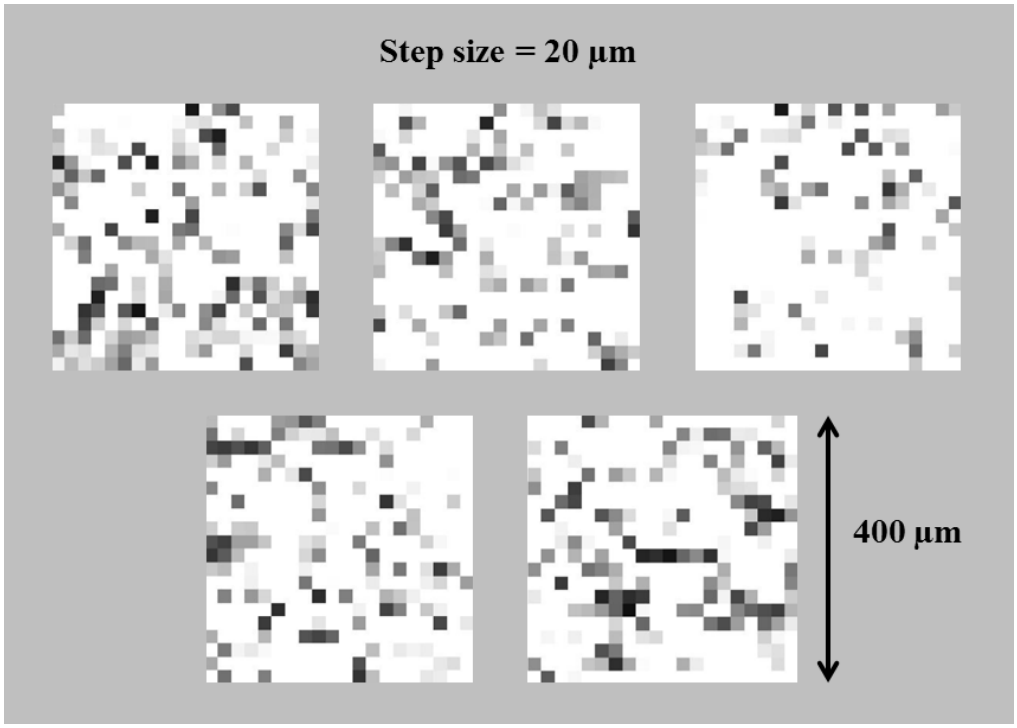

(B)

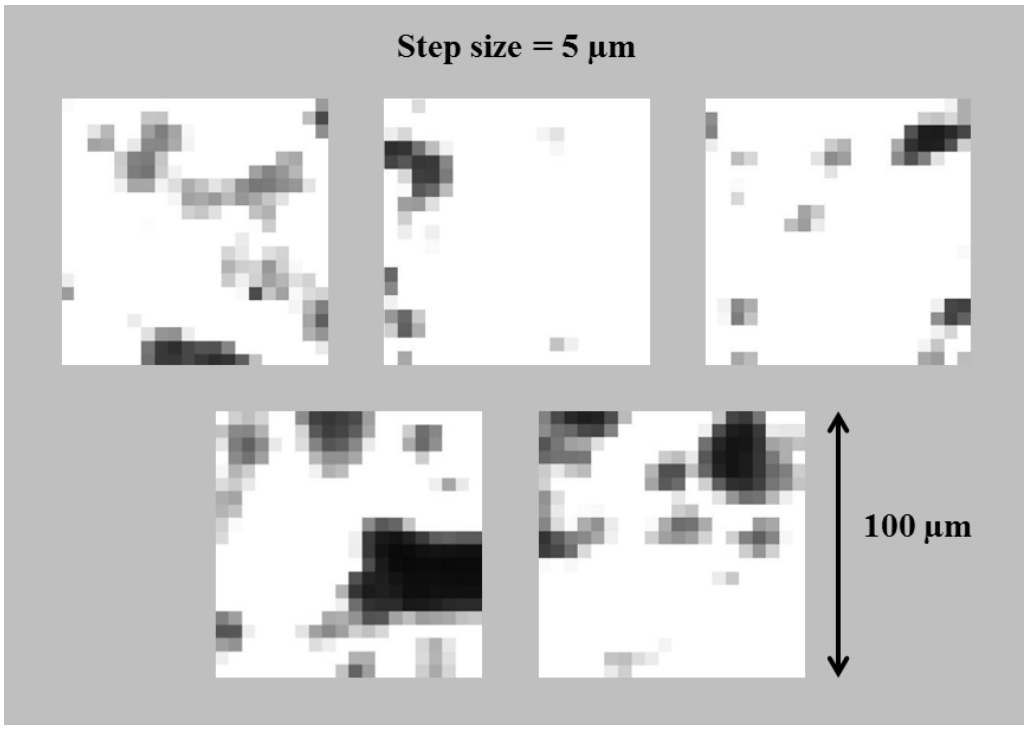

Figure 48. Raman maps constructed when the following mapping conditions were used: (A) step size = 20 µm and scan length = 400 µm and (B) step size = 5 µm and scan length = 100 µm. The sample comprised 1.5 %, w/w of micronized isoniazid in lactose carrier particles. White grid points represent the scan spots where only lactose was detected while gray/black grid points indicate the presence of isoniazid.

(A)

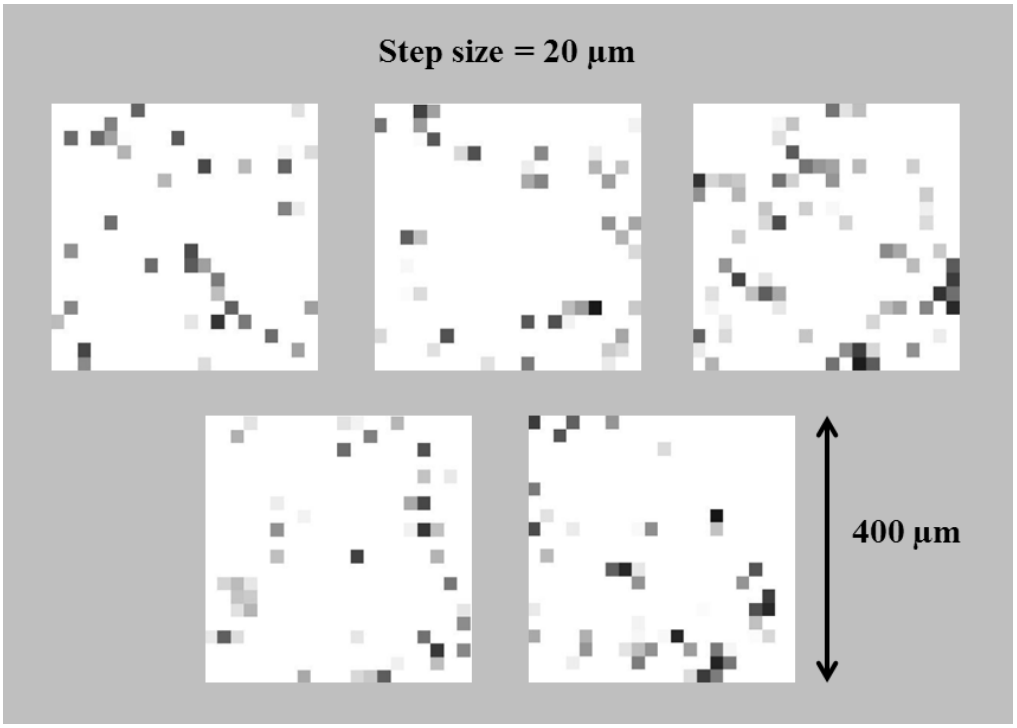

(B)

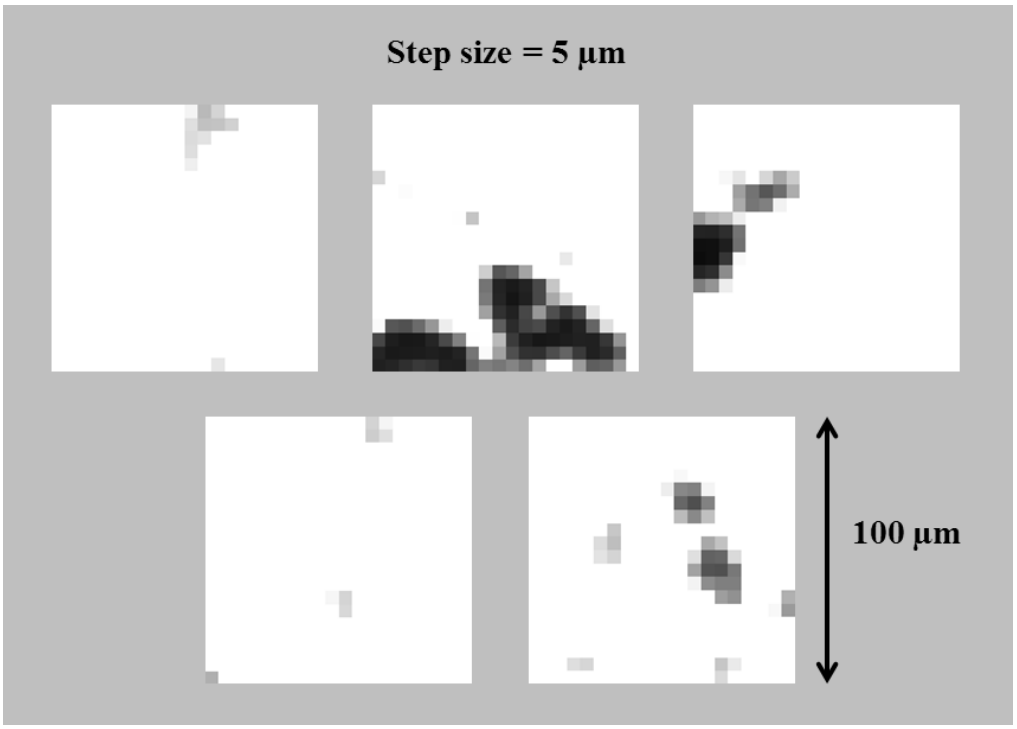

Figure 49. Raman maps constructed when the following mapping conditions were used: (A) step size = 20 µm and scan length = 400 µm and (B) step size = 5 µm and scan length = 100 µm. The sample comprised 0.75 %, w/w of micronized isoniazid in lactose carrier particles. White grid points represent the scan spots where only lactose was detected while gray/black grid points indicate the presence of isoniazid.

4.3.2.4.2 Concentration of micronized drug

In addition to visual information provided by the Raman maps, the distribution of SS was analyzed by the use of histogram plots in Figure 50 and statistical measures were also calculated from them (Table 18). For the histogram plots, the grid points in each of the five Raman maps were combined and thus there were 2000 scan points in total for each combination of step size, sampling length and isoniazid concentration. The greatest number of grid points usually occurred when SS was between 0 – 0.1 (i.e., very low amount of isoniazid detected). This value decreased as the SS increased (i.e., when more isoniazid was detected). An exception, however, was observed in the Raman maps of the mixture containing 0.75 %, w/w isoniazid that were obtained using the 5 µm step size. The numbers of grid points were relatively similar across the entire range of SS.

The number of grid points within each range of SS was approximately halved when the concentration of isoniazid was also halved. This was observed only when the step size was larger (i.e., 20 µm). This observation suggests that the number of grid points containing isoniazid could possibly be used as a statistical measure of the concentration of isoniazid in these interactive mixtures. In contrast, the same inferences could not be drawn from the SS obtained using a smaller step size of 5 µm. One possible reason for this is because the relationship between the number of grid points containing isoniazid and the concentration of isoniazid were more varied across the different ranges of SS.

The results in Table 18 show the mean percentages of grid points containing isoniazid of five Raman maps in each set of conditions and their coefficients of variation. The results suggest that considerable uniformity of distribution of isoniazid particles had occurred when the particles are observed at the length scale of 400 µm (i.e., 10 – 20 particles).

(A)

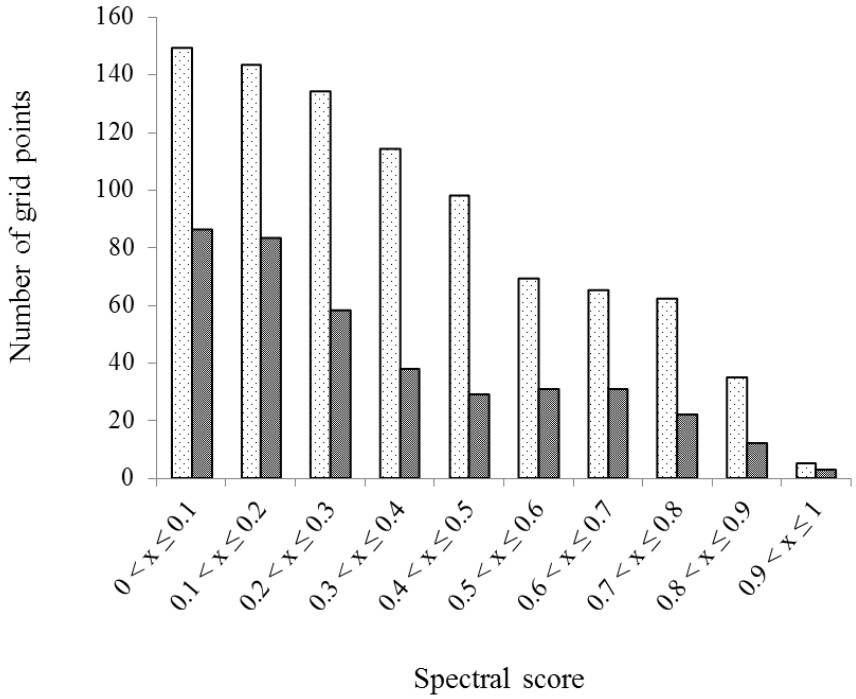

(B)

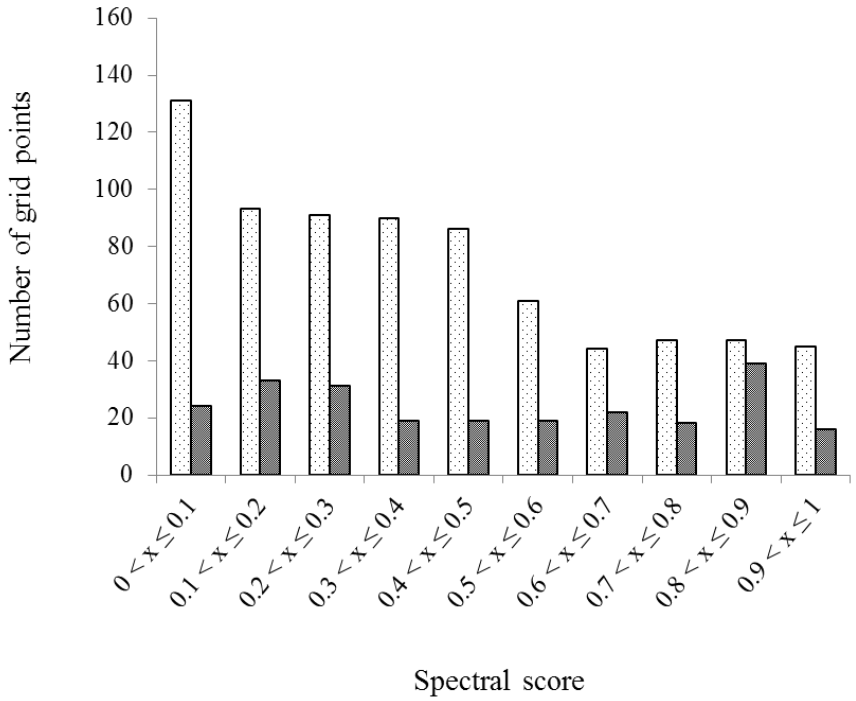

Figure 50. Histograms showing the spectral scores (SS) of the Raman maps obtained by scanning the samples, containing 1.5 %, w/w (⊡) and 0.75 %, w/w (▩) isoniazid, using the step size of (A) 20 µm and (B) 5 µm. The sampling length was 400 µm in (A) and 100 µm in (B).

Table 18. Percentage of grid points containing isoniazid in the Raman maps of lactose and isoniazid mixtures

Concentration of isoniazid (%, w/w)	No. of grid points containing isoniazid	
	Step size (μm)	
	5	20
0.75	11.9 (42.8)	19.9 (9.0)
1.50	36.6 (21.6)	43.4 (3.4)

Values in parenthesis represent the coefficient of variation (%) of the mean number of grid points containing isoniazid (n = 5)

This was because the coefficients of variation obtained when the step size of 20 μm were used were shown to be relatively small (i.e., lower than 10 %) among different Raman maps of the same sample. On the other hand, they were much larger when the step size of 5 μm was used. This indicates that isoniazid particles were not uniformly distributed when carrier particles were observed at the length scale of 100 μm (i.e. about 1 particle). For the same step size employed, the coefficients of variation were found to be greater when the concentration of isoniazid was lower. This was likely related to the lower probability of detecting isoniazid in any one grid point when Raman maps were obtained. The smaller the concentration of isoniazid, the larger the number of scans required to establish the same degree of statistical confidence from the results. Hence, the choice of sampling strategies was shown to influence (a) the distributions of SS and (b) the way the Raman maps should be interpreted with respect to the scale of observation and the drug concentration.

4.3.2.5 Qualitative assessments of drug distribution on carrier surfaces

Visual information about the surface distribution of drug agglomerates/particles on carrier surfaces was first assessed from SEM images. Typical images of the INH and

RC_{70} carriers, which were blended with 2 %, w/w drug, are shown in Figure 51. In general, drug particles were preferentially packed into the surface crevices rather than on the smoother surfaces of the INH carrier particles. For the RC_{70} carrier, however, surface crevices present all around the particles presented as potential sites for drug particles to be deposited in. However, the drug particles could not be as easily distinguished from the lactose particle fragments or protuberances which were also present on the surfaces of the RC_{70} carrier particles. Thus, the SEM was not a discriminating tool to assess the drug distribution on carrier surfaces, especially for the roller compacted carrier particles.

From the SEM images, it can be seen that the information in a 2D chemical image may not be quantitatively accurate in terms of area estimation. This is because the carrier surfaces are rarely flat with respect to the horizontal plane for scanning. Furthermore, the surface areas covered by the scan spots were much smaller than the total carrier surface considered. This led to additional variability in the area parameters calculated from the Raman image maps. Thus, visual information from SEM images would also serve as complimentary information to the chemical images in terms of the topological landscape of the scanned surfaces.

4.3.2.6 Raman mapping of dry powder inhaler formulations

4.3.2.6.1 Interactive mixtures containing various concentrations of fine lactose

In order to investigate the influence of fine lactose content on the distribution of drug particles over the carrier surface, Raman maps were obtained from ternary mixtures comprising the carrier particles, drug and fine lactose. The results are summarized in Table 19. The percentage of isoniazid on the images represented the degree of distribution of drug over the carrier surface. As each Raman map is a 2D chemical image

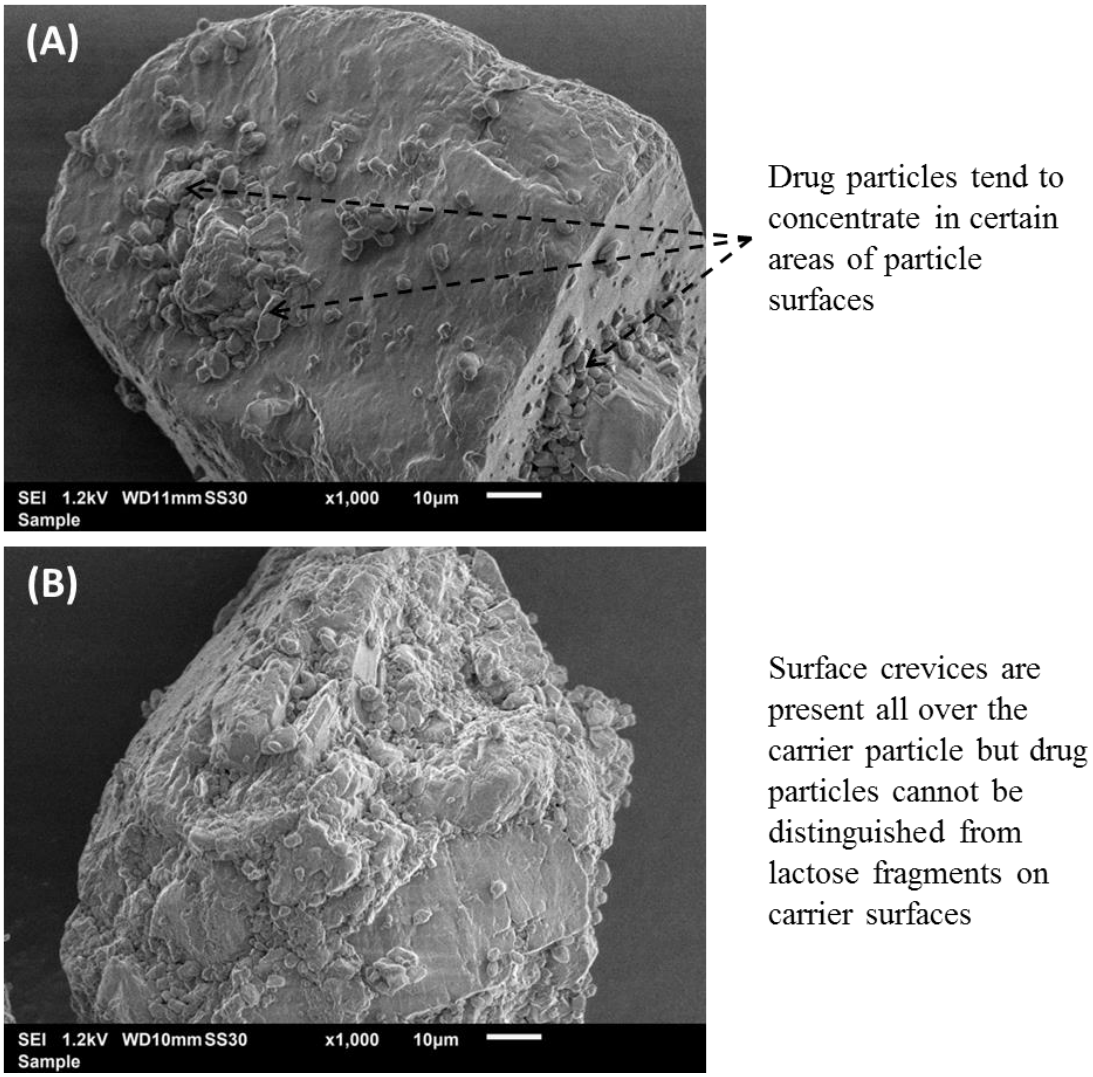

Figure 51. SEM images of a carrier particle in DPI interactive mixtures comprising 2 %, w/w drug in (A) the INH carrier and in (B) the RC_{70} carrier.

of the carrier surface, agglomerated drug particles would be expected to occupy a smaller total surface area on the carrier than dispersed drug particles. Surprisingly, the mean areas of the Raman maps occupied by isoniazid were generally similar and fell within the range of 42 – 46 % ($p = 0.92$). The increase in the percentage of fine lactose in the interactive mixtures did not appear to result in detectable differences in the Raman maps. In these three formulations, however, the drug content remained constant (2 %, w/w) but the actual content of coarse lactose carrier was decreased as the amount of fine

lactose increased. It has been suggested in the literature by other researchers (5) that the drug load in a DPI formulation should not only be considered in terms of its mass percentage in the formulation but also in terms of the surface area ratio of drug to the carrier. Assuming that the available carrier surface area for distribution of drug particles is proportional to the mass percentage of coarse carrier, an approximately 8.2 % decrease in carrier surface area was incurred when 8 %, w/w fine lactose was introduced into the interactive mixture while the drug-lactose ratio was kept constant. The increase in the average % isoniazid on the images was only about 4 %, suggesting that a fraction of drug particles were not adhering directly to the carrier surfaces. The fine lactose may also have shielded the drug particles, causing the reduced presence of drug when the Raman maps were constructed. The % isoniazid on the images might have been confounded by the formation of mixed agglomerates of drug-fine lactose. As the fine lactose content increased, mixed agglomerates may not be strongly adhered to the coarse carrier surfaces. Instead, a loose structure comprising mixed agglomerates interspersed between the individual coarse carrier particles may be formed.

4.3.2.6.2 Interactive mixtures containing carriers of different roughness

The Raman maps were further obtained from binary mixtures of drug and coarse carriers only and the results are shown in Table 20. A more significant change in the % isoniazid on the images were observed with varying surface roughness of the particles. The percentage area of the Raman maps occupied by isoniazid was generally found to be slightly higher (54 – 60 %) for the rougher carriers. However, an exception was observed in the FB_R carrier. Although the FB_R carrier had an intermediate roughness of 907 nm, the % isoniazid on the Raman image was comparable to the rougher RC carriers. The variability of the percentage areas were higher (i.e., greater than 40 %) in the interactive mixtures containing the FB_S and control carriers.

Table 19. Percentage of lactose carrier surfaces occupied by isoniazid particles, calculated from the Raman maps of mixtures containing different fine lactose contents

Interactive mixture used	Map no.	Total no. of grid points with isoniazid	% isoniazid on image
98 %, w/w INH carrier 2 %, w/w isoniazid	1	123	31
	2	44	11
	3	232	58
	4	192	48
	5	62	16
	6	321	80
	7	292	73
	8	119	30
	9	98	25
	10	215	54
	Average	170	42
96 %, w/w INH carrier 2 %, w/w isoniazid 2 %, w/w fine lactose	1	48	12
	2	256	64
	3	74	19
	4	109	27
	5	143	36
	6	258	65
	7	268	67
	8	270	68
	9	163	41
	10	95	24
	Average	168	42
90 %, w/w INH carrier 2 %, w/w isoniazid 8 %, w/w fine lactose	1	211	53
	2	184	46
	3	78	20
	4	226	57
	5	241	60
	6	96	24
	7	130	33
	8	204	51
	9	265	66
	10	185	46
	Average	182	46

Table 20. Percentages of lactose carrier surfaces occupied by isoniazid, calculated from the Raman maps of mixtures containing carriers of various surface roughness

Carrier code*	R_a (nm)	Total no. of grid points with isoniazid	No. of maps**	% isoniazid on maps	RSD (%)
FB_S	557	779	5	39	62
Control	562	951	5	48	41
INH	573	1698	10	42	23
FB_R	907	1199	5	60	20
RC_{50}	1175	1208	5	60	16
RC_{70}	1355	1082	5	54	19

*The interactive mixtures used were binary mixtures of 2 %, w/w isoniazid and 98 %, w/w coarse lactose carrier

**Each Raman map was composed of 400 scan spots

Figure 52 suggests a positive relationship between the % isoniazid on image and the FPF. However, the mixture containing the FB_R carrier was also observed to deviate from the general trend. The trend of increasing % isoniazid on the image with increasing carrier roughness suggests that some differences in the structure of the interactive mixture may be present when rougher carrier particles are used. This was likely to be related to the more regular distribution of surfaces crevices where drug particles can be distributed to. Rougher carrier surfaces might have assisted in the breakdown of drug agglomerates into smaller agglomerates/individual particles during the mixing process due to increased frictional forces. This might have reduced the energy requirements for dispersion of drug agglomerates and increase the FPF. On the other hand, smooth carriers contain relatively fewer surface crevices and drug is distributed over a smaller surface area. Some researchers have reported that rougher carriers contain more binding sites for drug particles since they have greater surface area (152, 153). An alternative explanation for

the increase in FPF resulting from the use of rougher carrier particles is the lower adhesion strengths of drug particles to rougher carrier surfaces. This could be due to sheltering of drug particles from the press-on forces during blending when the drug particles were distributed in the surface crevices. Even though no conclusive explanation has been given, a high degree of carrier surface roughness has been thought to contribute positively to the FPF.

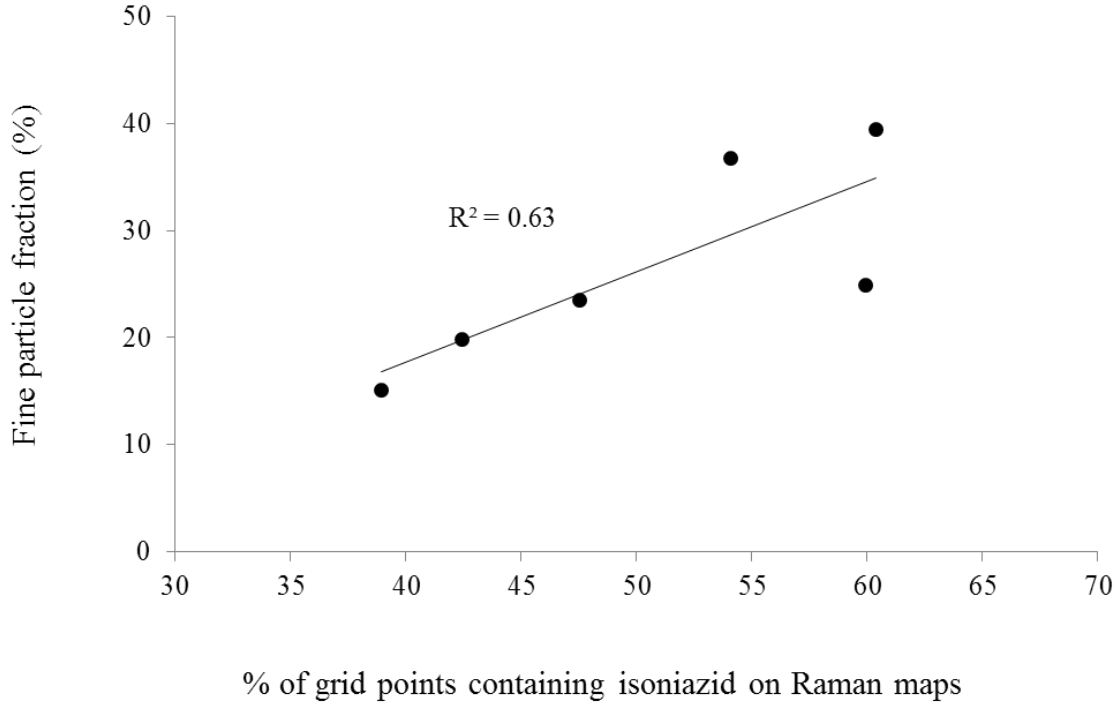

Figure 52. Relationship between the fine particle fraction and % isoniazid on the Raman maps.

4.3.3 Summary of Part 3

The investigations in Part 3 were conducted to evaluate the impact of surface roughness of carrier particles on the *in vitro* performance and drug distribution on carrier particles

of DPI formulations. In Part 3A of this study, DPI formulations with rough roller compacted carrier particles exhibited significantly higher FPF than both the inhalation grade and fluid-bed coated carriers. While the FPF of formulations containing the smoother carriers were significantly improved with the addition of fine lactose, the same outcome was not observed for the rougher roller compacted carriers. A direct relationship between the FPF and MMAD was not found for the series of formulations used in this part of the study. The higher MMAD of drug particles from formulations containing the rougher carriers suggested that fine drug particles could have been entrapped on rougher carriers. However, surface roughness still had an immensely beneficial impact on the FPF of DPI formulations.

In Part 3B of this study, Raman chemical imaging was explored as a method for investigating the spatial distribution of drug particles/agglomerates on carrier surfaces. A univariate approach for detecting the presence of isoniazid on the lactose carrier surface was successfully adopted. Preliminary work showed that the relatively high probability of detecting drug particles of a low concentration was related to the surface distribution of small drug particles over the coarse carrier particles in the interactive mixtures. One useful parameter that was calculated from the Raman chemical images was the % area of the image where the Raman signal of the drug had been detected. By choosing the appropriate sampling strategy, this parameter could either be used as (a) an indication of the content of drug in the interactive mixture or (b) an indirect method for visualization of particle surfaces. The surface coverage of drug was found to be unchanged with increasing content of fine lactose in the formulation. However, the surface coverage of drug was likely to be confounded by formation of drug-lactose agglomerates when fine lactose was added. Differences in surface coverage were much more pronounced when carriers of different roughness were used. Rougher carriers showed better drug surface

coverage on the carrier particles, suggesting that the spatial distribution of drug particles was wider on rougher surfaces. Although the explanations remain elusive, the mechanisms by which the spatial distribution of drug affects the FPF warrants more future work. This is expected to provide clearer evidence on the positive impact of carrier roughness to improve DPI drug delivery performance.

CHAPTER 5

CONCLUSION

5 CONCLUSION

Carrier surface roughness is an important physical characteristic which critically influences the aerosolization of micronized drug particles in carrier-based DPI formulations. Unlike other carrier particle properties such as size and shape, quantitative measurements of surface roughness are challenging to perform. The modification of surface roughness of particulates, particularly the process of surface roughening, has not been well studied. The research work conducted in this thesis has covered several important aspects in the use of rough carrier particles in DPI formulations. They include the quantification of surface roughness, preparation of rough carrier particles and the evaluation of their performance in DPI formulations.

Surface topographies of carriers were captured using optical profilometry, which is a rapid and non-contact method based on white-light interferometry. Raw surface images contained surface information spanning many length scales and the measurements were significantly affected by the random orientation of particles with respect to the horizontal plane of measurement. The magnitude of surface roughness, R_a, was found to be significantly influenced by the image processing techniques utilized in its calculation. By applying filters to extract surface information at the desired scale of observation, the effects of surface orientation and scan area were minimized. The presentation of roughness measurements together with the conditions for their derivation not only allows for more valid comparisons of R_a values in subsequent studies, but also ensures that measurements can be reproduced by other operators using similar equipment.

Studies on the preparation of rough carrier particles were conducted using two methods which employed very different principles. Surface roughening by fluid-bed coating was based on the adhesion of micronized fine lactose on the surfaces of coarse crystallized

lactose particles. Surface roughening by roller compaction was based on extensive fragmentation and bonding of fragments to create much rougher carriers of granular nature. The conditions for the preparation of rough carriers were investigated and identified for each method. The particle size of powders used for coating and amount of micronized lactose sprayed were found to be important factors contributing to the surface roughness of the fluid-bed coated carrier particles. Even for lactose powders with a relatively narrow starting size distribution, larger particles in the feed were roughened to a greater extent than the smaller particles. For roller compaction, the processibility of powder blends were studied in greater detail and the imparted carrier roughness was found to be more dependent on the compaction force than the size or composition of the powder blends used in roller compaction. The feasibility of compaction at high roll forces as well as consistent compaction parameters were identified as the main criteria for the selection of powder blends. These desirable characteristics were in turn found to be influenced by the particle size distribution and powder flow properties. Of the several flow parameters that were evaluated, the specific energy obtained from the powder rheometer could best reflect the variability in the compaction parameters during roller compaction.

The effects of rougher carrier particles on the *in vitro* performance and drug distribution of carrier particles of DPI formulations were investigated. The rougher roller compacted carriers exhibited significantly higher FPF than both the inhalation grade and fluid-bed coated carriers. Addition of fine lactose improved the FPF of formulations containing rougher carriers to a much lower extent than those containing smooth carriers. This was important since the inclusion of fine lactose particles is a commonly reported strategy for improving DPI performance. The higher MMAD of drug particles from formulations containing the rougher carriers suggest that fine drug particles could have been

entrapped on rougher carriers. Nevertheless, surface roughness was overall shown to have an immensely beneficial impact on the FPF of DPI formulations. Following this, Raman chemical imaging was explored as a method for investigating the spatial distribution of drug particles/agglomerates on carrier surfaces. This method was found to be complex and time-consuming but could provide valuable chemical information about carrier surfaces which could not be obtained by other imaging equipment, such as the SEM. Raman spectral mapping was used for indirect visualization of the drug particles/agglomerates on carrier surfaces only after proper considerations of the concentration of drug and the sampling plan for construction of the chemical images. The surface coverage of drug on the carrier surface had provided useful insights which could describe how well drug particles/agglomerates were being dispersed over the surface. Rougher carriers were shown to result in greater surface coverage of drug on the carrier, suggesting that drug was more efficiently dispersed as smaller agglomerates on rough surfaces.

Finally, two research areas with potential scientific impact are identified for future investigation. First, a comprehensive evaluation of carrier surface roughness should also include investigations in the macro-, micro- and nano-scale surface features. This may require the concurrent usage of multiple surface measurement equipment, such as both the optical profilometer and the scanning probe microscope. The most challenging aspect will probably be the need to derive common and comparable roughness parameters from both line and area profiling methods. Second, the interactive mixing of rough carriers with micronized drug is a relatively unexplored area of research. Most researchers have instead concentrated their efforts on the process of drug aerosolization. The Raman spectral mapping conducted in this thesis has shown that the spatial orientation of drug particles was altered by carrier roughness in the interactive mixtures. Hence, it is

important to understand the contributions of surface roughness during interactive mixing to DPI performance. This could potentially aid formulation scientists in refining the selection criteria for carriers in DPI formulations, especially in terms of their surface characteristics.

CHAPTER 6

REFERENCES

6 REFERENCES

1. N.R. Labirisand M.B. Dolovich. Pulmonary drug delivery. Part I: Physiological factors affecting therapeutic effectiveness of aerosolized medications. British Journal of Clinical Pharmacology. 56:588-599 (2003).
2. J.S. Patiland S. Sarasija. Pulmonary drug delivery strategies: A concise, systematic review. Lung India : Official Organ of Indian Chest Society. 29:44-49 (2012).
3. J.S. Patton, C.S. Fishburn, and J.G. Weers. The Lungs as a Portal of Entry for Systemic Drug Delivery. Proceedings of the American Thoracic Society. 1:338-344 (2004).
4. D.E. Geller. Comparing clinical features of the nebulizer, metered-dose inhaler, and dry powder inhaler. Respir Care. 50:1313-1321 (2005).
5. C. Marriottand H.W. Frijlink. Lactose as a carrier for inhalation products: breathing new life into an old carrier. Advanced Drug Delivery Reviews. 64:217-219 (2012).
6. S.R. Carvalho, A.B. Watts, J.I. Peters, and R.O. Williams. Dry Powder Inhalation for Pulmonary Delivery: Recent Advances and Continuing Challenges. Pulmonary Drug Delivery, John Wiley & Sons, Ltd 2015, pp. 35-62.
7. P.L. Stephensonand W.J. Thiel. The effect of humidity on the production of ordered mixtures. Powder Technology. 25:115-119 (1980).
8. J.P. Mitchelland M.W. Nagel. Particle Size Analysis of Aerosols from Medicinal Inhalers. KONA:32-65 (2004).
9. Y. Kawashima, T. Serigano, T. Hino, H. Yamamoto, and H. Takeuchi. Effect of surface morphology of carrier lactose on dry powder inhalation property of pranlukast hydrate. International Journal of Pharmaceutics. 172:179-188 (1998).
10. M.P. Timsina, G.P. Martin, C. Marriott, D. Ganderton, and M. Yianneskis. Drug delivery to the respiratory tract using dry powder inhalers. International Journal of Pharmaceutics. 101:1-13 (1994).
11. P.C. Emmett, R.J. Aitken, and W.J. Hannan. Measurements of the total and regional deposition of inhaled particles in the human respiratory tract. Journal of Aerosol Science. 13:549-560 (1982).
12. W. Stahlhofen, J. Gebhart, and J. Heyder. Experimental determination of the regional deposition of aerosol particles in the human respiratory tract. American Industrial Hygiene Association Journal. 41:385-398 (1980).
13. H. Chrystyn. The Diskus™: a review of its position among dry powder inhaler devices. International Journal of Clinical Practice. 61:1022-1036 (2007).
14. D.C. Cipollaand I. Gonda. Formulation technology to repurpose drugs for inhalation delivery. Drug Discovery Today: Therapeutic Strategies. 8:123-130 (2011).

15. P.M. Young, O. Wood, J. Ooi, and D. Traini. The influence of drug loading on formulation structure and aerosol performance in carrier based dry powder inhalers. International Journal of Pharmaceutics. 416:129-135 (2011).
16. M. Kumon, S. Machida, M. Suzuki, A. Kusai, E. Yonemochi, and K. Terada. Application and mechanism of inhalation profile improvement of DPI formulations by mechanofusion with magnesium stearate. Chemical and Pharmaceutical Bulletin. 56:617-625 (2008).
17. P. Begat, D.A.V. Morton, J.N. Staniforth, and R. Price. The cohesive-adhesive balances in dry powder inhaler formulations I: Direct quantification by atomic force microscopy. Pharmaceutical Research. 21:1591-1597 (2004).
18. A.M. Healy, M.I. Amaro, K.J. Paluch, and L. Tajber. Dry powders for oral inhalation free of lactose carrier particles. Advanced Drug Delivery Reviews. 75:32-52 (2014).
19. G. Pilcer, T. Sebti, and K. Amighi. Formulation and characterization of lipid-coated tobramycin particles for dry powder inhalation. Pharmaceutical Research. 23:931-940 (2006).
20. J. Raula, A. Lähde, and E.I. Kauppinen. Aerosolization behavior of carrier-free l-leucine coated salbutamol sulphate powders. International Journal of Pharmaceutics. 365:18-25 (2009).
21. J. Raula, F. Thielmann, M. Naderi, V.P. Lehto, and E.I. Kauppinen. Investigations on particle surface characteristics vs. dispersion behaviour of l-leucine coated carrier-free inhalable powders. International Journal of Pharmaceutics. 385:79-85 (2010).
22. Q.T. Zhou, L. Qu, I. Larson, P.J. Stewart, and D.A.V. Morton. Improving aerosolization of drug powders by reducing powder intrinsic cohesion via a mechanical dry coating approach. International Journal of Pharmaceutics. 394:50-59 (2010).
23. D.L. French, D.A. Edwards, and R.W. Niven. The influence of formulation on emission, deaggregation and deposition of dry powders for inhalation. Journal of Aerosol Science. 27:769-783 (1996).
24. D. Lechuga-Ballesteros, C. Charan, C.L.M. Stults, C.L. Stevenson, D.P. Miller, R. Vehring, V. Tep, and M.C. Kuo. Trileucine improves aerosol performance and stability of spray-dried powders for inhalation. Journal of Pharmaceutical Sciences. 97:287-302 (2008).
25. R. Feldstein, J. Glass, and S.S. Steiner. Self assembling diketopiperazine drug delivery system, Vol. US5352461 A, United States, 1994.
26. D.A. Edwards, J. Hanes, G. Caponetti, J. Hrkach, A. Ben-Jebria, M.L. Eskew, J. Mintzes, D. Deaver, N. Lotan, and R. Langer. Large porous particles for pulmonary drug delivery. Science. 276:1868-1871 (1997).
27. M.E. Aulton. Pulmonary drug delivery. In M.E. Aulton (ed.), Aulton's pharmaceutics: the design and manufacture of medicines, Churchill Livingstone 2007, pp. 546-547.

28. eMC. Summary of Product Characteristics - Bricanyl Turbohaler, 0.5mg/dose, inhalation powder, Datapharm Communications Limited, Surrey, 2002.
29. eMC. Summary of Product Characteristics - Pulmicort Turbohaler 100, Datapharm Communications Limited, Surrey, 2002.
30. N. El-Gendy, S. Huang, P. Selvam, P. Soni, and C. Berkland. Development of budesonide nanocluster dry powder aerosols: Formulation and stability. Journal of Pharmaceutical Sciences. 101(9):3445-3455 (2012).
31. H. Larhrib, X.M. Zeng, G.P. Martin, C. Marriott, and J. Pritchard. The use of different grades of lactose as a carrier for aerosolised salbutamol sulphate. International Journal of Pharmaceutics. 191:1-14 (1999).
32. Q.T. Zhouand D.A.V. Morton. Drug-lactose binding aspects in adhesive mixtures: Controlling performance in dry powder inhaler formulations by altering lactose carrier surfaces. Advanced Drug Delivery Reviews. 64:275-284 (2012).
33. Y. Rahimpour, M. Kouhsoltani, and H. Hamishehkar. Alternative carriers in dry powder inhaler formulations. Drug Discovery Today. 19:618-626 (2014).
34. H. Steckeland N. Bolzen. Alternative sugars as potential carriers for dry powder inhalations. International Journal of Pharmaceutics. 270:297-306 (2004).
35. M.E. Aulton. Mixing. In M.E. Aulton (ed.), Aulton's pharmaceutics: the design and manufacture of medicines, Churchill Livingstone 2007, pp. 161-162.
36. J.A. Hersey. Ordered mixing: A new concept in powder mixing practice. Powder Technology. 11:41-44 (1975).
37. F. Podczeck. Adhesion forces in interactive powder mixtures of a micronized drug and carrier particles of various particle size distributions. Journal of Adhesion Science and Technology. 12:1323-1339 (1998).
38. A. Vossand W.H. Finlay. Deagglomeration of dry powder pharmaceutical aerosols. International Journal of Pharmaceutics. 248:39-50 (2002).
39. A.H. De Boer, H.K. Chan, and R. Price. A critical view on lactose-based drug formulation and device studies for dry powder inhalation: Which are relevant and what interactions to expect? Advanced Drug Delivery Reviews. 64:257-274 (2012).
40. Q. Zhouand D.A.V. Morton. Drug–lactose binding aspects in adhesive mixtures: Controlling performance in dry powder inhaler formulations by altering lactose carrier surfaces. Advanced Drug Delivery Reviews. 64:275-284 (2012).
41. G. Pilcer, N. Wauthoz, and K. Amighi. Lactose characteristics and the generation of the aerosol. Advanced Drug Delivery Reviews. 64:233-256 (2012).
42. X. Kou, L.W. Chan, H. Steckel, and P.W.S. Heng. Physico-chemical aspects of lactose for inhalation. Advanced Drug Delivery Reviews. 64:220-232 (2012).
43. M.D. Jones, P. Young, and D. Traini. The use of inverse gas chromatography for the study of lactose and pharmaceutical materials used in dry powder inhalers. Advanced Drug Delivery Reviews. 64:285-293 (2012).
44. B.H.J. Dickhoff, A.H. de Boer, D. Lambregts, and H.W. Frijlink. The effect of carrier surface and bulk properties on drug particle detachment from crystalline

lactose carrier particles during inhalation, as function of carrier payload and mixing time. European Journal of Pharmaceutics and Biopharmaceutics. 56:291-302 (2003).

45. B.H.J. Dickhoff, A.H. de Boer, D. Lambregts, and H.W. Frijlink. The interaction between carrier rugosity and carrier payload, and its effect on drug particle redispersion from adhesive mixtures during inhalation. European Journal of Pharmaceutics and Biopharmaceutics. 59:197-205 (2005).
46. V. Swaminathanand D.O. Kildsig. The effect of particle morphology on the physical stability of pharmaceutical powder mixtures: The effect of surface roughness of the carrier on the stability of ordered mixtures. Drug Development and Industrial Pharmacy. 26:365-373 (2000).
47. V.K. Vikas Anand Saharan, Mahesh Kataria, Vandana Kharb, Pratim Kumar Choudhury. Ordered mixing: mechanism, process and applications in pharmaceutical formulations. Asian Journal of Pharmaceutical Sciences. 3:240-259 (2008).
48. L.W. Chan, L.T. Lim, and P.W.S. Heng. Immobilization of fine particles on lactose carrier by precision coating and its effect on the performance of dry powder formulations. Journal of Pharmaceutical Sciences. 92:975-984 (2003).
49. K. Iida, Y. Hayakawa, H. Okamoto, K. Danjo, and H. Luenberger. Effect of surface covering of lactose carrier particles on dry powder inhalation properties of salbutamol sulfate. Chemical & Pharmaceutical Bulletin. 51:1455-1457 (2003).
50. K. Iida, H. Todo, H. Okamoto, K. Danjo, and H. Leuenberger. Preparation of dry powder inhalation with lactose carrier particles surface-coated using a Wurster fluidized bed. Chemical and Pharmaceutical Bulletin. 53:431-434 (2005).
51. M.P. Flament, P. Leterme, and A. Gayot. The influence of carrier roughness on adhesion, content uniformity and the in vitro deposition of terbutaline sulphate from dry powder inhalers. International Journal of Pharmaceutics. 275:201-209 (2004).
52. P.M. Young, P. Kwok, H. Adi, H.K. Chan, and D. Traini. Lactose composite carriers for respiratory delivery. Pharmaceutical Research. 26:802-810 (2009).
53. F. Podczeck. The relationship between particulate properties of carrier materials and the adhesion force of drug particles in interactive powder mixtures. Journal of Adhesion Science and Technology. 11:1089-1104 (1997).
54. S. Adi, H. Adi, H.K. Chan, Z. Tong, R. Yang, and A. Yu. Effects of mechanical impaction on aerosol performance of particles with different surface roughness. Powder Technology. 236:164-170 (2013).
55. B. Mei Jin Tan, C.V. Liew, L.W. Chan, and P.W.S. Heng. Particle Surface Roughness – Its Characterisation and Impact on Dry Powder Inhaler Performance. Pulmonary Drug Delivery, John Wiley & Sons Ltd, 2015, pp. 199-222.
56. A. Boryczko. Distribution of roughness and waviness components of turned surface profiles. Metrology and Measurement Systems. 17:611-620 (2010).

57. J. Raja, B. Muralikrishnan, and S. Fu. Recent advances in separation of roughness, waviness and form. Precision Engineering. 26:222-235 (2002).
58. M. Bunker, M. Davies, and C. Roberts. Towards screening of inhalation formulations: Measuring interactions with atomic force microscopy. Expert Opinion on Drug Delivery. 2:613-624 (2005).
59. P.M. Young, D. Cocconi, P. Colombo, R. Bettini, R. Price, D.F. Steele, and M.J. Tobyn. Characterization of a surface modified dry powder inhalation carrier prepared by "particle smoothing". Journal of Pharmacy and Pharmacology. 54:1339-1344 (2002).
60. P.W.S. Heng, L.W. Chan, and L.T. Lim. Quantification of the surface morphologies of lactose carriers and their effect on the in vitro deposition of salbutamol sulphate. Chemical and Pharmaceutical Bulletin. 48:393-398 (2000).
61. E.M. Littringer, A. Mescher, H. Schroettner, L. Achelis, P. Walzel, and N.A. Urbanetz. Spray dried mannitol carrier particles with tailored surface properties – The influence of carrier surface roughness and shape. European Journal of Pharmaceutics and Biopharmaceutics. 82:194-204 (2012).
62. A.M. Boshhihaand N.A. Urbanetz. Influence of carrier surface fines on dry powder inhalation formulations. Drug Development and Industrial Pharmacy. 35:904-916 (2009).
63. D.J. Whitehouseand J.F. Archard. The Properties of Random Surfaces of Significance in their Contact. Proceedings of the Royal Society of London A Mathematical and Physical Sciences. 316:97-121 (1970).
64. F. Podczeck. The Influence of Particle Size Distribution and Surface Roughness of Carrier Particles on the in vitro Properties of Dry Powder Inhalations. Aerosol Science and Technology. 31:301-321 (1999).
65. N.Y.K. Chew, P. Tang, H.K. Chan, and J.A. Raper. How much particle surface corrugation is sufficient to improve aerosol performance of powders? Pharmaceutical Research. 22:148-152 (2005).
66. S.G. Maas, G. Schaldach, E.M. Littringer, A. Mescher, U.J. Griesser, D.E. Braun, P.E. Walzel, and N.A. Urbanetz. The impact of spray drying outlet temperature on the particle morphology of mannitol. Powder Technology. 213:27-35 (2011).
67. H.J. Butt, B. Cappella, and M. Kappl. Force measurements with the atomic force microscope: Technique, interpretation and applications. Surface Science Reports. 59:1-152 (2005).
68. J.D. Kielyand D.A. Bonnell. Quantification of topographic structure by scanning probe microscopy. Journal of Vacuum Science and Technology B: Microelectronics and Nanometer Structures. 15:1483-1493 (1997).
69. U. Sindeland I. Zimmermann. Measurement of interaction forces between individual powder particles using an atomic force microscope. Powder Technology. 117:247-254 (2001).

70. O. Dos Santos Ferreira, E. Gelinck, D. de Graaf, and H. Fischer. Adhesion experiments using an AFM—Parameters of influence. Applied Surface Science. 257:48-55 (2010).
71. W.P. Dong, E. Mainsah, and K.J. Stout. Determination of appropriate sampling conditions for three-dimensional microtopography measurement. International Journal of Machine Tools and Manufacture. 36:1347-1362 (1996).
72. A.D. Karande, Q. Zhou, L.W. Chan, P.W.S. Heng, and C.V. Liew. Scanning probe microscopy for surface roughness characterization of lactose carriers used in dry powder inhalation therapy. Journal of Scanning Probe Microscopy. 2:5-9 (2007).
73. F. Marinello, E. Savio, P. Bariani, and S. Carmignato. Coordinate metrology using scanning probe microscopes. Measurement Science and Technology. 20(8) (2009).
74. V.M.G. Digital Instruments. Scanning probe microscopy training notebook, Digital Instruments, Santa Barbara, CA, 1998, p. 11.
75. P. Samyn, J. Van Erps, H. Thienpont, and G. Schoukens. Paper coatings with multi-scale roughness evaluated at different sampling sizes. Applied Surface Science. 257:5613-5625 (2011).
76. ISO-4287. ISO 4287:1997 - Geometrical Product Specifications (GPS) -- Surface texture: Profile method -- Terms, definitions and surface texture parameters, Vol. 2012, International Organization for Standardization, Geneva, 1997.
77. M.M. Amaral, M.P. Raele, J.P. Caly, R.E. Samada, N.D. Vieira Jr, and A.Z. Freitas. Roughness measurement methodology according to DIN 4768 using optical coherence tomography (OCT), Vol. 73902009.
78. F. Blateyron. New 3D parameters and filtration techniques for surface metrology, Japanese Society of Precision Engineering Annual Congress 2006, Tokyo, 2006.
79. K. Carneiro, C.P. Jensen, J.F. Jørgensen, J. Garnæs, and P.A. McKeown. Roughness Parameters of Surfaces by Atomic Force Microscopy. CIRP Annals - Manufacturing Technology. 44:517-522 (1995).
80. M. Seahand L.D. Chiffre. Quantification of Surface Texture. In H. Czichos, T. Saito, and L. Smith (eds.), Springer Handbook of Metrology and Testing, Springer Berlin Heidelberg 2011, pp. 281-335.
81. ISO-25178. ISO 25178-2:2012 - Geometrical product specifications (GPS) - Surface texture: Areal - Part 2: Terms, definitions and surface texture parameters, Vol. 2012, International Organization for Standardization, Geneva, 2012.
82. R.J. Crawford, H.K. Webb, V.K. Truong, J. Hasan, and E.P. Ivanova. Surface topographical factors influencing bacterial attachment. Advances in Colloid and Interface Science. 179–182:142-149 (2012).
83. J. Dejeu, M. Bechelany, L. Philippe, P. Rougeot, J. Michler, and M.l. Gauthier. Reducing the Adhesion between Surfaces Using Surface Structuring with PS Latex Particle. ACS Applied Materials & Interfaces. 2:1630-1636 (2010).

84. H.R. Fischerand E.R.M. Gelinck. Determination of adhesion forces between smooth and structured solids. Applied Surface Science. 258:9011-9017 (2012).
85. A. Spencer, I. Dobryden, N. Almqvist, A. Almqvist, and R. Larsson. The influence of AFM and VSI techniques on the accurate calculation of tribological surface roughness parameters. Tribology International. 57:242-250 (2013).
86. S. Adi, H. Adi, H.K. Chan, P.M. Young, D. Traini, R. Yang, and A. Yu. Scanning white-light interferometry as a novel technique to quantify the surface roughness of micron-sized particles for inhalation. Langmuir. 24:11307-11312 (2008).
87. M.J. Donovanand H.D.C. Smyth. Influence of size and surface roughness of large lactose carrier particles in dry powder inhaler formulations. International Journal of Pharmaceutics. 402:1-9 (2010).
88. N. Islam, P. Stewart, I. Larson, and P. Hartley. Surface roughness contribution to the adhesion force distribution of salmeterol xinafoate on lactose carriers by atomic force microscopy. Journal of Pharmaceutical Sciences. 94:1500-1511 (2005).
89. J. Shurand R. Price. Advanced microscopy techniques to assess solid-state properties of inhalation medicines. Advanced Drug Delivery Reviews. 64:369-382 (2012).
90. F. Ferrari, D. Cocconi, R. Bettini, F. Giordano, P. Santi, M. Tobyn, R. Price, P. Young, C. Caramella, and P. Colombo. The surface roughness of lactose particles can be modulated by wet-smoothing using a high-shear mixer. AAPS PharmSciTech. 5(4):69-74 (2004).
91. J. Paluszyńskiand W. Slówko. Measurements of the surface microroughness with the scanning electron microscope. Journal of Microscopy. 233:10-17 (2009).
92. X.M. Zeng, K.H. Pandhal, and G.P. Martin. The influence of lactose carrier on the content homogeneity and dispersibility of beclomethasone dipropionate from dry powder aerosols. International Journal of Pharmaceutics. 197:41-52 (2000).
93. T. Hino, T. Serigano, H. Yamamoto, H. Takeuchi, T. Niwa, and Y. Kawashima. Particle design of Wogon extract dry powder for inhalation aerosols with granulation method. International Journal of Pharmaceutics. 168:59-68 (1998).
94. D. Traini, S. Scalia, H. Adi, E. Marangoni, and P.M. Young. Polymer coating of carrier excipients modify aerosol performance of adhered drugs used in dry powder inhalation therapy. International Journal of Pharmaceutics. 438:150-159 (2012).
95. D. El-Sabawi, R. Price, S. Edge, and P.M. Young. Novel temperature controlled surface dissolution of excipient particles for carrier based dry powder inhaler formulations. Drug Development and Industrial Pharmacy. 32:243-251 (2006).
96. D. El-Sabawi, S. Edge, R. Price, and P.M. Young. Continued investigation into the influence of loaded dose on the performance of dry powder inhalers: Surface smoothing effects. Drug Development and Industrial Pharmacy. 32:1135-1138 (2006).

97. N. Islam, P. Stewart, I. Larson, and P. Hartley. Lactose surface modification by decantation: Are drug-fine lactose ratios the key to better dispersion of salmeterol xinafoate from lactose-interactive mixtures? Pharmaceutical Research. 21:492-499 (2004).
98. C.P. Watling, J.A. Elliott, C. Scruton, and R.E. Cameron. Surface modification of lactose inhalation blends by moisture. International Journal of Pharmaceutics. 391:29-37 (2010).
99. V. Bérard, E. Lesniewska, C. Andrès, D. Pertuy, C. Laroche, and Y. Pourcelot. Dry powder inhaler: Influence of humidity on topology and adhesion studied by AFM. International Journal of Pharmaceutics. 232:213-224 (2002).
100. R. Price, P.M. Young, S. Edge, and J.N. Staniforth. The influence of relative humidity on particulate interactions in carrier-based dry powder inhaler formulations. International Journal of Pharmaceutics. 246:47-59 (2002).
101. R. Guchardi, M. Frei, E. John, and J.S. Kaerger. Influence of fine lactose and magnesium stearate on low dose dry powder inhaler formulations. International Journal of Pharmaceutics. 348:10-17 (2008).
102. X.M. Zeng, G.P. Martin, C. Marriott, and J. Pritchard. Crystallization of lactose from carbopol gels. Pharmaceutical Research. 17:879-886 (2000).
103. X.M. Zeng, G.P. Martin, C. Marriott, and J. Pritchard. The use of lactose recrystallised from carbopol gels as a carrier for aerosolised salbutamol sulphate. European Journal of Pharmaceutics and Biopharmaceutics. 51:55-62 (2001).
104. X.M. Zeng, G.P. Martin, S.-K. Tee, and C. Marriott. The role of fine particle lactose on the dispersion and deaggregation of salbutamol sulphate in an air stream in vitro. International Journal of Pharmaceutics. 176:99-110 (1998).
105. D.Y.T. Wong, P. Wright, and M.E. Aulton. The derformation of alpha-lactose monohydrate and anhydrous alpha-lactose monocrystals. Drug Development and Industrial Pharmacy. 14:2109-2126 (1988).
106. M.D. Jones, J.C. Hooton, M.L. Dawson, A.R. Ferrie, and R. Price. An investigation into the dispersion mechanisms of ternary dry powder inhaler formulations by the quantification of interparticulate forces. Pharmaceutical Research. 25:337-348 (2008).
107. G. Saint-Lorant, P. Leterme, A. Gayot, and M.P. Flament. Influence of carrier on the performance of dry powder inhalers. International Journal of Pharmaceutics. 334:85-91 (2007).
108. S.K. Tee, C. Marriott, X.M. Zeng, and G.P. Martin. The use of different sugars as fine and coarse carriers for aerosolised salbutamol sulphate. International Journal of Pharmaceutics. 208:111-123 (2000).
109. M.D. Jones, J.G.F. Santo, B. Yakub, M. Dennison, H. Master, and G. Buckton. The relationship between drug concentration, mixing time, blending order and ternary dry powder inhalation performance. International Journal of Pharmaceutics. 391:137-147 (2010).

110. V.N.P. Le, T.H.H. Thi, E. Robins, and M.P. Flament. Dry powder inhalers: Study of the parameters influencing adhesion and dispersion of fluticasone propionate. AAPS PharmSciTech. 13:477-484 (2012).
111. E. Guenette, A. Barrett, D. Kraus, R. Brody, L. Harding, and G. Magee. Understanding the effect of lactose particle size on the properties of DPI formulations using experimental design. International Journal of Pharmaceutics. 380:80-88 (2009).
112. K. Iida, Y. Hayakawa, H. Okamoto, K. Danjo, and H. Luenberger. Effect of surface layering time of lactose carrier particles on dry powder inhalation properties of salbutamol sulfate. Chemical and Pharmaceutical Bulletin. 52:350-353 (2004).
113. P. Selvam, S. Marek, C.R. Truman, D. McNair, and H.D.C. Smyth. Micronized drug adhesion and detachment from surfaces: Effect of loading conditions. Aerosol Science and Technology. 45:81-87 (2011).
114. S. Das, I. Larson, P. Young, and P. Stewart. Agglomerate properties and dispersibility changes of salmeterol xinafoate from powders for inhalation after storage at high relative humidity. European Journal of Pharmaceutical Sciences. 37:442-450 (2009).
115. P. Begat, D.A.V. Morton, J. Shur, P. Kippax, J.N. Staniforth, and R. Price. The role of force control agents in high-dose dry powder inhaler formulations. Journal of Pharmaceutical Sciences. 98:2770-2783 (2009).
116. R. Pfeffer, R.N. Dave, D. Wei, and M. Ramlakhan. Synthesis of engineered particulates with tailored properties using dry particle coating. Powder Technology. 117:40-67 (2001).
117. D. Mortonand J. Staniforth. Dry powder composition comprising co-jet milled particles for pulmonary inhalation. U.S. Patent 8182838. Vectura Limited, United States, 2012.
118. M. Kumon, M. Suzuki, A. Kusai, E. Yonemochi, and K. Terada. Novel approach to DPI carrier lactose with mechanofusion process with additives and evaluation by IGC. Chemical and Pharmaceutical Bulletin. 54:1508-1514 (2006).
119. L. Vepsäläinen, P. Stenberg, P. Pääkkönen, M. Kuittinen, M. Suvanto, and T.A. Pakkanen. Roughness analysis for textured surfaces over several orders of magnitudes. Applied Surface Science. 284:222-228 (2013).
120. C. Lamband M. Zecchino. Wyko Surface Profilers Techinical Reference Manual, Veeco Metrology Group, Arizona, USA, 1999.
121. P.V. Quyet, A.K. Samanta, C.V. Liew, L.W. Chan, and P.W.S. Heng. A prediction model for monitoring ribbed roller compacted ribbons. Journal of Pharmaceutical Sciences. 102:2667-2678 (2013).
122. W.H. Finlay. 2 - Particle size distributions. In W.H. Finlay (ed.), The Mechanics of Inhaled Pharmaceutical Aerosols, Academic Press, London, 2001, pp. 3-15.
123. W. John. Size Distribution Characteristics of Aerosols. Aerosol Measurement, John Wiley & Sons Inc, 2011, pp. 41-54.

124. G. Ramachandranand D.W. Cooper. Size Distribution Data Analysis and Presentation. Aerosol Measurement, John Wiley & Sons Inc, 2011, pp. 479-506.
125. M. Rhodes. Storage and Flow of Powders – Hopper Design. Introduction to Particle Technology, John Wiley & Sons Ltd 2008, pp. 265-292.
126. M. Leturia, M. Benali, S. Lagarde, I. Ronga, and K. Saleh. Characterization of flow properties of cohesive powders: A comparative study of traditional and new testing methods. Powder Technology. 253:406-423 (2014).
127. H.Y. Saw, C.E. Davies, J.R. Jones, G. Brisson, and A.H.J. Paterson. Cohesion of lactose powders at low consolidation stresses. Advanced Powder Technology. 24:796-800 (2013).
128. M.J. Pelletier. Quantitative analysis using Raman spectrometry. Applied Spectroscopy. 57(1):20A-42A (2003).
129. S. Lakio, B. Vajna, I. Farkas, H. Salokangas, G. Marosi, and J. Yliruusi. Challenges in Detecting Magnesium Stearate Distribution in Tablets. AAPS PharmSciTech. 14:435-444 (2013).
130. B.N.J. Persson, O. Albohr, U. Tartaglino, A.I. Volokitin, and E. Tosatti. On the nature of surface roughness with application to contact mechanics, sealing, rubber friction and adhesion. Journal of Physics: Condensed Matter. 17:R1-R62 (2005).
131. H.R. Norouzi, N. Mostoufi, and R. Sotudeh-Gharebagh. Effect of fines on segregation of binary mixtures in gas–solid fluidized beds. Powder Technology. 225:7-20 (2012).
132. Z. Zou, H. Li, Q. Zhu, and Y. Wang. Experimental Study and Numerical Simulation of Bubbling Fluidized Beds with Fine Particles in Two and Three Dimensions. Industrial & Engineering Chemistry Research. 52:11302-11312 (2013).
133. S.R. Iyerand L.T. Drzal. Behavior of cohesive powders in narrow-diameter fluidized beds. Powder Technology. 57:127-133 (1989).
134. E.W. Chuan Lim, R.B. Hee Tan, and Z. Xiao. Mixing behaviors of wet granular materials in gas fluidized bed systems. AIChE Journal. 59:4058-4067 (2013).
135. L.S.C. Wan, P.W.S. Heng, and C.V. Liew. The influence of liquid spray rate and atomizing pressure on the size of spray droplets and spheroids. International Journal of Pharmaceutics. 118:213-219 (1995).
136. C. USP. United States Pharmacopeia 30 - National Formulary 25, *<1174> Powder Flow*, The United States Pharmacopeial Convention, United States, 2007.
137. W. Kaialyand A. Nokhodchi. Particle Engineering for Improved Pulmonary Drug Delivery Through Dry Powder Inhalers. Pulmonary Drug Delivery, John Wiley & Sons Ltd, 2015, pp. 171-198.
138. X.M. Zeng, G.P. Martin, C. Marriott, and J. Pritchard. The influence of carrier morphology on drug delivery by dry powder inhalers. International Journal of Pharmaceutics. 200:93-106 (2000).

139. H.-K. Chan. What is the role of particle morphology in pharmaceutical powder aerosols? Expert Opinion on Drug Delivery. 5:909-914 (2008).
140. H. Adi, I. Larson, H. Chiou, P. Young, D. Traini, and P. Stewart. Role of agglomeration in the dispersion of salmeterol xinafoate from mixtures for inhalation with differing drug to fine lactose ratios. Journal of Pharmaceutical Sciences. 97:3140-3152 (2008).
141. E. Guenette, A. Barrett, D. Kraus, R. Brody, L. Harding, and G. Magee. Understanding the effect of lactose particle size on the properties of DPI formulations using experimental design. International Journal of Pharmaceutics. 380:80-88 (2009).
142. M.D. Jonesand R. Price. The influence of fine excipient particles on the performance of carrier-based dry powder inhalation formulations. Pharmaceutical Research. 23:1665-1674 (2006).
143. M.D. Loueyand P.J. Stewart. Particle interactions involved in aerosol dispersion of ternary interactive mixtures. Pharmaceutical Research. 19:1524-1531 (2002).
144. J. Shur, H. Harris, M. Jones, J.S. Kaerger, and R. Price. The Role of Fines in the Modification of the Fluidization and Dispersion Mechanism Within Dry Powder Inhaler Formulations. Pharmaceutical Research. 25:1631-1640 (2008).
145. T. Srichana, G.P. Martin, and C. Marriott. On the relationship between drug and carrier deposition from dry powder inhalers in vitro. International Journal of Pharmaceutics. 167:13-23 (1998).
146. K. Thalberg, E. Berg, and M. Fransson. Modeling dispersion of dry powders for inhalation. The concepts of total fines, cohesive energy and interaction parameters. International Journal of Pharmaceutics. 427:224-233 (2012).
147. D. Ganderton. The Generation of Respirable Clouds from Coarse Powder Aggregates. Journal of Biopharmaceutical Sciences. 3:101-105 (1992).
148. P. Lucas, K. Anderson, and J.N. Staniforth. Protein Deposition from Dry Powder Inhalers: Fine Particle Multiplets as Performance Modifiers. Pharmaceutical Research. 15(4):562-569 (1998).
149. H. Kinnunen, G. Hebbink, H. Peters, D. Huck, L. Makein, and R. Price. Extrinsic lactose fines improve dry powder inhaler formulation performance of a cohesive batch of budesonide via agglomerate formation and consequential co-deposition. International Journal of Pharmaceutics. 478:53-59 (2015).
150. H. Susiand J.S. Ard. Laser-raman spectra of lactose. Carbohydrate Research. 37:351-354 (1974).
151. B.M. Murphy, S.W. Prescott, and I. Larson. Measurement of lactose crystallinity using Raman spectroscopy. Journal of Pharmaceutical and Biomedical Analysis. 38:186-190 (2005).
152. S. Zellnitz, H. Schroettner, and N.A. Urbanetz. Influence of surface characteristics of modified glass beads as model carriers in dry powder inhalers (DPIs) on the aerosolization performance. Drug Development and Industrial Pharmacy. 41:1710-1717 (2015).

153. A. Pacławski, J. Szlęk, R. Lau, R. Jachowicz, and A. Mendyk. Empirical modeling of the fine particle fraction for carrier-based pulmonary delivery formulations. International Journal of Nanomedicine. 10:801-810 (2015).

CHAPTER 7

LIST OF PUBLICATIONS

7 LIST OF PUBLICATIONS

International journals

1. **Tan BMJ**, Loh ZH, Soh JLP, Liew CV, Heng PWS 2014. Distribution of a viscous binder during high shear granulation – Sensitivity to the method of delivery and its impact on product properties. *International Journal of Pharmaceutics* **460(1-2)**:255-263.
2. **Tan BMJ**, Tay JYS, Wong PM, Chan LW, Heng PWS 2015. Investigation of the milling capabilities of the F10 Fine Grind mill using Box-Behnken designs. *European Journal of Pharmaceutics and Biopharmaceutics* **89**:208-215.
3. **Tan BMJ**, Chan LW, Heng PWS 2016. Improving dry powder inhaler performance by surface roughening of lactose carrier particles. *Pharmaceutical Research* **33**(8):1923-1935.
4. **Tan BMJ**, Chan LW, Heng PWS 2016. Determination of the nip angle in roller compactors with serrated rolls. *Journal of Pharmaceutical Sciences* **105**(6):1967-1975.

Book chapters

1. **Tan BMJ**, Liew CV, Chan LW, Heng PWS. 2015. Particle Surface Roughness – Its Characterisation and Impact on Dry Powder Inhaler Performance. In Nokhodchi A, Martin GP, editors. *Pulmonary Drug Delivery: Advances and Challenges*, Chichester: John Wiley & Sons, Ltd. p 199-222.

Conference presentations

1. **Tan BMJ**, Tay JYS, Wong PM, Chan LW, Heng PWS 2013. Investigation of the milling capabilities of the Quadro F10 Fine Grind Mill. Asian Federation of Pharmaceutical Sciences (AFPS) Conference. Jeju, Republic of Korea.
2. **Tan BMJ**, Chan LW, Heng PWS 2014. Surface roughness measurement of lactose particles: Important measurement and image processing conditions. GEA Graduate Congress. Suwon, Republic of Korea.
3. **Tan BMJ**, Chan LW, Heng PWS 2015. A study of the drug dispersion performance of DPI lactose carriers of different surface characteristics. American Association of Pharmaceutical Scientists (AAPS) Annual Meeting and Exposition. Florida, USA.